Pro gradu
Economic geology

A RECONNAISSANCE STUDY ON THE DISTRIBUTION OF CRITICAL METALS IN ROCK-FORMING TRIOCTAHEDRAL MICAS OF FENNOSCANDIAN S-, I-, AND A-TYPE GRANITES

Jussi Rytkönen

2018

Supervisors:
Thomas Wagner, Tobias Fusswinkel, Anselm Loges

UNIVERSITY OF HELSINKI
FACULTY OF SCIENCE
DEPARTMENT OF GEOSCIENCES AND GEOGRAPHY
DIVISION OF GEOLOGY AND GEOCHEMISTRY

P.O. Box 64 (Gustaf Hällströmin katu 2a)
FI-00014 University of Helsinki

Tiedekunta/Osasto Fakultet/Sektion – Faculty	Laitos/Institution– Department
Faculty of Science	Department of Geosciences and Geography

Tekijä/Författare – Author

Jussi Rytkönen

Työn nimi / Arbetets titel – Title

A reconnaissance study on the distribution of critical metals in rock-forming trioctahedral micas of Fennoscandian S-, I-, and A-type granites

Oppiaine /Läroämne – Subject

Geology

Työn laji/Arbetets art – Level	Aika/Datum – Month and year	Sivumäärä/ Sidoantal – Number of pages
Pro gradu	March 2018	94 + 40

Tiivistelmä/Referat – Abstract

Critical metals are defined as rare specialty metals (e.g. Be, Sc, Co, Ga, Ge, Nb, REEs, In, Ta) that are critical for the facilitation of the Strategic Energy Technology Plan set by the European Union. These rare metals are typically associated with highly evolved granitic ores. Trioctahedral micas are often one of the main, if not sole, hydrous ferromagnesian phases in these granite-related rare metal deposits. Since many critical metals are readily incorporated in the mica crystal structure, micas are often used as petrogenetic indicators in assessing granite melt evolution.

This study is a preliminary investigation in the critical metal distribution of trioctahedral micas in Fennoscandian S-I-A type granites. Ten granite samples (6 A-type, 2 S-type, and 2 I-type samples) were selected for examination that represent three distinct areas within the Fennoscandian shield: the Paleoproterozoic Wiborg rapakivi batholith (A-type) in southeastern Finland, the Paleoproterozoic Västervik metasedimentary formation (S-type) in southeastern Sweden, and the Neoarchean Hattu schist belt (S- and I-type) in eastern Finland. Whole-rock major and trace element chemistry was determined via WD-XRF, mineral major element chemistry via WDS-EPMA, and mineral trace element chemistry via LA-ICP-MS.

The A-type granites are predominantly ferroan, alkali-calcic, and metaluminous, whereas the S- and I-type granites are predominantly magnesian, calc-alkalic, and peraluminous. Trioctahedral micas in the A-type granites are characteristically annitic, whereas S- and I-type granites trend progressively towards more phlogopitic compositions.

Trace element data indicates that most critical and rare metal abundances (Li, Be, B, Sc, Ga, Ge, Zr, Nb, In, Sn, Ta) tend to increase with progressing fractionation, but largely independent from granite type. Moreover, the absolute differences in abundances are often small, but distinct. However, owing to their more primitive character, I-type granites are typically less fractionated than A- and S-type granites, and thus contain lower amounts of critical and rare metals. Furthermore, it is indicated that the fractionation of the following elements may be correlated: Be & Al, Be & Sc, and In & Sc. Moreover, it is indicated that amphibole and muscovite minerals may incorporate Be, Sc, Zr, and In more readily than trioctahedral micas.

Avainsanat – Nyckelord – Keywords

critical metals, rare metals, biotite, trioctahedral mica, micas, muscovite, amphibole, hornblende, Fennoscandia, S-type, A-type, I-type, granite, granites, LA-ICP-MS

Säilytyspaikka – Förvaringställe – Where deposited

University of Helsinki Library

Muita tietoja – Övriga uppgifter – Additional information

37 figures, 11 tables

Tiedekunta/Osasto Fakultet/Sektion – Faculty Matemaattis-luonnnontieteellinen tiedekunta	Laitos/Institution– Department Geotieteiden ja maantieteen laitos

Tekijä/Författare – Author
Jussi Rytkönen

Työn nimi / Arbetets titel – Title
A reconnaissance study on the distribution of critical metals in rock-forming trioctahedral micas of Fennoscandian S-, I-, and A-type granites

Oppiaine /Läroämne – Subject
Geologia

Työn laji/Arbetets art – Level	Aika/Datum – Month and year	Sivumäärä/ Sidoantal – Number of pages
Pro Gradu	Maaliskuu 2018	94 + 40

Tiivistelmä/Referat – Abstract

Kriittiset metallit ovat harvinaisia erikoismetalleja (esim. Be, Sc, Co, Ga, Ge, Nb, REE, In, Ta), jotka on luokiteltu kriittisiksi EU:n energiastrategian toteuttamisen kannalta. Kriittiset metallitesiintymät liitetään usein kehittyneisiin graniittimalmioihin, joissa vesipitoiset kiilleminerаalit ovat yleinen rauta- ja magnesiumpitoinen pääminerаali. Koska useimmat kriittiset ja harvinaiset metallit fraktioituvat kiilleminerаalien kidehiloihin differentaation edetessä, kiilleminerаaleja käytetään usein graniittisulan petrogeneettisinä indikaattoreina.

Tämä tutkimus on alustava selvitys kriittisten metallien jakautumisesta Fennoskandian kilven alueella esiintyvien S-, I-, ja A-tyyppisten graniittien kiilleminerаaleissa. Tutkimuskohteiksi valittiin kymmenen graniittinäytettä (6 A-tyyppistä, 2 S-tyyppistä ja 2 I-tyyppistä), jotka edustavat Fennoskandian kilven kolmea tunnusomaista aluetta: Paleoproterotsooinen Viipurin rapakivibatoliitti (A-tyyppi) Kaakkois-Suomessa, Paleoproterotsooinen Västervikin metasedimentaarinen muodostuma (S-tyyppi) Kaakkois-Ruotsissa ja Neoarkeeinen Hatun liuskevyöhyke (S- ja I-tyyppi) Itä-Suomessa. Näytteiden kokokivikoostumus määritettiin WD-XRF:lla, mineraalien pääkomponentit WDS-EPMA:lla ja mineraalien hivenalkuainekoostumukset LA-ICP-MS:lla.

A-tyypin graniittinäytteet ovat pääosin rautapitoisia, alkali-kalkkisia ja metalumiinisia. S- ja I-tyypin graniitit ovat sen sijaan pääosin magnesiumpitoisia, kalkki-alkalisia ja peralumiinisia. Kiilleminerаalit ovat pääosin anniittisia A-tyypin graniiteissa, mutta S- ja I-tyyppien kiilteet vaihettuvat progressiivisesti kohti flogopiittisempia koostumuksia.

Hivenalkuainedata indikoi, että kriittisten ja harvinaisten metallien pitoisuudet (Li, Be, B, Ga, Zr, Nb, In, Sn, Hf, Ta, sekä mahdollisesti Sc ja Ge – käyttäen kobolttia fraktioitumisindikaattorina) pääosin kasvavat fraktioitumisen edetessä, mutta riippumatta graniittisulan tyypistä. Lisäksi absoluuttiset koostumuserot ovat usein pieniä. I-tyypin graniitit ovat kuitenkin usein A- ja S-tyypin graniitteja primitiivisempiä, ja siten sisältävät matalampia kriittisten ja harvinaisten metallien pitoisuuksia. Lisäksi tutkimusdata viittaa, että Be & Al, Be & Sc sekä In & Sc fraktioituminen saattavat olla toisistaan riippuvaisia, ja Be, Sc, Zr sekä In suosivat amfiboli- ja muskoviittimineraalien kidehiloja biotiittiin verrattuna.

Avainsanat – Nyckelord – Keywords
kriittiset metallit, harvinaiset metallit, biotiitti, kiille, kiilteet, Fennoskandia, S-tyyppi, I-tyyppi, A-tyyppi, graniitti

Säilytyspaikka – Förvaringställe – Where deposited
Helsingin yliopiston kirjasto

Muita tietoja – Övriga uppgifter – Additional information
37 kuvaa, 11 taulukkoa.

1. INTRODUCTION

1.1. Framework

Critical metals are rare specialty metals (e.g. Be, Sc, Co, Ga, Ge, Nb, REEs, In, Ta) that are used in the production of many hi-tech commodities and services. For example, Be is used in the aerospace industry owing to its high mechanical and thermal rigidness, Co in steel superalloys and batteries, Ga in Light Emitting Diodes (LEDs, e.g. in LCD monitors), and Nd in permanent magnets that are used in wind energy generators (European Commission 2015). The goals set in the EU Strategic Energy Technology Plan (reduction of greenhouse gas emissions and increased renewable energy supply) require the employment and use of numerous specialty metals that are produced predominantly outside the EU, and are mined mainly as by-products of other more common metals (Moss 2011). Thus, there are certain supply risks associated with many rare specialty metals, and hence their critical characterization.

Owing to their incompatible geochemical characteristics, economic critical and rare metal (e.g. Li, Zr, Sn, W) deposits are often associated with granite-related ores. The deposits may be sourced directly from granites through magmatic processes, but are more commonly affiliated with highly fractionated granites as a consequence of extreme fractional crystallization, metasomatic processes, or both (Černý et al. 2005). The extent of fractional crystallization is frequently assessed via fractionation indicators such as K/Rb, Ba/Rb, Nb/Ta, Zr/Hf, Al/Ga, and K/Cs (Černý et al. 1985). The underlying principle in all ratioed element fractionation indicators is that the paired elements behave similarly in geochemical processes, but are decoupled as certain minerals begin to precipitate from granitoid melts.

For example, K/Rb is one of the more often used fractionation indicators in granitic rocks (Černý et al. 1985). K is favored over Rb in crystallizing plagioclase and hornblende in basic to intermediate melts, which results in a decreasing K/Rb ratio. If biotite or K-feldspar precipitation is significant, such as in many granites, K accumulates over Rb into

biotite and K-feldspar crystal lattices. Therefore, the residual melt becomes enriched in Rb, and the K/Rb ratio starts to decrease with advancing crystallization. Hence, K/Rb decreases rapidly in late-magmatic and post-magmatic granites, which is well correlated with the concurrent increase in other rare metals abundances in the rock (Černý et al. 1985, Zaraisky et al. 2009).

Micas, and particularly trioctahedral micas (i.e. biotites), are often used as petrogenetic indicators in highly fractionated granites. The mica crystal structure can accommodate a wide variety of minor and trace elements, such as the Large Ion Lithophile Elements (LILE: e.g. K, Rb, Cs, Sr, Ba), High Field Strenght Elements (HFSE: e.g. Ti, Sc, Zr & Hf, Nb & Ta, U), Ga, Ge, In, to name a few (Rollinson 1993, Xie et al. 2015, Breiter et al. 2017). Moreover, micas are a common hydrous ferromagnesian phase in most granitoids, and in many rare element granitoids micas may be the only rock-forming hydrous Fe-Mg(-Ti)-silicate (Xie et al. 2015, Breiter et al. 2017). Thus, trace elements with an affinity to Fe, Mg, and Ti are readily fractionated into micas, and micas may be used as robust petrogenetic indicators.

1.2. Review of literature and aims of the study

This project began in late 2016 with the prior understanding that the fractionation (and hence distribution) of critical metals in trioctahedral micas of contrasting granite types (i.e. S-I-A-M granites) is an unexplored subject. However, since the start of this project, the literature in this field has expanded. A recent paper by Breiter et al. (2017) investigated the trace element fractionation of trioctahedral micas in S-, I-, and A-type granites from the Bohemian Massif (Central Europe). Breiter et al. (2017) argue that the literature on sufficiently accurate and sensitive *in situ* (i.e. LA-ICP-MS) analyses on trioctahedral mica compositions are, indeed, scarce, and no exhaustive surveys have been made. Furthermore, they state that granite-related mica studies with large datasets are limited to five papers, which are mostly related to S- or A-type granites: Van Lichtervelde et al. (2008), Johan et al. (2012), Roda-Robles et al. (2012), Li et al. (2015), and Xie et al. (2015). It is unclear what constitutes a large data set, but since then (or roughly concurrent with Breiter et al. 2017), at least three further *in situ* trioctahedral mica studies in granites have been published (in chronological order): Michallik et al. (2017), Simons

et al. (2017), and Berni et al. (2017).

Breiter et al. (2017) concluded that there are no clear differences in the trace element distribution between different granite types, but critical and rare metal abundances generally tend to increase in trioctahedral micas with advancing fractionation, which is in concert with other literature (Van Lichtervelde et al. 2008, Johan et al. 2012, Roda-Robles et al. 2012, Li et al. 2015, Xie et al. 2015, Berni et al. 2017, Michallik et al. 2017, Simons et al. 2017). However, it is stressed that this is a simplification as many factors influence and partake in trace element fractionation (e.g. pressure, temperature, other minerals, fluid phases, etc.), and some individual elements may be depleted in one deposit, whereas enriched in another, even if they share the same granite type.

Nonetheless, three aims were set for this study: (1) to understand the distribution of critical metals in rock-forming trioctahedral micas of different granite types (S-I-A), (2) to evaluate the critical metal potential of different granite types, and (3) to identify potential implications for granite-related ore forming processes. Thus, the ultimate objective was to gain preliminary insights for future research. To meet these goals, ten Fennoscadian S-, I-, and A-type granite samples were selected as a focus group, which were examined using whole-rock (WD-XRF) and mineral (WDS-EPMA and LA-ICP-MS) chemistry.

As a short note on terminology, the term *granite* is used in the broadest sense throughout this study. That is, granites are referred as rocks that plot within the granite, granodiorite, and tonalite fields of the IUGS classification (Streckeisen 1974). Moreover, the series name *biotite* is often used in place of *trioctahedral mica* and *lepidolite*. *Trioctahedral micas* encompass the annite – phlogopite – siderophyllite – eastonite trioctahedral end-members, whereas *lepidolite* is a series name for Li-rich trioctahedral micas (Rieder et al. 1998).

2. GEOLOGIC SETTING

The A-, S-, and I-type granite samples obtained for this study represent three distinct regions within the Fennoscandian Shield: the 1.65 – 1.62 Ga Paleoproterozoic Wiborg rapakivi batholith (A-type, samples LOV-1 to -6, Fig. 1) in southeastern Finland, the 1.85 – 1.80 Ga Paleoproterozoic REE-affiliated Olserum granite (S-type, sample OLR09, Fig. 2) located in the Västervik metasedimentary formation in southeastern Sweden, and the 2.76 – 2.70 Ga Neoarchean Hattu schist belt (S- and I-type; NAR-1 S-type; VIG-1 and KUI-3 I-type; Fig. 3) located in the Ilomantsi Greenstone Belt in eastern Finland (Vaasjoki et al. 1991, Vaasjoki et al. 1993, Nolte et al. 2011).

2.1. Wiborg rapakivi batholith

The Wiborg rapakivi batholith is characterized by anorogenic bimodal suites intruded into the c. 1.90 Ga metamorphosed Svecofennian crust. The bimodal lithologies consist predominantly of mafic gabbro-anorthosites plutons and diabase dikes, whereas the felsic counterparts are typically wiborgite and pyterlite granites (Rämö & Haapala 2005). The distinctive feature of rapakivi granites is the presence of ovoidal alkali feldspar phenocrysts in the granite groundmass, and are classified as wiborgite if the alkali feldspar phenocrysts are mantled by a rim of plagioclase, and pyterlite if the plagioclase rims are absent, although alkali feldspar ovoids are not a prerequisite for a rapakivi classification (Rämö & Haapala 2005).

Rapakivi granites are typically iron-rich, contain high amounts of alkali feldspar, and are enriched in many incompatible trace elements (e.g. Zn, Ga, Rb, Zr, Nb, Sn, REE, Th, U). Granite magmatism within the Wiborg batholith may be divided into three main stages based on textural and mineralogical criteria: the early phases are marked by coarse-grained or porphyritic wiborgite and pyterlite assemblages (hastingsite, annite/siderophyllite, and fayalite), and the main intrusive phase is represented by even-grained or porphyritic biotite granites. The last stage granites are typically leucocratic topaz-bearing microcline granites, which may be even-grained or porphyritic, and are occasionally associated with greisen mineralizations and pegmatite intrusions (Rämö &

Haapala 2005).

A-type samples (LOV-1 to -6) were collected near the boundary between the Wiborg batholith and the Svecofennian crust (Fig. 1). LOV-1 to -4 were sampled in the Sarvlaxviken bay area, which hosts two main generations of polymetallic greisenized veins (Valkama et al. 2016). With respect to the (inferred) temporal relationships between LOV-1 to -4, LOV-1 and -2 (wiborgite) represent early stage magmas, LOV-3 ("Marviken granite", c.f. Valkama et al. 2016) is intermediate (but does not necessarily represent a main phase), and LOV-4 ("Hormnäs granite") is the youngest deposit within the Sarvlaxviken bay area (Valkama et al. 2016). LOV-5 and -6 were sampled some 10 km northeast of the Sarvlaxviken bay area, but their temporal association with LOV-1 to -4 are unknown. However, based on textural and mineralogical criteria, they are likely affiliated with the early granite magmatism of the Wiborg batholith.

2.2. Västervik metasedimentary formation

The Västervik formation is an accretionary metasediment basin located at the southwestern margin between the c. 1.9 Ga Svecofennian Domain and the c. 1.85 – 1.80 Ga Transscandinavian Igneous Belt (TIB). The metasedimentary sequence was deposited c. 1.88 – 1.85 Ga (Kleinhanns et al. 2012), which was subsequently intruded by TIB plutons that facilitated the metamorphic re-working and anatexis of the sedimentary basin (Nolte et al. 2011, Reed 2013, Kleinhanns et al. 2015).

The Västervik formation hosts the Olserum REE ore mineralization some 30 km due NW from the city of Västervik (Reed 2013). The REE ore is accommodated mainly in hydrothermally altered metasedimentary veins near the contact of TIB granites and Västervik metasedimentary units. The Olserum granites are typically medium-grained, massive to weakly foliated, and exhibit low mica contents. Sporadic granite-metasediment assimilation structures are associated with the granite-metasediment contact zone, and macroscopically the Olserum granites display a reddish tint (Reed 2013).

According to the proposed Västervik granitoid classification of Nolte et al. (2011), the

sampled Olserum granite (OLR09, Fig. 2) is a Cordilleran S-type Monzogranite (MG), which is related to a c. 1.85 – 1.81 Ga compressional system following a c. 1.88 – 1.85 Ga extensional A-type magmatic regime (Nolte et al. 2011, Kleinhanns et al. 2015). However, this is contradicted by Andersson et al. (in press), who propose that the Olserum granites are likely of shallow AG (anatectic granite) origin, which are subsequent to the Cordilleran type granites (Nolte et al. 2011, Kleinhanns et al. 2015, Andersson et al. [in press]). Thus, it is indicated that OLR09 may not be representative sample of the Olserum REE-affiliated granites, or that the Olserum granites are more diverse than previously believed.

2.3. Hattu schist belt

The supracrustal rocks of the Hattu schist belt consist predominantly of 2.76 – 2.75 Ga felsic epi- and pyroclastic deposits that host several basalt, komatiite, and granitoid intrusions (NAR-1, VIG-1, KUI-3, Fig. 3; Sorjonen-Ward et al. 2015). There are a number of known economic gold deposits within the Hattu schist belt that are often associated with metamorphosed and deformed units (e.g. the Pampalo mine, Fig. 3). These gold mineralizations are roughly concurrent with sediment deposition and sometimes affiliated with granitoid intrusions, e.g. the Kuittila tonalite (Sorjonen-Ward et al. 2015). NAR-1, VIG-1, and KUI-3 represent three disctinc granitoid plutons within the Hattu schist belt: the Naarva leucogranite, the Viluvaara granodiorite, and the Kuittila tonalite, respectively.

The c. 2.70 Ga Naarva leucogranite is a syntectonic, elongate pluton that streches up to 20 km in the northwestern part of the Hattu schist belt. The granites hosted by the Naarva pluton vary from aplitic to pegmatitic, and the general mineralogy is marked with muscovite, biotite, tourmaline, and accessory garnet. The country rocks are predominantly metasedimentary, but metamorphosed felsic volcanic units are also present. The leucogranites are interpreted to have formed mainly by crustal anatexis of older sedimentary rocks (O'Brien et al. 1993, Sorjonen-Ward 1993).

The central parts of the Hattu schist belt are bounded in the east by the late-stage Viluvaara granodiorites, which are typically medium-grained, and marked by 3 – 4 cm

K-feldspar phenocrysts (which are not present in VIG-1), biotite, epidote, and chlorite. The age of the Viluvaara granodiorite is poorly constrained, but an age of c. 2.75 ± 0.2 Ga has been indicated in literature (Sorjonen-Ward 1993).

The c. 2.75 Ga Kuittila tonalite is a relatively small (c. 12 km^2), predominantly foliated, medium-grained, lenticular biotite tonalite intrusion located in the southern part of the Hattu schist belt. The central parts of the pluton are leucocratic trondhjemitic rock, whereas the main bulk of the intrusion is represented by biotite tonalite. Hydrothermal alteration zones within the Kuittila tonalite are associated with gold deposits, which are marked by the destruction of primary plagioclase and biotite, and the introduction of replacement minerals (e.g. quartz, sericite, calcite). The comparatively unaltered tonalities may exhibit replacement assemblages, but are generally undeformed apart from polygonal mosaic textures within quartz and biotite (Sorjonen-Ward 1993, Sorjonen-Ward et al. 2015).

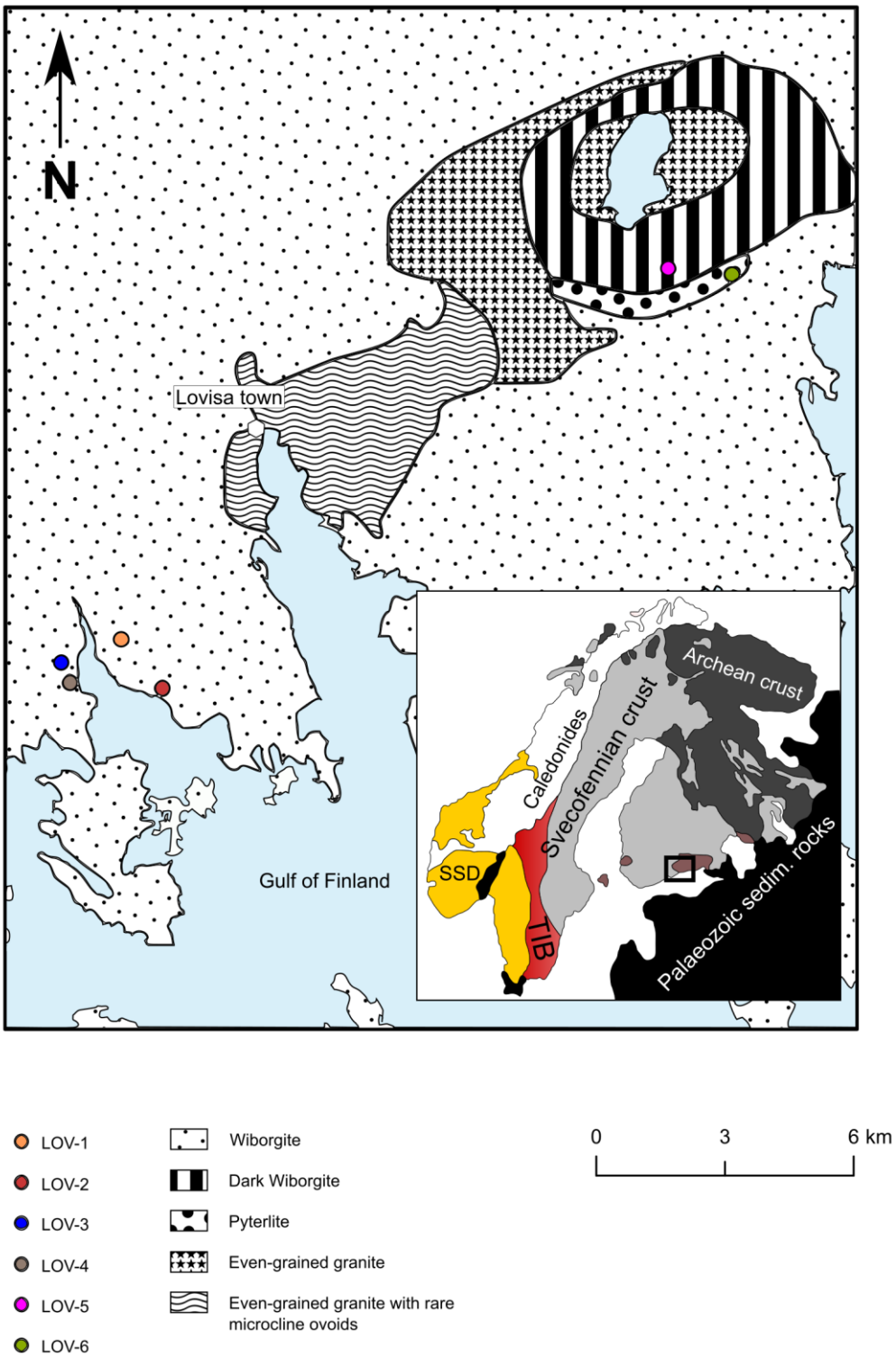

Figure 1. Sketch map of the Lovisa area sampling sites (LOV-1 to LOV-6) and geology. Modified and redrawn after Valkama et al. (2016, Fig. 2). Geological map of the Fennoscandian Shield indented. SSD = Southwest Scandinavian Domain; TIB = Transscandinavian Igneous Belt.

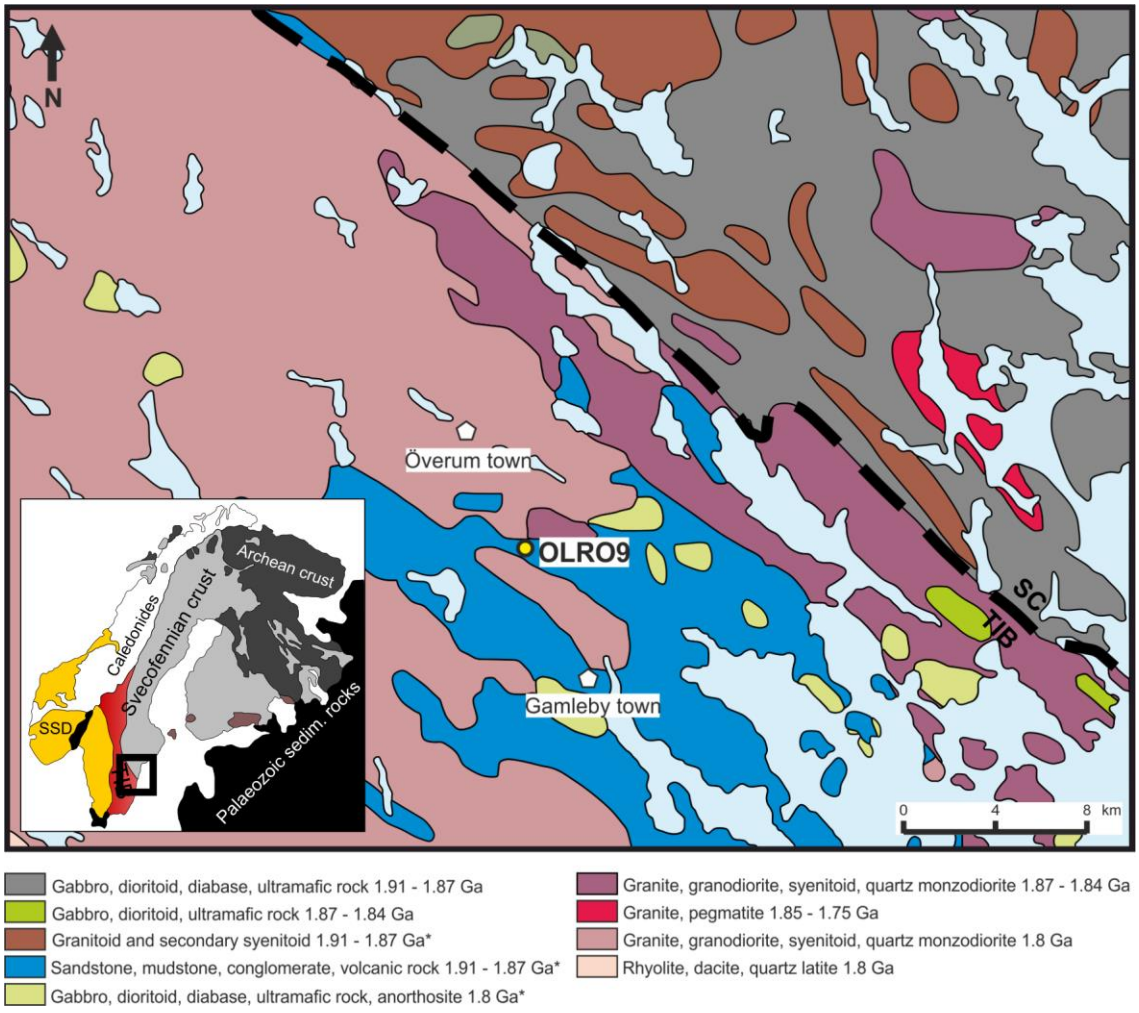

Figure 2. Sketch map of the Olserum sampling site (OLR09) and surrounding geology. Rock types denoted by asterisk (*) include metamorphosed rocks. Based on a 1:250,000 electronic bedrock map of the Västervik area provided by the Geological Survey of Sweden (2017). Geological map of the Fennoscandian Shield indented. SC = Svecofennian Crust; SSD = Southwest Scandinavian Domain; TIB = Transscandinavian Igneous Belt.

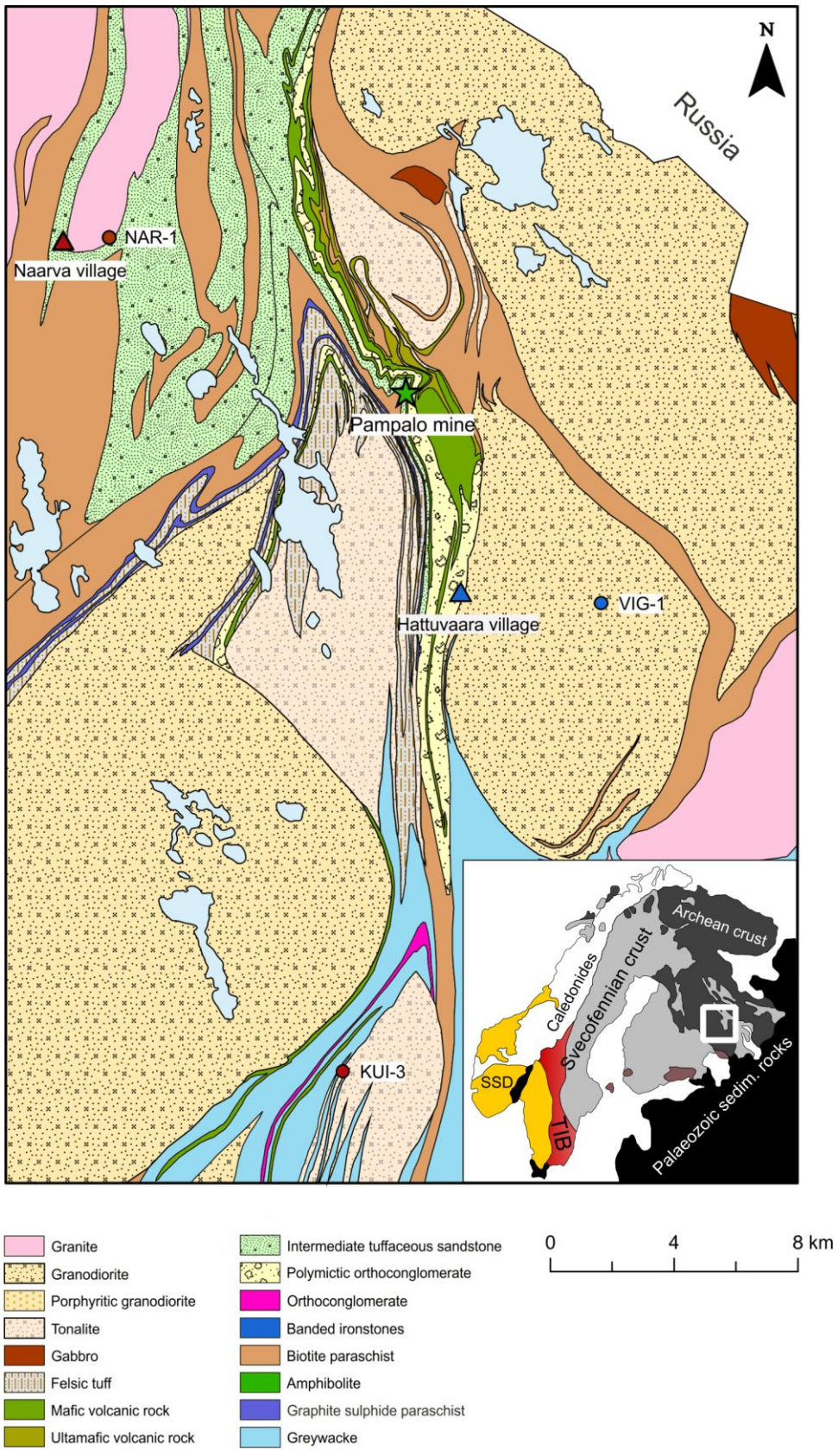

Figure 3. Sketch map of the Hattu schist belt sampling sites (NAR-1, VIG-1, and KUI-3) and geology. Based on an electronic scale-free (i.e. a composite of different scales) bedrock map of the Ilomantsi area provided by the Geological Survey of Finland (2017). Geological map of the Fennoscandian Shield indented. SSD = Southwest Scandinavian Domain; TIB = Transscandinavian Igneous Belt.

3. MATERIALS AND METHODS

The samples were collected in three parts: the first six Lovisa (LOV-1 to -6) samples were sampled mainly from large boulders by the author, Tobias Fusswinkel, and Anselm Loges near the town of Lovisa in southeastern Finland (Fig. 1). One sample (ORL09, Fig. 2) was provided by Stefan Andersson from the University of Helsinki research project "Quantitative constraints on the formation of hydrothermal rare earth element deposits", and three samples (NAR-1, VIG-1, KUI-3, Fig. 3) were provided by Tobias Fusswinkel and Henrik Kalliomäki from the University of Helsinki research project "Chemical controls on gold transport and deposition in orogenic lode-gold systems". Brief macroscopic descriptions of the samples are provided in Table 2, sampling site coordinates in Table 1, and macroscopic sample photographs in Fig. 4.

Table 1. Sampling locations in ETRS-TM35FIN geodetic datum.

Sample	N	E
LOV-1	6698511	455031
LOV-2	6697493	455888
LOV-3	6698026	453789
LOV-4	6697613	453974
LOV-5	6706228	466401
LOV-6	6706102	467727
OLR09*	6423498	580091
NAR-1	6995701	706819
VIG-1	6984860	721396
KUI-3	6970983	713747

* = SWEREF99 TM.

Table 2. Macroscopic (i.e. hand-size) descriptions of study samples.

Sample	Field name	Locality	Texture	Grain size	Felsic minerals	Mafic minerals
LOV-1	Wiborgite granite	Wiborg batholith	Phaneritic, inequigranular, porphyritic	Coarse	Kfs + plag + q	Bt + hbl
LOV-2	Wiborgite granite	Wiborg batholith	Phaneritic, inequigranular, porphyritic	Coarse	Kfs + plag + q	Bt + hbl
LOV-3	Equigranular rapakivi granite	Wiborg batholith	Phaneritic, equigranular	Medium	Kfs + plag + q	Bt
LOV-4	Equigranular rapakivi granite	Wiborg batholith	Phaneritic, equigranular	Medium	Kfs + plag + q	Bt + hem
LOV-5	Porphyritic rapakivi granite	Wiborg batholith	Phaneritic, inequigranular, porphyritic	Coarse	Kfs + plag + q	Bt
LOV-6	Dark wiborgite granite	Wiborg batholith	Phaneritic, inequigranular, porphyritic	Coarse	Kfs + plag + q	Bt
OLR09	Two-mica granite	Olserum, Västervik	Phaneritic, equigranular	Medium	Kfs + plag + q	Bt
NAR-1	Two-mica leucogranite	Hattu schist belt	Phaneritic, equigranular, weakly foliated	Medium	Kfs + plag + q	Bt + ms + grt
VIG-1	Granodiorite	Hattu schist belt	Phaneritic, equigranular, weakly foliated	Medium	Kfs + plag + q	Bt + ep + hbl
KUI-3	Tonalite	Hattu schist belt	Phaneritic, equigranular, weakly foliated	Medium	Plag + q	Bt + hbl

Kfs = K-feldspar; q = quartz; plag = plagioclase; bt = biotite; hbl = hornblende; hem = hematite; ms = muscovite; ep = epidote; grt = garnet.

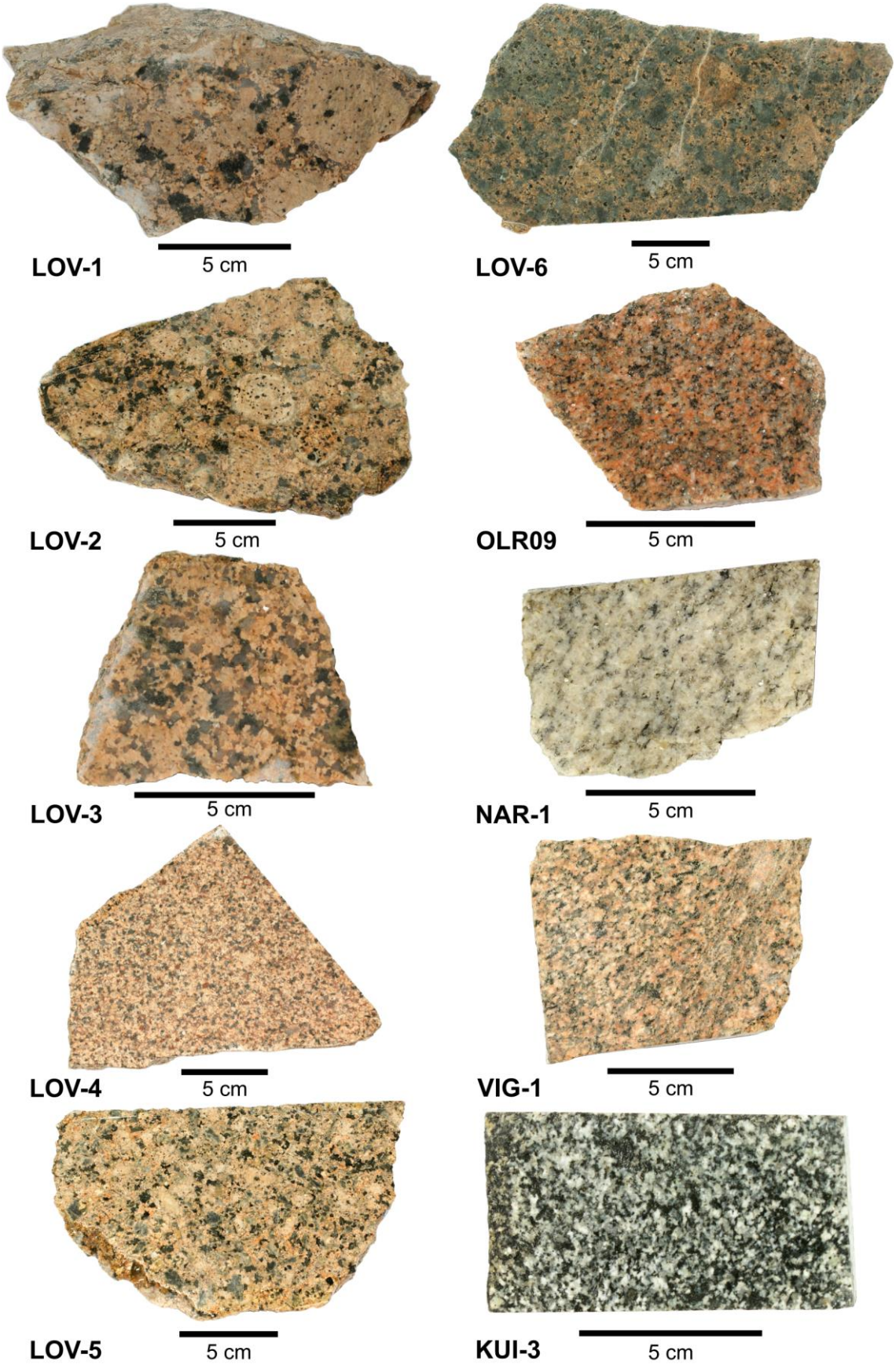

Figure 4. Sample hand-specimen.

All ten samples were analyzed by means of optical petrography, X-ray fluorescence spectroscopy (WD-XRF), electron probe microanalysis (WDS-EPMA), and laser ablation inductively coupled mass spectrometry (LA-ICP-MS). Polished thin sections (30 μm) were used for optical petrography and polished thick sections (250 μm) for EPMA and LA-ICP-MS. Relatively homogeneous mineral grains (that contained relatively low amounts of fluid or mineral inclusions and showed no signs of alteration under an optical microscope) were mapped and selected from the thick sections for trace element analysis. The main objective for this study was to analyze biotite trace element compositions, but some additional amphibole and muscovite grains were included in the *in situ* analysis menu due to the low occurrence of (unaltered) biotite phases in three of the samples (LOV-1, LOV-2, and NAR-1).

Alkali flux beads derived from crushed and powdered bulk rock samples were used for XRF analysis. In general, one polished thin section, one polished thick section and two flux beads were prepared for each sample. The exceptions to this rule were LOV-2 and LOV-6, which were commissioned for two thick sections each (LOV-2.1, LOV-2.2 and LOV-6.1, LOV-6.2). The reasoning behind this decision was that LOV-2 and LOV-6 contained mafic mineral-bearing orthoclase ovoids, and the mafic minerals inside the ovoids could be then compared to the mafic minerals outside the ovoids. Optical microscopy later revealed, however, that the ovoid-hosted mafic minerals in LOV-6.1 and LOV-6.2 were highly altered, and since the objective was to select relatively homogeneous mineral grains, ovoid-hosted mafic grains from LOV-6 thick sections were not selected for analysis. Nevertheless, in total, 10 polished thin sections, 12 polished thick sections and 20 flux beads were prepared.

The respective analyzing methods were chosen to measure sample bulk chemistry (XRF) and mineral chemistry (EPMA: biotite, muscovite and amphibole) for use as an internal standard in later LA-ICP-MS studies. LA-ICP-MS was utilized so that the trace element concentrations could be measured as accurately as possible from the minerals of interest.

Unaltered hand-sized specimens were picked from the sample material for further processing. All processing stages, excluding the manufacturing of polished thick sections, were performed or commissioned at the University of Helsinki Department of Geosciences and Geography mineralogical and thin section laboratory facilities. The

unprocessed samples (excluding ORL09) were ca. 20 cm in diameter, or larger, and were cut into smaller more workable pieces with a diamond-bladed CLIPPER CM 501 masonry saw. The resulting rock fragments were then divided into two sample groups based on later processing stages: a) XRF fragments (i.e. rock powder samples for bulk geochemistry), and b) optical petrography, EPMA and LA-ICP-MS fragments (i.e. polished thin/thick section samples for mineral major/ trace element chemistry).

3.1. Bulk rock major and trace element quantification (XRF)

A PANalytical Axios mAX 4 kW wavelength dispersive X-ray fluorescence spectrometer (WD-XRF) was used to measure bulk rock major element oxide compositions in addition to a selection of trace elements (Ba, Ce, Cu, Cr, La, Nb, Ni, Sr, Rb, U, V, Zn, Zr, and Y). The XRF spectrometer was calibrated using 19 Certified Reference Materials (CRM) that cover the chemical variation in natural rocks from basalt to granite. Li-borate flux beads were used as analytes. Two Li-borate flux beads were produced for each of the ten samples. Thus, in total, twenty flux beads were produced. The sample analyte processing stages from rock to flux beads are described below.

Sample rock fragments were split into smaller ca. 5 - 10 cm pieces with a sharp-edged hydraulic presser. The resulting pieces were then crushed into thumb-sized (ca. 0.5 – 2 cm) fragments with a 4 kW CMT 100/150 jaw crusher. The jaw crusher was cleaned of excess dust by brushing and vacuuming. After removing all excess dust, the jaws of the crusher were “washed” by crushing respective leftover sample material before the main sample bulk crushing to minimize contamination from other samples and rock types. The sample bulk crushing products were then subdivided into two groups: (a) “coarser” fraction that were later hand-picked with plastic tweezers for rock powder milling, and (b) “finer” fraction that were later picked for rock powder milling with a disposable plastic spoon (Fig. 5). The reasoning for this grouping was that the results of the “coarse” sample analytes could be compared to the results of the “fine” sample analytes, which were assumed to be more representative of the sample average whole-rock geochemistry.

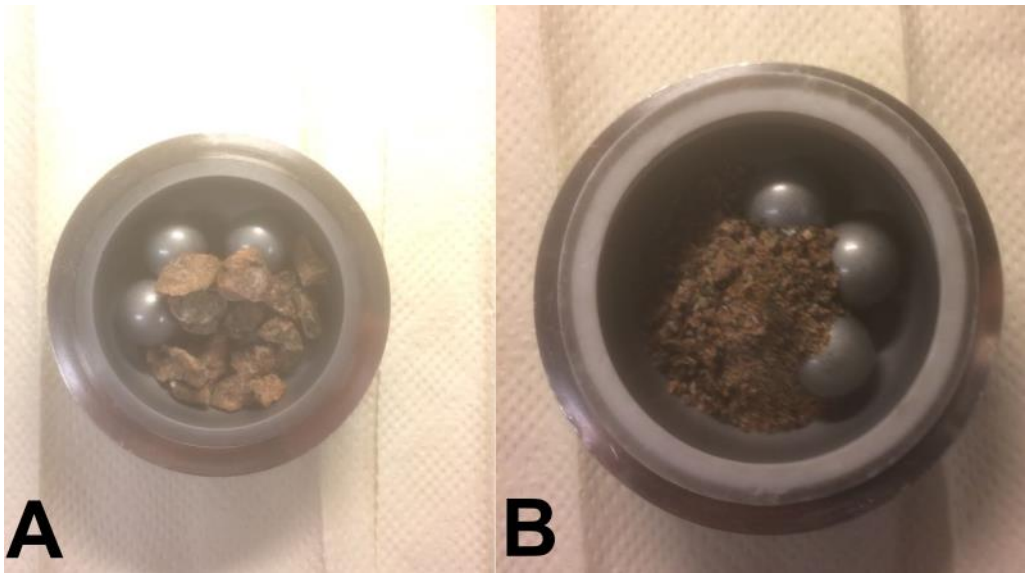

Figure 5. LOV-2 as an example of the “coarse” (A) and “fine” (B) milling fractions.

The crushed sample materials, both the “coarse” and “fine” fractions, were sieved with a plastic ca. 4 mm sift by washing the materials with tap water and ion-exchanged water. The “coarse” fraction sieving products (i.e. sample material that passed the sieve) were discarded, and the remaining sample materials were set into Teflon bowls. In contrast, the “fine” fraction sieving products were decanted with tap water and ion-exchanged water, collected, and put into Teflon bowls. The “fine” fraction sample materials that did not pass the sieve were stored for later potential use. The sample-containing Teflon bowls were then dried in a 105 °C hot air oven overnight.

After drying, 30 g of both the “coarse” and “fine” sample fractions were ground to powder in a Fritsch Pulverisette 6 tungsten carbide ball mill. The tungsten carbide pans were washed with tap water and ion-exchanged water before each milling run, and an additional fine quartzite sand “wash” was milled after every second sample run. The standard procedure is to wash the tungsten carbide pans with quartzite after every sample run. However, if the overall bulk geochemistry is be expected to be similar within the sample group, the samples contain hard abrasive minerals as major phases (such as quartz and orthoclase), and the sample powders do not tend to stick to the tungsten carbide pan surfaces, it may be assumed that the contamination induced by the previously milled sample does not produce an observable anomaly in the bulk composition of the next

sample (Pasi Heikkilä, personal communication 2017).

0.6 g of sample powder was blended with a 6.0 g mixture of lithium tetraborate ($Li_2B_4O_7$ 49.75 %), lithium metaborate ($LiBO_2$ 49.75 %) and lithium bromide (LiBr 0.5 %). The resulting flux mixture was melted with a Claisse M4 Fluxer in a Pt-Au crucible at approximately 1000 °C and cooled in a Pt-Au mold.

Bulk geochemical plotting and the respective calculations were carried out mainly by using the Geochemical Data Toolkit (GCDkit) software package (Janoušek et al. 2006).

3.2. Optical petrography and polished sections

Polished thin and thick section fragments were further refined into approximately 5 cm x 4 cm x 1 cm tablets with a table masonry saw. Polished thin sections were then commissioned at the University of Helsinki Department of Geosciences and Geography thin section laboratory, and polished thick sections at the University of Würzburg Institute of Geography and Geology.

Optical petrography was performed on 30 µm thin sections with a standard transmitted light polarizing microscope. The 250 µm thick sections often proved unfruitful in terms of precise optical microscopy due to the thickness of the sample material. The thick section minerals and microscopic structures were often too dark or cluttered for meaningful identification, however the topmost layer of the section could be identified with relative ease with a reflected light microscope (Fig. 6). A Leica DM2500P petrographic microscope equipped with a reflected light module was used for mineral identification and preparing thick section overview maps. The main objective for optical microscopy was to identify the minerals and textures prior to EPMA analysis. Additional objectives for optical petrography were to define the mode and confirm the rock type (from field observations) for all samples.

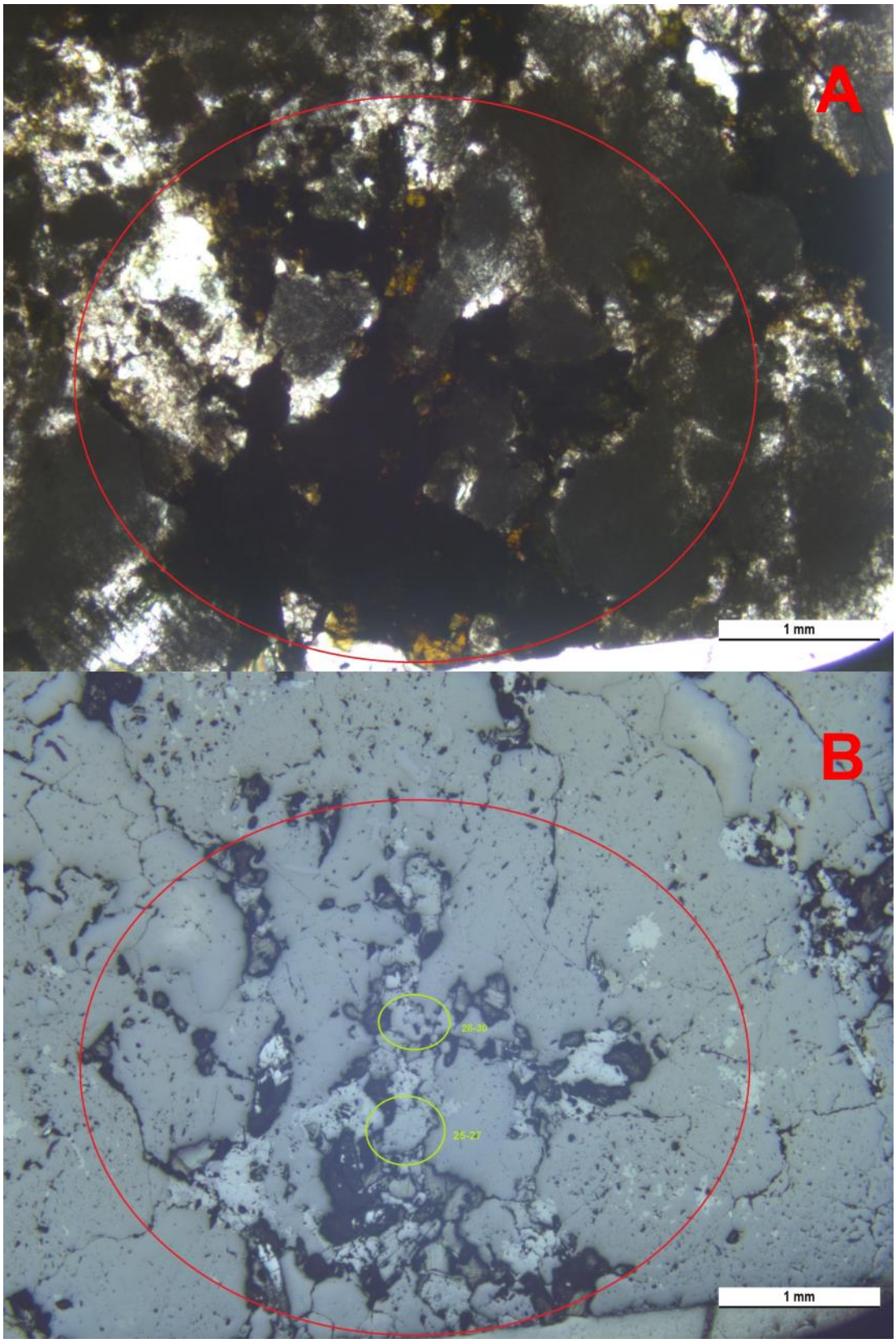

Figure 6. An example (VIG-1) of transmitted light microscopy (A) vs. reflected light microscopy (B). Circled mineral grains indicate planned biotite analysis sites.

3.3. *In situ* major element quantification (EPMA)

The original intent was to measure ten unaltered and relatively inclusion-free biotite grains from each sample, and later measure these same grains for trace elements using LA-ICP-MS, as discussed previously. Reflected light microscopy revealed that mica grains often contained numerous mineral and fluid inclusions, and therefore measurement sites were selected in such a way that the inclusions could be best avoided. For samples LOV-1, LOV-2.1, LOV-2.2, and NAR-1 this proved difficult, however, since biotite grains in the respective samples were (in most cases) either highly altered or filled with inclusions, or both. The respective samples contained amphibole or muscovite grains in addition to biotite, and thus it was decided that amphibole/muscovite grains would replace some of the biotite grains in the measurement plan. The reasoning was that the amount of measured mineral grains per sample would nevertheless total about 10, and the contrasting minerals could then be compared. Thus, three amphibole grains and seven biotite grains were analyzed from LOV-1 (totaling 10 grains), seven amphiboles and three biotites from LOV-2.1 (totaling 10 grains), and two amphiboles and twelve biotites from LOV-2.2 (totaling 14 grains). Seven muscovite and three biotite grains were measured from NAR-1. In total, 125 mineral grains were measured across all samples, out of which 106 were biotites, 12 amphiboles and 7 muscovites. Grains were numbered 1, 2, 3, … *n* after the amount of measured grains in each sample. Two amphibole grains and four biotite grains were later disqualified from results and calculations, however, as LA-ICP-MS measurements revealed that these analysis sites contained mineral inclusions or highly anomalous ablation signals, thus rendering the LA-ICP-MS results unreliable and EPMA results meaningless for the respective mineral grains.

Carbon coated polished thick sections were analyzed using a Jeol JXA-8600 Electron Probe Microanalyzer equipped with four wavelength dispersive X-ray detectors (WDS), an energy dispersive X-ray detector (EDS), and secondary electron (SE) and back scattered electron (BSE) detectors. The detector and sample stages were operated with PointElectronic SAMx hardware coupled to a XMAS/IDFix/Diss5 software package. The objectives for EPMA measurements were a) to measure mineral major element chemistry for use as an internal standard in LA-ICP-MS studies, b) to acquire both BSE and SE images, and c) rapid mineral identification (EDS). Quantitative analyses were acquired

via WDS with a defocused beam of 10 µm, an acceleration voltage of 15 kV, and a beam current of 15 nA. Qualitative analyses were acquired via EDS with an acceleration voltage of 20 kV and a beam current of 1 nA for samples NAR-1, KUI-3 and VIG-1, and an acceleration voltage of 15 kV and a beam current of 4 nA for all the remaining samples. Elements analyzed were Si, Ti, Al, Fe, Mg, Ca, Na, and K. All Fe was assumed to be ferrous. Standards were measured twice, and the following natural and synthetic AstimeX standards were used for mica calibration: plagioclase (Al, Ca), rutile (Ti), hematite (Fe), albite (Na), periclase (Mg), and sanidine (K, Si). Diopside (Si, Mg, Ca), plagioclase (Al), rutile (Ti), hematite (Fe), albite (Na), and sanidine (K) were used for amphibole calibration. Analyte thick sections were cleaned with acetone prior to inserting them into the sample chamber.

Duplicate analyses were measured as a check for homogeneity for some of the grains in six of the samples (LOV-1, LOV-2.2, LOV-4, LOV-5, LOV-6.1, and VIG-1) within an area of approximately 100 µm. The samples, grains, and amount of duplicate measurements per grain are shown in Table 3. Due to mineral alteration, inclusions, and time constraints, duplicate measurements could not be obtained for all grains and samples.

Table 3. Samples, grains, and the amount of duplicate measurements. Mineral grains represent biotite unless specified otherwise.

Sample	Grain numbers	Amount of measurements / grain
LOV-1	2 - 3	3
LOV-2.2	2 (amphibole)	3
LOV-4	1 - 3, 5, 10	3
LOV-4	9	4
LOV-5	4	5
LOV-5	7	3
LOV-6.1	2, 4	3
LOV-6.1	6	4
VIG-1	1 - 10	3

Since only 24 grains out of a total of 125 grains were measured for duplicates, duplicate measurement data were excluded from other calculations, plots, or schemes to remain consistent with the rest of the data. Instead, the spot measured closest to the LA-ICP-MS analysis spot was selected as the most representative data point, and was included in

further calculations and plots.

Micas were identified after the *mgli* classification of Tischendorf et al. (1997, 2001) and the IMA classification of micas (Rieder et al. 1998). Mineral formulae calculations were based on 22 O apfu, according to the principles outlined by Deer et al. (1992). Amphibole mineral formulae and identification were determined on the basis of 24 O apfu using an amphibole classification excel spreadsheet (Locock 2014), which follows the recommendations of the IMA (Hawthorne et al. 2012).

3.4. *In situ* major and trace element quantification (LA-ICP-MS)

Minerals and grains analyzed by EPMA were quantified by means of LA-ICP-MS to quantify accurate trace elements compositions. The LA-ICP-MS measurements were conducted using an Agilent 7900s quadrupole ICP-MS connected to a Coherent GeoLas Pro MV2 193 nm laser ablation system. The ICP-MS results were calibrated by measuring external standards (NIST 610 and GSE-1G) of known composition. Al_2O_3 concentrations (in wt.%) acquired via EPMA analysis were used as internal standards for the corresponding samples and grains. Analyte thick sections were cleaned with acetone prior to inserting them into the sample cell. Concentration calculation and data reduction were made with the MATLAB-based SILLS software (Guillong et al. 2008).

Laser ablation parameters for external standards were 10 J cm^{-2} energy density, repetition rate of 10 Hz, 500 pulses, and a crater size of 60 µm. The respective ablation parameters for unknown samples were 4 J cm^{-2} energy density, 10 Hz repetition rate, 500 pulses, and a crater size of 32 – 90 µm, depending on obstructing inclusions and grain size. Helium was used as a carrier gas with a flow rate of 1.03 L min^{-1}, and argon was used as an auxiliary gas with a flow rate of 0.85 L min^{-1}. Argon plasma gas flow rate was at 15 L min^{-1}. The LA-ICP-MS instrument was calibrated daily by repeated measurements of a NIST 612 standard reference material as an unknown to ensure an accuracy better than 5 %. The aim was to ensure optimal signal-to-background ratios, to reduce oxidation (ThO/Th < 0.5 %), and to hone ablation, transport, and plasma conditions (U/Th = 1.00 ± 0.02).

The elements and respective masses measured for all minerals were ^{7}Li, ^{9}Be, ^{11}B, ^{23}Na, ^{24}Mg, ^{27}Al, ^{29}Si, ^{39}K, ^{44}Ca, ^{45}Sc, ^{49}Ti, ^{55}Mn, ^{56}Fe, ^{57}Fe, ^{59}Co, ^{60}Ni, ^{63}Cu, ^{66}Zn, ^{69}Ga, ^{72}Ge, ^{90}Zr, ^{93}Nb, ^{111}Cd, ^{113}In, ^{115}In, ^{118}Sn, ^{137}Ba, ^{146}Nd, ^{162}Dy, ^{165}Ho, ^{178}Hf, ^{181}Ta, and ^{208}Pb. The dwell time was set at 0.02 seconds for ^{90}Zr, ^{93}Nb, ^{178}Hf, and ^{181}Ta. A dwell time of 0.01 seconds was used for all remaining elements and masses.

Three spots were measured from both external standards approximately every two to three hours to control and correct for detector drift (instrumental drift corrections are calculated automatically in SILLS). Duplicate spots from unknowns were measured for samples LOV-2.1, LOV-6.1, OLR09, VIG-1, and KUI-3. Again, as with EPMA analysis, duplicate measurements could not be made for all samples and grains due to mineral alteration, inclusions, and time constraints. Duplicate sample measurements were used firstly as a back-up spot (in case either measured spot showed signs of mineral of fluid inclusions) and secondly as a check for homogeneity and trace element fractionation. In total, 156 sample spots were measured (out of which 31 were duplicates) from 125 mineral grains. 119 out of the 156 individual measurements were qualified for further analysis after data selection and reduction (102 biotites, 7 muscovites, and 10 amphiboles).

Out of the duplicate measurements, one spot analysis per mineral grain was selected for plotting and calculations. The spot that was deemed most suitable was selected after the following considerations: (1) which spot was closest to the measured EPMA spot, (2) whether the spot contained inclusions (if so, the inclusion-free spot was favored), (3) whether the ablation interval exhibited anomalous multi-element ablation signals (spots with stable ablation signals were favored), (4) which spot produced a superior ICP/EPMA wt.% major and minor element ratios (i.e. the spot closer to 1.00 overall ratio was selected), and 5) crater size (larger crater size was favored over smaller crater size). It should be noted that sampling bias is introduced when data is cherry picked. However, since the objective was to analyze homogeneous minerals, and anomalous ablation signals result in anomalous concentrations (i.e. interpretation is complex and likely erroneous), and because sensitivity of the LA-ICP-MS system is tied to crater size (Fryer et al. 1995), data selection was used.

3.5. Sources of error and data quality analysis

Geological data is often liable to a myriad of sources of error. Sources of error can be divided into two major categories: analytical and geological error. Analytical errors include machine errors (e.g. when two isotopes are counted as one mass in ICP-MS), calibration, specimen preparation errors (e.g. tools that are used to prepare a specimen may contaminate the sample), which may be introduced in all sampling stages, and statistical errors if summary statistics are used (e.g. selection of relevant statistical parameters). Geological errors often refer to the geological variability of the studied entity and the geological significance of the sampled material, e.g. sample representativeness (Rock et al. 1987, Rock 1988).

During XRF analyte preparation, the most substantial sources of contaminants originate from specimen crushing and milling. The jaw crusher may contaminate the specimen if rock fragments from prior usage are lodged between or adhered on jaw surfaces (e.g. soft carbonate minerals). Additional steel alloy contaminants may be imparted on the crushed material from crusher surfaces, most notably Fe, Cr, and Ni. Similarly, milling infects the specimen with W, Co, and Ta in trace element quantities.

The main sources of contaminants in EPMA and LA-ICP-MS originate from grinding the specimen with a copper-bonded diamond wheel during section preparation. Thus, Cu surface contaminations were somewhat common (Fig. 7). Ca was observed, although less frequently, as a surface contaminant. However, since surface contaminants (and sub-surface contaminants, i.e. inclusions) were identifiable, large scale sample contamination was avoidable, unlike in XRF analysis.

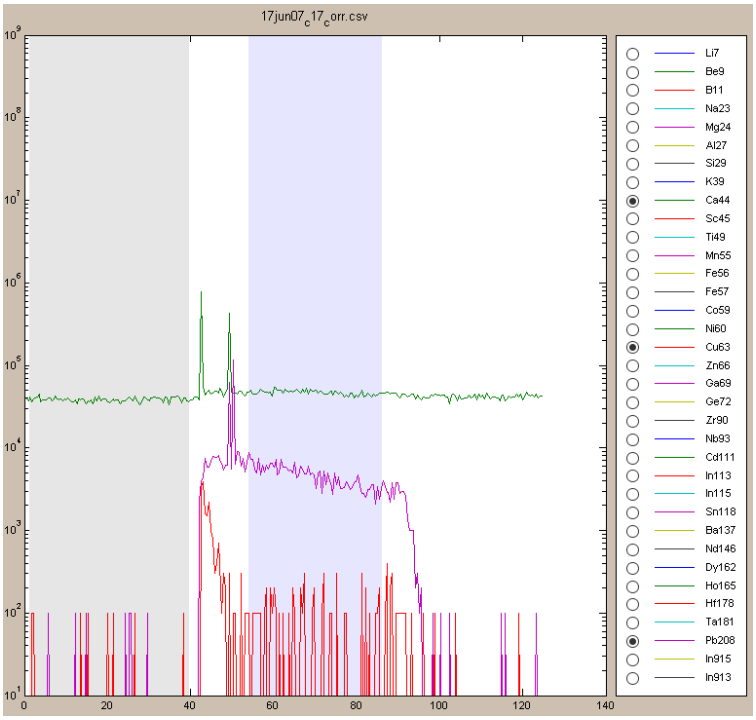

Figure 7. An example of surface contamination (LOV-2.1 biotite grain 1) from SILLS. Grey area indicates the gas blank and blue area is the user-defined ablation signal integration interval. Green line refers to ^{44}Ca, red line to ^{63}Cu, and purple line to ^{208}Pb.

3.5.1. EPMA data quality

Biotite, sanidine, and diopside standards of known composition were measured once as unknowns (Appendix 1). For the biotite standard, the relative accuracy of the EPMA analysis was approximately 95 % for Si, Al, Fe, and Mg oxides, while for TiO_2 the relative accuracy was about 55%, and 99% for K_2O. A relative accuracy of about 99 % was measured for both the sanidine and diopside major element oxides. Since there were no repeated analyses, the overall precision is unknown and the above-mentioned relative accuracies should be considered as approximations. The low relative accuracy of TiO_2 in the biotite standard may be attributed to the fact that the standard of known composition is inhomogeneous, and the minor element concentrations are also close to the limits of detection, which increases the uncertainty in both the measured composition and the certified concentration provided by the standard manufacturer. Thus, the TiO_2 standard, and possibly sample, concentrations may be erroneous in biotites.

The range of wt.% values from the duplicate grain analyses are summarized in Table 4. Homogeneity was evaluated by calculating the ratio of maximum/minimum (max/min) wt.% values for all oxide elements in each grain. In general, all grains appear relatively

homogeneous in terms of SiO_2, Al_2O_3, and FeO. MgO and K_2O behave similarly for the most part, however two MgO outliers in LOV-6.1 and two K_2O outliers VIG-1 produced high max/min ratios. Concentration ratios of TiO_2, CaO, and Na_2O are much more varied, which reflects that either the minerals are largely heterogeneous in terms of these oxides, or that high analytical error is associated with TiO_2 and the other element concentrations that are close to the limits of detection (Table 8 in Results), or both. The inaccuracies that surfaced when standards of known composition were measured as unknowns implies analytical error. Yet, if biotite max/min ratios are compared to amphibole (LOV-2.1) max/min ratios, duplicate measurements from amphibole hint that the relatively high max/min ratios in some biotites could be attributed to heterogeneity. However, it is unknown whether low max/min ratios are characteristic to amphiboles, since only one amphibole grain was measured for duplicates, so it is uncertain whether the variation in homogeneity is purely a function of analytical error or sample heterogeneity. It is also unknown if oxide phases would have shown similar behavior in all samples. Nonetheless, amphibole and mica mineral formulae recalculation produced coherent and consistent results (Tables 8, 9, 10), which indicates that the overall accuracy and reproducibility are satisfactory. Full major element data for the respective grains and measured spots can be found in Appendix 2.

Table 4. Calculated minimum and maximum wt.% difference values from all duplicate analyses. The maximum wt.% value (e.g. 34% SiO_2) was divided by the respective minimum value (e.g. 33% SiO_2) in all duplicate analyses for all oxide elements, thus producing a minimum and a maximum difference value for a given oxide element. The "Min. difference" row indicates the lowest calculated minimum difference value from all duplicate analyses for a given oxide element (e.g. SiO_2), whereas "Max. difference" row indicates the respective maximum difference value. That is, the lowest and highest calculated difference values from 24 duplicate analyses were 1.00 and 1.04 for SiO_2, respectively.

	SiO_2	TiO_2	Al_2O_3	FeO	MgO	CaO	Na_2O	K_2O
Min. difference	1.00	1.06	1.01	1.01	1.01	1.00	1.00	1.01
Max. difference	1.04	2.07	1.05	1.06	1.43	2.48	1.62	1.14

3.5.2. LA-ICP-MS data quality

LA-ICP-MS data quality was assessed by comparing LA-ICP-MS analysis data to the respective EPMA data. Data provided by LA-ICP-MS analyses can be viewed as more reliable than that of EPMA for trace elements due to the higher sensitivity achieved by LA-ICP-MS, and because the ablation integration interval can be inspected for heterogeneities (Ranta 2017).

Element concentrations were calculated using both NIST 610 and GSE-1G. The latter was selected for further calculations, plotting and representation, however, as the ratios of LA-ICP-MS major element compositions to EPMA major element compositions were closer to 1.00 with GSE-1G (on average for biotite grains). That is, an ICP-MS/EPMA ratio of 1.00 indicates a 1:1 correlation between the measured ICP-MS and EPMA concentration.

For example, the average ICP-MS/EPMA ratio for ^{56}Fe, using GSE-1G, was about 0.96, and 0.81 using NIST 610. Likewise, the average ICP-MS/EPMA ratio for Si was about 0.99 for GSE-1G and 0.97 for NIST 610. In contrast, the Ti average ratios were 1.18 and 1.05, respectively. Considering that Ti concentrations were below 3 wt.% in biotites, and Fe concentrations ranged from about 12 wt.% to 28 wt.% (Table 8 in Results), more accurate Fe compositions were favored over Ti. Similar behavior was observed for Ti in muscovite and amphibole grains. Therefore, all reported ICP-MS Ti values are subject to a systematic error of about 15 – 20 %. The systematic error may result from the fact that the GSE-1G standard contains only 400 ppm Ti, and Ti concentrations were estimated in the wt.% range, which is two orders of magnitude higher than the standard concentration. Thus, if the analyzed Ti content in *GSE-1G* is higher or lower than 400 ppm (due to standard heterogeneity), a significant systematic error is introduced into *unknown* concentration calculations.

The ICP-MS/EPMA relationships are illustrated more clearly in Fig. 8, as summary statistics can be misleading (Rock 1988). Al is omitted from the figure since it was used as the internal standard, resulting in inherent 1:1 correlation. Data points in Fig. 8 represent individual mineral analyses.

All major elements approximate 1:1 correlation, although not perfectly. This is true especially for Ca and Na in biotites, where EPMA concentrations are much higher than the ICP-MS counterparts. The disparity results presumably from instrument sensitivity in addition to Na and Ca volatility under the microprobe electron beam. The closest fit to 1:1 correlation is exhibited in Mg. Si and Fe EPMA concentrations tend to be slightly higher for biotites and amphiboles, while for Si in muscovites the opposite is true. ICP-MS titanium concentrations tend to be higher for all minerals, as previously discussed.

However, for muscovites this cannot be stated with any degree of certainty due to the low number of samples: only one EPMA measurement was above the statistical detection limit (at a 95 % confidence level). Analyzed K mica concentrations are also higher for ICP-MS, although not as dramatically as with Ti. However, the respective K amphibole concentrations approximate a close 1:1 fit. As for the cause of these discrepancies, the deviations between ICP-MS and EPMA values may be caused by standardization and calibration errors in either apparatus.

Pearson product-moment coefficients of linear correlation (hereafter *r*) are listed in Table 5 for the measured major elements (ICP-MS and EPMA). The correlation coefficients were calculated from a combined array of all minerals. All major element correlations are statistically significant at the 95 % confidence level. The calculated correlation coefficients support the observations derived from ICP-MS/EPMA ratios and the respective scatter plots.

Table 5. Pearson product-moment coefficients of linear correlation calculated for all major elements from the respective LA-ICP-MS and EPMA measurements. All reported values are statistically significant at the 95 % confidence level.

	Si	Ti	Al	Fe	Mg	Ca	Na	K
r	0.93	0.93	1.00	0.99	1.00	1.00	1.00	0.98

All additional correlation coefficients reported hereafter are statistically significant at the 95 % confidence level, unless stated otherwise.

Spectral interferences are created by multitude of sources (e.g. other elements in the sample or oxygen in the air) in ICP-MS measurements. As element concentration calculations are based on mass/charge ratios, polyatomic and isobaric interferences are introduced when two (or more) atomic ions are counted as one particle, or when two different isotopes of the same mass are counted as one element. For instance, an $^{40}Ar^{16}O^{+}$ ion entering the ion detector would get counted as mass 56, which is also a major isotope of iron, $^{56}Fe^{+}$. Similarly, a $^{113}Cd^{+}$ isotope would get counted as $^{113}In^{+}$, or vice versa, depending on the element of interest. One way to compensate for spectral interferences is to use interference correction calculations. For example, to estimate the "true" intensity of an element, such as $^{113}In^{+}$, the interfering isotopes or species are measured at another mass. Provided that another mass is free of interferences, the intensity of the interfering

isotope is ratioed to the intensity of the alternate mass and a correction is calculated on the basis of their relative isotopic abundances. For example, the interfering isotope for $^{113}In^{+}$ is $^{113}Cd^{+}$. An interference free isotope $^{111}Cd^{+}$ is measured, and a correction is applied (Thomas 2013, Berni et al. 2017):

$$^{113}In^{+} = \text{total counts at mass } 113 - (^{113}Cd^{+}/^{111}Cd^{+}) \times (^{111}Cd^{+}), \quad [1]$$

where ($^{113}Cd^{+}/^{111}Cd^{+}$) is the ratio of the natural abundances of the two isotopes. Spectral interference corrections were calculated in similar fashion with in-house software for isotopes $^{113}In^{+}$ and $^{115}In^{+}$ with $^{111}Cd^{+}$ and $^{118}Sn^{+}$ as the respective reference isotopes.

Isobaric interference correction calculations produced mixed results for ^{113}In and ^{115}In (Figs. 9 and 10). Based on viewing Fig. 9 alone, *corrected* ^{113}In concentrations seem to correlate better with ^{111}Cd than the respective *uncorrected* concentrations. In theory, the opposite should occur. The coefficient of linear correlation for *corrected* ^{113}In and ^{111}Cd is 0.40 with 12 degrees of freedom, which means that the calculated correlation coefficient is statistically insignificant at the 95 % confidence level. Yet, if the two outliers in Fig. 9 B (corrected) are removed, r = 0.81, and the null hypothesis can be rejected. The respective r -values in Fig. 9 A (uncorrected) are 0.79 (with outliers) and 0.96 (without outliers). Based on the calculated correlation coefficients, with or without outliers, the correlations behave as expected, i.e. *corrected* ^{113}In correlates less with ^{111}Cd than the *uncorrected* counterparts. Thus, it could be argued that the isobaric correction calculations for ^{113}In achieved their purpose. However, it should be noted that ^{111}Cd was below detection limit in most analyses, and that *corrected* ^{113}In concentrations are often higher than *uncorrected* ^{113}In. This results from high Cd concentrations in the standard material, which is reflected in the standard measurements. Because the Cd content is high in the standard, but mostly below detection limit in biotite, ^{113}In concentrations are underestimated in the samples due to interference effects in the external standard as spectral interference corrections are applied both to the standard and sample measurements (Berni et al. 2017).

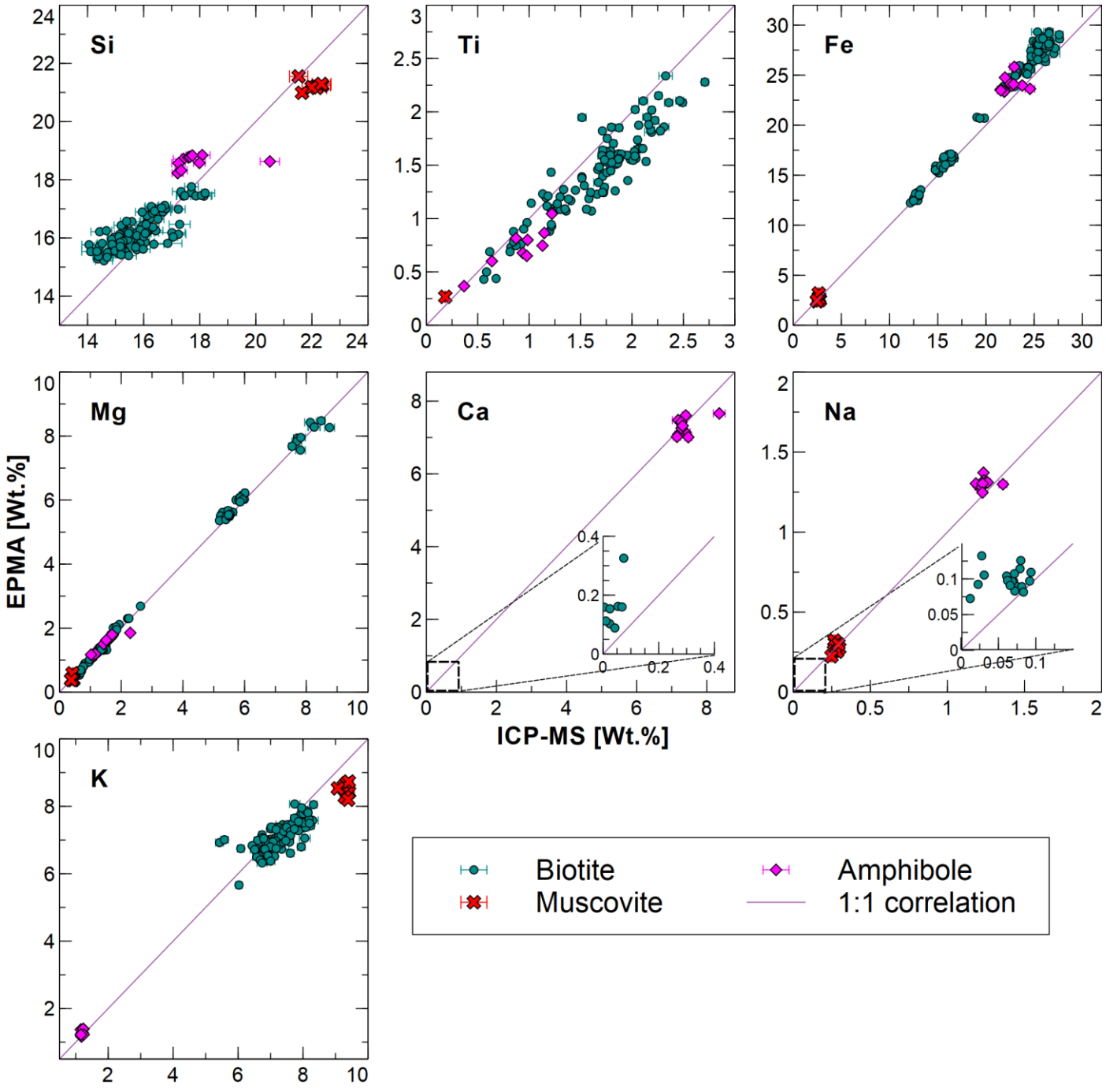

Figure 8. Comparison of ICP-MS concentrations (calculated via GSE-1G) to EPMA-WDS concentrations. ICP-MS data as the abscissa and EPMA data as the ordinate. Axis values are in wt.%. Error bars indicate a combined 1 σ of LA-ICP-MS transient signal noise and counting statistical errors.

^{115}In correction calculations produced more consistent results. Based on viewing Fig. 10, *uncorrected* ^{115}In concentrations tend to be higher than the respective *corrected*

concentrations. Moreover, the correlation between *uncorrected* ^{115}In and ^{118}Sn is more evident than in the respective *corrected* concentrations. The *uncorrected* ^{113}In and ^{115}In concentrations are less well-correlated than the *corrected* concentrations, as is expected, assuming that the reported ^{113}In concentrations are reliable. Calculated correlation coefficients support these observations: in the ^{118}Sn -plots, r = 0.84 for the *uncorrected* concentrations and r = 0.56 for the *corrected* concentrations. For the In/In plots, r = 0.73 for the *uncorrected* concentrations and r = 0.97 for the *corrected* concentrations. Therefore, it is argued that the *corrected* ^{113}In and ^{115}In concentrations are reliable with respect to isobaric interferences.

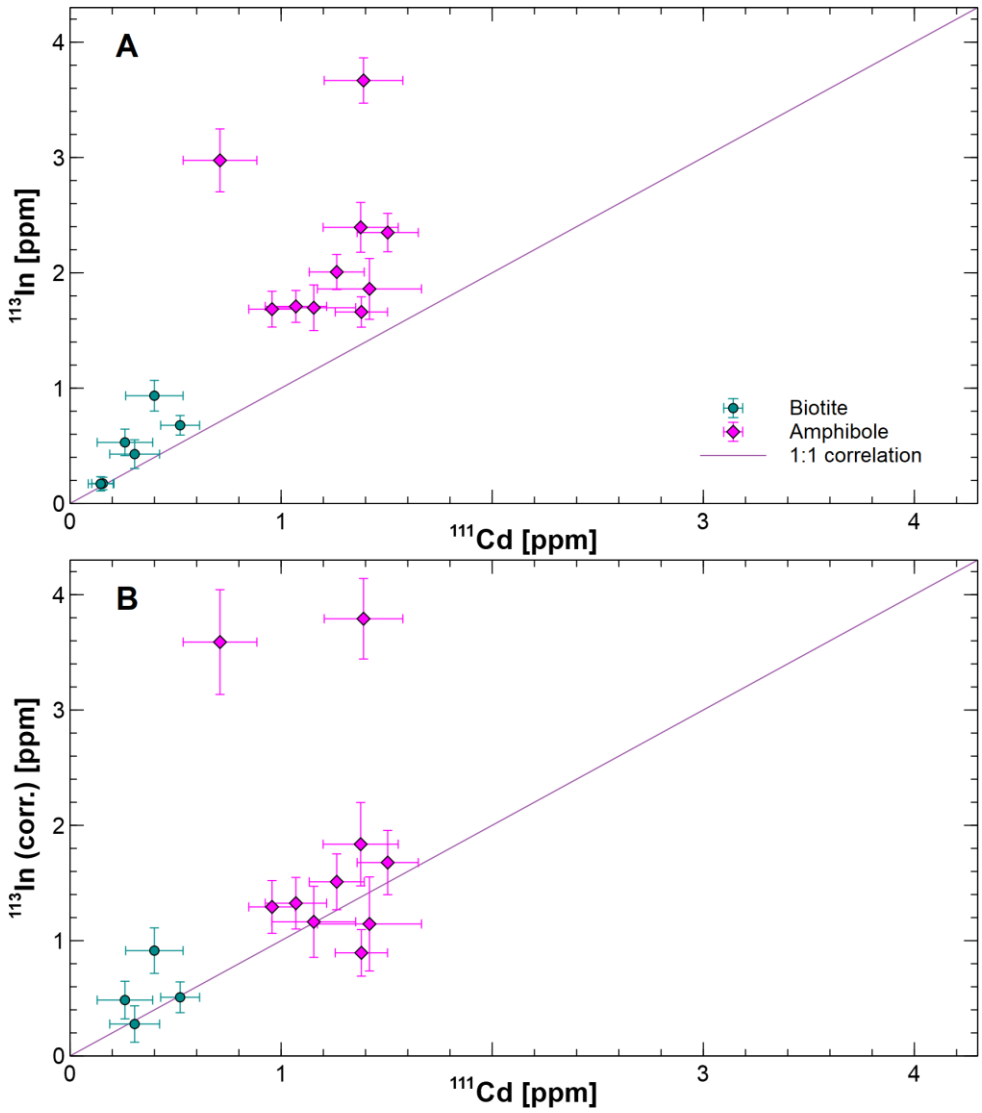

Figure 9. ^{111}Cd vs. ^{113}In scatter plots. (A) ^{111}Cd vs. *uncorrected* ^{113}In. (B) ^{111}Cd vs. *corrected* ^{113}In. Note that "^{111}Cd [ppm]" and "^{113}In [ppm]" refer to the total Cd and In concentrations calculated from masses 111 and 113, respectively. Error bars indicate a combined 1 σ of LA-ICP-MS transient signal noise and counting statistical errors.

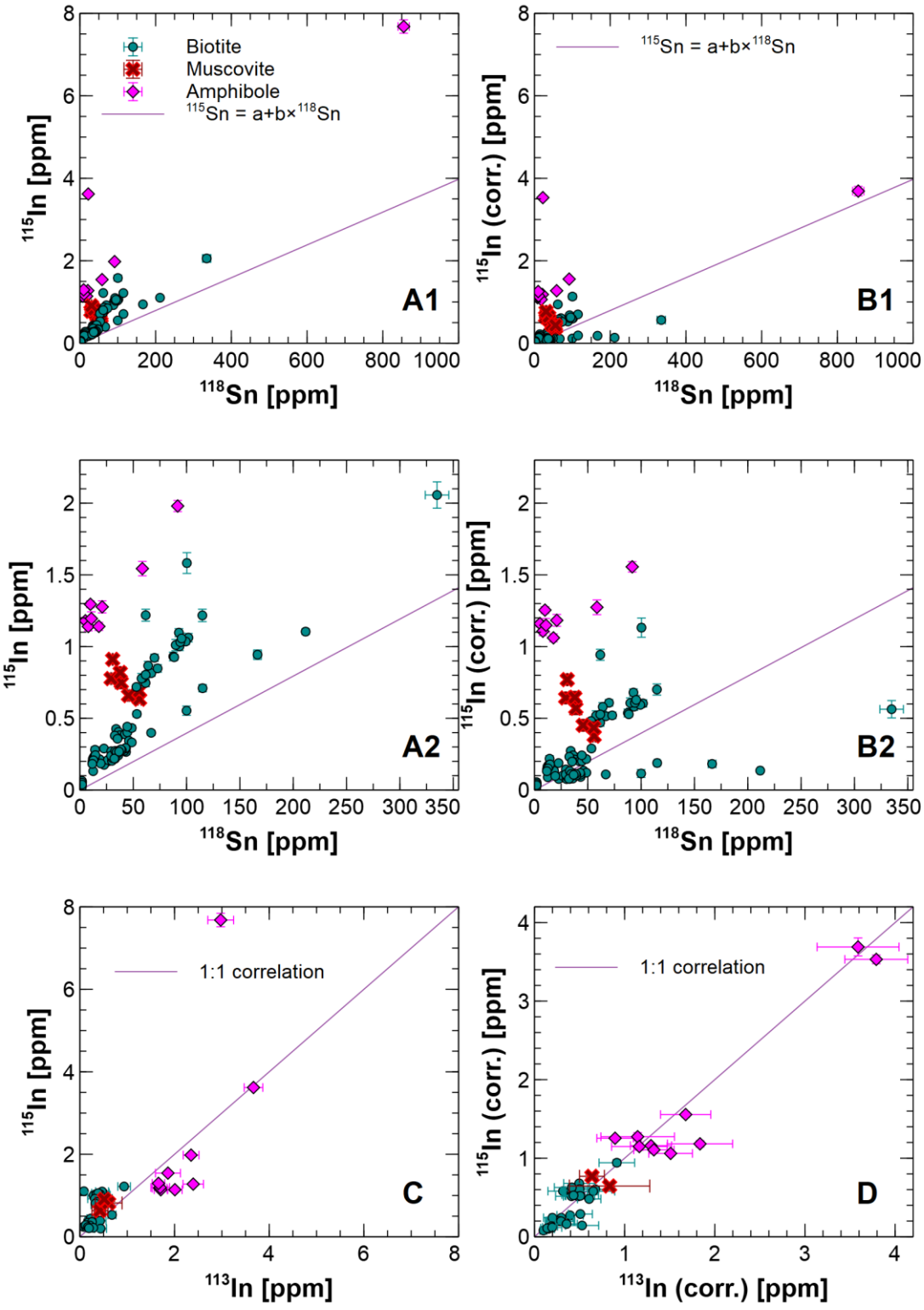

Figure 10. ^{118}Sn vs. ^{115}In scatter plots. (A1) and (A2) represent ^{118}Sn vs. *uncorrected* ^{115}In. (B1) and (B2) represent ^{118}Sn vs. *corrected* ^{115}In. (C) and (D) represent *corrected* and *uncorrected* ^{113}In vs. ^{115}In. Note the different scales. Furthermore, note that "^{113}In [ppm]", "^{115}In [ppm]", and "^{118}Sn [ppm]" refer to the total In and Sn concentrations calculated from masses 113, 115, and 118, respectively. The regression line (y = a + bx) in (A) and (B) represents the function of ^{115}Sn and ^{118}Sn concentrations. The regression line in (C) and (D) represents 1:1 correlation. Error bars indicate a combined 1 σ of LA-ICP-MS transient signal noise and counting statistical errors.

Spectral interferences for ^{56}Fe were evaluated by comparing ^{56}Fe abundances to ^{57}Fe. Since the Fe abundances based on analysis of the masses 56 and 57 approximate a 1:1 correlation (Appendix 3) – i.e. spectral interferences are largely insignificant – and ^{56}Fe is the more abundant isotope, ^{56}Fe concentrations were used for ICP-MS-related Fe plotting and calculations.

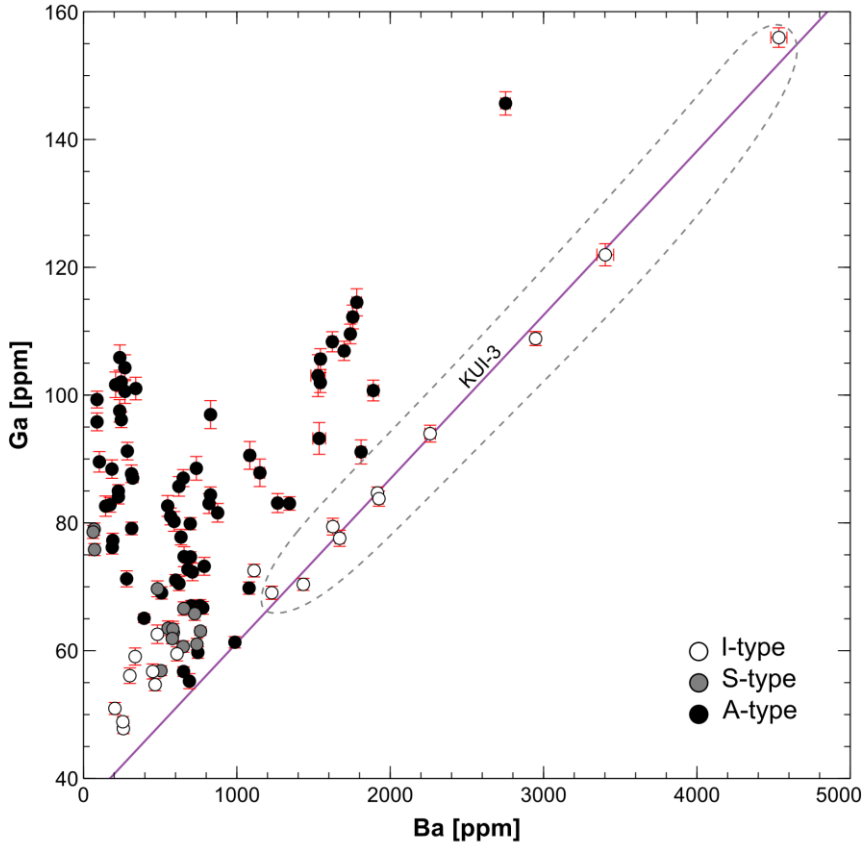

Figure 11. Biotite variation diagram. Interference on ^{69}Ga caused by doubly charged ^{138}Ba resulted in a linear correlation between the two elements in KUI-3 (outlined by dashed grey line). The purple line represents a linear function fit through the KUI-3 Ga-Ba data. It is assumed that KUI-3 contains no Ga, and the apparent Ga concentrations are, in stead, caused by the doubly charged Ba interference (see text below for discussion). Error bars indicate a combined 1 σ of LA-ICP-MS transient signal noise and counting statistical errors.

Doubly charged ^{138}Ba produced a significant interference effect on ^{69}Ga (Fig. 11), which resulted in Ga-Ba correlation close to 1 in KUI-3 (the most Ba-rich sample in this study). Although the barium isotope analyzed in this study was ^{137}Ba, it is not the most abundant barium isotope encountered in normal terrestrial materials (Berglund & Wieser 2011). The most abundant barium isotope is ^{138}Ba (71.70 %), followed by ^{137}Ba (11.23 %). Since $^{138}Ba^{++}$ is identical to $^{69}Ga^{+}$ in terms of mass/charge, an interference is introduced especially in Ba-rich minerals. Although the Ga-Ba interference was identified after

analysis, and as such no robust offline corrections could be made to the sample data, an empirical correction was applied to all biotite Ga data points with the underlying assumption that KUI-3 contains no Ga (i.e. the apparent Ga abundances in KUI-3 are wholly caused by doubly charged Ba). A linear function was then fit to the Ga-Ba ppm data in KUI-3, and the resulting slope and intercept were used in calculating "corrected" Ga abundances for all remaining samples. However, it is stressed that not only does this empirical correction introduce statistical uncertainties in itself, there is no independent way of verifying the double charge formation rate of Ba, and thus there are potential large uncertainties associated with the biotite Ga data in this study. Ga and Ba in amphiboles and muscovites, on the other hand, did not produce any noticeable linear correlations, and are assumed to be relatively unaffected by the Ba interference.

Fractionation factors were calculated with in-house software that is based on Fryer et al. (1995). Fractionation factor analysis is an indicator of data reliability as it is a measure of how parallel an isotope signal is to the internal standard. A fractionation factor of 1 for a given element indicates that the ablation signal was stable throughout the integration interval. A fractionation factor much higher or lower than 1 indicates that the analyte could be chemically zoned, contained an inclusion, or that the element was close to the limit of detection. Since a multitude of trace element concentrations vary over several orders of magnitude between samples, a deviation of 20 % from the integrated signal time is considered acceptable in this study. A 20 % deviation translates into an equivalent concentration anomaly, which is less than the sample abundance variation in most cases, and hence does not skew deductions to a great extent (Fryer et al. 1995, Ranta 2017).

Six representative external standard measurements and 16 sample grain measurements were selected for fractionation factor analysis. External standards were selected using a random number generator from a total of 24 standard measurements. Representative sample grains were selected by sorting each sample from largest to smallest according to their Al wt.% content. The middle value grain was picked as a representation of the typical Al wt.% content in the sample. If the number of grains measured was even (within a sample), the middle value was chosen randomly between the two middle values. Since concentration calculations depend on internal standard abundances, Al concentration was selected as the eliminating factor. Moreover, this representation scheme is used for all EPMA and LA-ICP-MS result portrayal hereafter, unless stated otherwise. Fractionation

factors are shown for the selected standards, micas, and amphiboles in Appendix 4.

Fractionation factors (hereafter FF) are within acceptable limits in the selected GSE-1G external standards (Appendix 4, Fig. 3). All elements range from 0.87 to 1.07. The lowest and highest values are associated with Cd and Sn-corrected ^{115}In. Minor troughs are associated with Sc, Zn, and Cd, while ^{115}In FFs appear elevated relative to their neighboring elements.

For the selected micas (biotite & muscovite), major element FFs are within acceptable limits except for Ca, which forms a uniform peak (Appendix 4). However, the relatively high Ca FFs are caused by low signal to background ratios (e.g. Fig. 12). Trace elements show more complex behavior: Be, B, Cu, Zr, Cd, In, REEs, and Hf display large scale scattering. However, this results mainly from patchy ablation signals or because the signal to background ratios are close to 1. Nonetheless, if these general observations hold true for all mica measurements, the accuracies of the previously mentioned trace elements are somewhat questionable, especially for REEs. Thus, with respect to Be, B, Cu, Zr, Cd, In, REEs, and Hf, the reported concentrations are in many cases more informational rather than absolute. That is, an element was detected, but its accuracy might be low.

Based on the amphibole fractionation factor results (Appendix 4, Fig. 2), all elements are more or less within the acceptable range apart from B. The relatively high FFs for B are, again, caused by low signal to background ratios (Fig. 12).

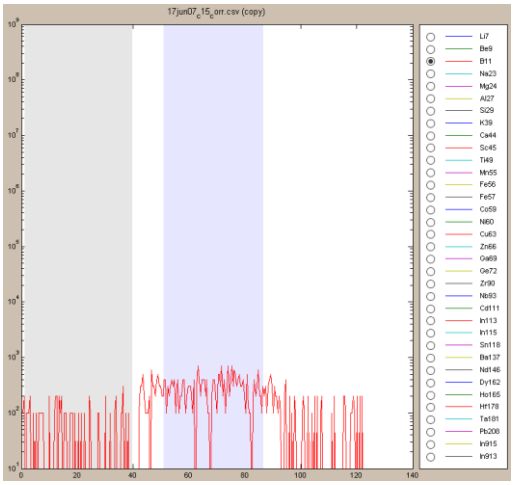

Figure 12. The boron LA-ICP-MS signal (red line) of a LOV-1 amphibole grain analysis as an example of a low signal to background ratio. The light-blue area represents the signal, and grey and white areas represent the background.

4. RESULTS

4.1. Sample petrography

All arbitrary adjectives in this sub-chapter are relative in the context of this sub-chapter, i.e. “highly”, “fairly”, etc. are referenced to the other samples in this study. Opaque minerals were determined by SEM-EDS analysis and are reported, when applicable, in parentheses.

4.1.1. A-type granites

The main rock-forming minerals in A-type granites (LOV-1 to -6) comprise microperthitic orthoclase + saussuritic plagioclase + undulose quartz + biotite ± hornblende. Accessory phases include opaque minerals (mainly ilmenite, but sulfides such as pyrite and sphalerite were encountered) + apatite + zircon + fluorite + chlorite ± hornblende ± muscovite ± iddingsite ± epidote ± fayalite ± calcite ± anatase ± allanite ± monazite ± hematite. Hornblende occurs as a main rock-forming mineral in samples LOV-2, -5, and -6, and these samples, in addition to LOV-1, host orthoclase and plagioclase megacrysts. Thus, LOV-1, -2, -5, and -6 are porphyritic, whereas LOV-3 and -4 are equigranular.

LOV-1 and LOV-2 exhibit typical porphyritic wiborgite rapakivi texture with orthoclase ovoids enclosed by plagioclase overgrowths. The orthoclase ovoids are up to 2.5 cm in size (in thin section; up to c. 4 cm in hand specimen) while the groundmass consists of ca. 0.5 cm mineral grains. Plagioclase is often saussuritizated, and orthoclase shows some intermittent signs of sericitization. Myrmekitization is also evident, but not common or pervasive (Fig. 13 B). Chloritization and biotitization of biotite and hornblende are common, and mafic minerals often appear shredded. Biotite ± hornblende occur commonly in the interstices of felsic minerals, although quartz appears to invade mafic minerals at times (Fig. 13 A). The K-feldspar ovoids host numerous mafic minerals as inclusions.

Grain size in LOV-3 and LOV-4 varies typically between 1 and 5 mm, and mafic minerals

are commonly slightly smaller than the felsic minerals. Felsic phases and biotites are relatively unaltered compared to the porphyritic A-type granites, however chloritization in some biotite grains is evident. The average grain size in LOV-4 is slightly smaller compared to LOV-3. Grainy deep blood red accumulations, approximately 0.5 mm in diameter, and interpreted as hematite, occur in LOV-4 as an added minor mafic phase.

LOV-5 and LOV-6 are porphyritic rapakivi granites that host up to 4 cm (in hand specimen) orthoclase and plagioclase megacrysts. Orthoclase megacrysts are generally larger than the plagioclase megacrysts, up to 2 cm and 1.5 cm, respectively (in thin section). Myrmekitic alteration textures are common along the orthoclase – plagioclase grain boundaries (Fig. 13 C), and plagioclase is often highly saussuritizated in LOV-5, but relatively unaltered in LOV-6. Orthoclase grains show some weak and occasional signs of sericitic alteration. In terms of myrmekite alteration, LOV-6 is the most evolved study sample. Quartz grains are commonly granular and 1 – 4 mm-sized, and occur in many occasions as a myrmekite alteration product in LOV-5. In LOV-6, quartz occurs chiefly as a granular or vermiform myrmekite alteration product, however there are several ca. 1 mm independent granular quartz grains. The main mafic phases, hornblende and biotite, are generally highly altered. Biotitization is common in hornblende, and chloritization in biotite. Unaltered hornblende and biotite occur mainly in quartz interstices, whereas the shredded and altered mineral grains are concentrated in orthoclase – plagioclase boundaries where myrmekite alteration is prevalent. Few hornblende grains are mantled by allanite in LOV-6 (Fig. 13 D). Owing to the apparent wiborgite texture and high modal plagioclase contentration (ca. 40 %), LOV-6 is classified as a dark wiborgite. However, the rapakivi ovoid textures are scarce in LOV-6 compared to LOV-1 and -2.

4.1.2. S-type granites

The main rock-forming minerals in S-type granites (OLR09 and NAR-1) compose of microcline + undulose quartz + slightly sericitic plagioclase + biotite + muscovite. Accessory phases consist of fluorite (Fig. 13 E) + zircon + apatite ± opaque minerals (ilmenite, pyrite) ± garnet ± tourmaline ± anatase and ± monazite. Both samples are medium-grained and equigranular.

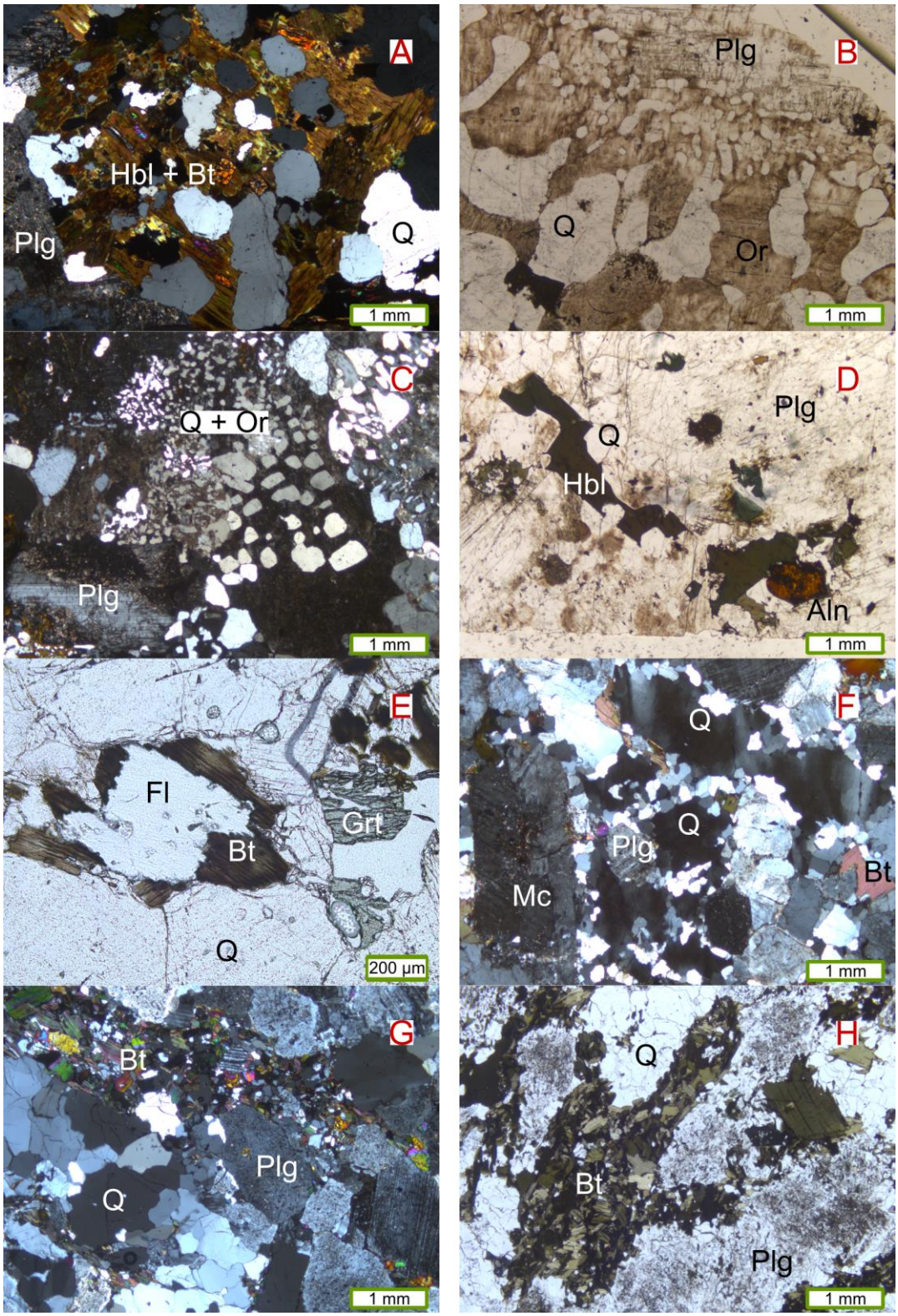

Figure 13. Cross- and plane-polarized thin section photographs. (A) Shredded biotite and hornblende in LOV-1. (B) Incipient myrmekite in LOV-2. (C) Comparably more developed myrmekite texture in LOV-5. (D) Allanite, hornblende and quartz encased by a plagioclase megacryst in LOV-6. (E) A large fluorite crystal surrounded by biotite in NAR-1. (F) Polygonised and undulose quartz in OLR09. (G) Cumulophyric biotite and polygonised quartz in VIG-1. (H) Cumulophyric and “independent” biotite in KUI-3. Aln = allanite; Bt = biotite; Fl = fluorite; Grt = garnet; Hbl = hornblende; Mc = microcline; Or = orthoclase; Plg = plagioclase; Q = quartz.

All major phases are up to ca. 3 mm-sized in OLR09, although the two micas occur chiefly as ≤ 0.5 mm grains. Microcline is typically slightly sericitic, whereas plagioclase is often fairly sericitic and occasionally exhibits incipient myrmekite alteration. The larger quartz grains typically exhibit undulose extinction that resembles polygonised quartz, and in many cases the larger undulose quartz grains are enveloped by the smaller fully polygonised quartz grains (Fig. 13 F). Biotite and muscovite grains are slightly folded and exhibit undulose extinction in some instances.

The felsic phases are typically 1 – 5 mm-sized in NAR-1, whereas muscovite and biotite are up to 2.5 mm-sized. Out of the two micas, muscovite is more abundant. Both felsic and mica phases are relatively unaltered, however plagioclase shows faint, grainy sericitization in some grains. The two micas are weakly oriented in the same general direction, but there are numerous instances where individual mica grains differ in orientation from the general foliation direction.

4.1.3. I-type granites

The main rock-forming minerals in I-type granites (VIG-1 and KUI-3) include highly saussuritic plagioclase + polygonised and undulose quartz + biotite ± microcline ± epidote, whereas the accessory phases consist of fluorite + muscovite + apatite + zircon ± chlorite ± epidote ± sphene ± tourmaline and ± calcite. Both samples are medium-grained, equigranular, and weakly foliated. VIG-1 is classified as granodiorite and KUI-3 as tonalite.

Plagioclase and quartz grains are up to 3 mm-sized in VIG-1, whereas microcline grains are typically ≤ 0.5 mm. Plagioclase grains are highly saussuritized and speckled by epidote and muscovite, whereas the microcline grains are unaltered. Both plagioclase and quartz are cross-cut by intermittent epidote-filled fractures. Individual biotite and epidote grains are typically ≤ 0.5 mm-sized, however they occur simultaneously as elongated cumulophyric clusters (Fig. 13 G) that are up to 5 mm in lenght. Biotite shows occasional chloritization, however this is limited to a handful of individual grains.

KUI-3 is akin to VIG-1 in overall texture and grain size distribution: plagioclase is highly

saussuritic, quartz is typically polygonised and biotite occurs as cumulophyric aggregates (Fig. 13 H), although epidote is an accessory phase in KUI-3. Plagioclase and quartz are up to 3 mm-sized and biotite grains are typically ≤ 0.5 mm-sized. There are, however, multiple large, up to 2.5 mm, biotite grains that are absent in VIG-1. Biotite is relatively fresh in KUI-3, and shows few, if any, signs of alteration, although some grains are slightly bent and exhibit undulose extinction.

In summary, all samples, based on textural and mineral criteria, show some signs of biotite alteration, with (in a somewhat arbitrary decreasing order) LOV-6 and LOV-5 being the most altered samples, followed by LOV-2, LOV-1, LOV-3, LOV-4, VIG-1, OLR09, NAR-1 and KUI-3. All rapakivi samples contain orthoclase that has been subjected to perthitic exsolution, while all other samples, barring KUI-3, contain fresh microcline. Quartz exhibits undulose extinction in all samples and alteration products are exhibited in other felsic phases. Samples OLR09, VIG-1 and KUI-3 contain polygonised quartz. Sample rock types were identified (Fig. 14) after the IUGS classification (Streckeisen 1974).

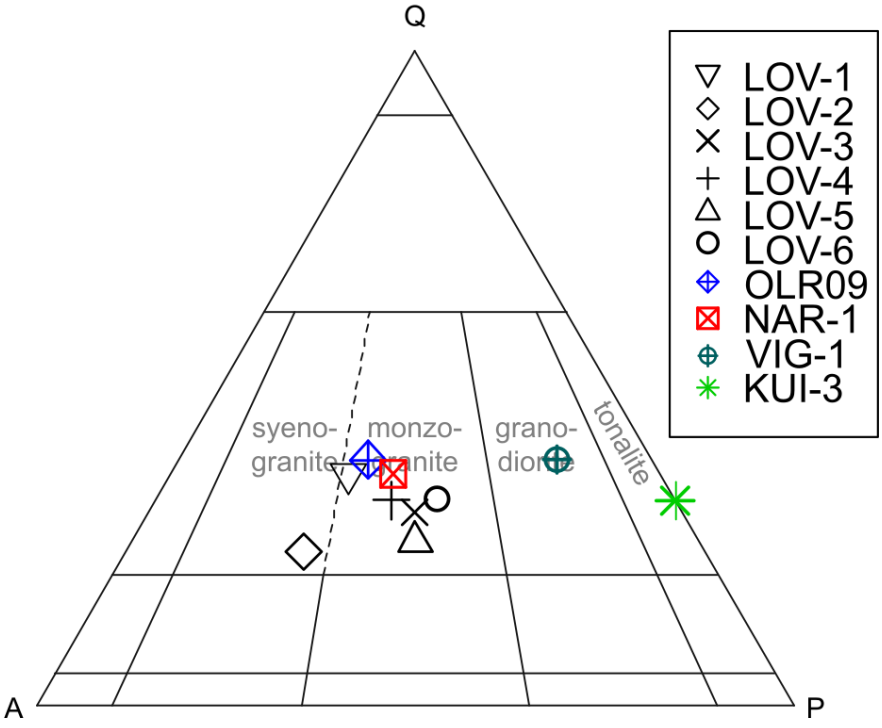

Figure 14. Sample identification after the IUGS classification (Streckeisen 1974).

4.2. Bulk chemical analysis (XRF)

Data from the “fine” and “coarse” analysis fractions discussed in Chapter 3.1 deviate less than 1% with respect to their total weight percentages. However, individual oxide and trace elements analyses deviate up to about 320 % between the coarse and fine fractions. For example, the lowest and highest oxide element ratios (defined as the fine fraction wt.% divided by the coarse fraction wt.%) are 0.60 for P_2O_5 (LOV-5) and 2.00 for MnO (NAR-1), respectively. The most dramatic deviations occur in the <1 wt.% range. The lowest and highest trace element ratios are 0.50 for Ni (LOV-3) and 3.19 for Ce (LOV-3). Despite this, the absolute concentration deviations are relatively low (e.g. 0.04 wt.% MnO vs. 0.02 wt.% MnO in NAR-1), and geochemical discrimination plots produce similar results both with the “fine” and “coarse” fraction data. Nonetheless, the “fine” fraction was selected as a better estimate of the average bulk composition, as discussed in Chapter 3.1. Hence, all reported bulk concentrations and associated calculations hereafter reflect the “fine” fraction results. Data from whole-rock analyses are reported in Table 6. The “coarse” fraction results are reported in Appendix 6.

Bulk major element Harker diagrams data are plotted in Fig. 15. As a crude approximation, and on the basis of SiO_2 content , KUI-3 is the most primitive sample, followed by LOV-6, LOV-2, LOV-5, VIG-1, LOV-1, OLR09, LOV-4, LOV-3, and finally NAR-1. Thus, NAR-1 is the most evolved sample. TiO_2, Al_2O_3, FeO, MnO, CaO, and P_2O_5 contents generally decrease with progressing SiO_2 evolution. Trends for MgO, Na_2O, and K_2O are more scattered, but KUI-3 and VIG-1 form distinct outliers (with regard to Na_2O and K_2O), reflecting that they contain less potassium feldspar and more plagioclase compared to the other granitoids.

Table 6. Sample whole-rock compositions as determined by WD-XRF. Oxide element and total rows are expressed as wt.%, and trace element rows as ppm. All iron is assumed to be ferrous. Table continued on the next page.

	LOV-1	LOV-2	LOV-3	LOV-4	LOV-5	LOV-6	OLR09	NAR-1	VIG-1	KUI-3
SiO_2	70.18	68.47	75.18	73.28	69.64	66.55	71.41	75.99	70.12	63.17
TiO_2	0.32	0.43	0.15	0.25	0.45	0.50	0.26	0.06	0.25	0.44
Al_2O_3	13.76	14.07	11.50	12.25	13.06	15.02	14.37	13.27	14.68	15.82
FeO	2.70	3.50	1.58	2.23	4.27	4.22	1.64	0.70	1.87	4.90
MnO	0.04	0.04	0.02	0.03	0.06	0.05	0.02	0.04	0.04	0.07
MgO	0.26	0.30	0.08	0.21	0.38	0.30	0.65	0.13	0.81	2.11
CaO	1.48	1.82	0.68	0.63	2.10	3.06	1.36	0.66	2.53	3.12
Na_2O	2.91	2.91	2.43	2.54	2.38	2.99	2.76	3.61	4.80	4.61
K_2O	5.78	5.98	6.05	5.83	5.35	4.99	5.07	4.13	2.54	2.34
P_2O_5	0.07	0.10	0.02	0.06	0.09	0.12	0.07	0.08	0.08	0.13
Sub-total	97.50	97.62	97.69	97.31	97.78	97.80	97.61	98.67	97.72	96.71
V	6	8	b.d.	8	8	b.d.	26	7	33	84
Cr	b.d.	b.d.	b.d.	b.d.	b.d.	b.d.	b.d.	b.d.	15	76
Ni	b.d.	2	2	2	2	2	5	b.d.	9	28
Cu	11	6	b.d.	b.d.	13	6	4	b.d.	8	5
Zn	87	87	59	60	147	112	24	22	36	71
Rb	245	247	393	388	266	234	168	253	56	88
Sr	152	152	37	56	164	231	507	65	594	662
Y	45	59	95	68	97	70	12	12	7	10
Zr	282	436	254	239	464	470	123	36	73	95
Nb	21	21	28	26	28	25	9	15	8	9
Ba	1127	1105	233	324	792	1091	829	196	760	496
La	98	81	166	111	151	112	43	b.d.	21	34
Ce	162	144	287	193	268	198	81	b.d.	39	48
U	9	9	11	17	6	7	5	13	2	2
Total	97.71	97.86	97.85	97.46	98.02	98.06	97.79	98.74	97.89	96.89
Type	A	A	A	A	A	A	S	S	I	I
A/CNK	1.00	0.97	0.98	1.05	0.97	0.95	1.15	1.14	0.96	1.00
Fe* *	0.91	0.92	0.95	0.91	0.92	0.93	0.72	0.84	0.70	0.70
MALI*	7.21	7.07	7.80	7.74	5.63	4.92	6.47	7.08	4.81	3.83
ASI*	1.01	0.97	0.98	1.06	0.97	0.95	1.16	1.15	0.97	1.01

Type = S-I-A-M classification of granitoids after Whalen et al. (1987) and Chappell & White (2001); b.d. = below detection limit; * = after Frost et al. (2001); Fe* = $FeO_{tot}/(FeO_{tot}$ + MgO); MALI = Modified alkali-lime index; ASI = Aluminum saturation index (corrected for apatite).

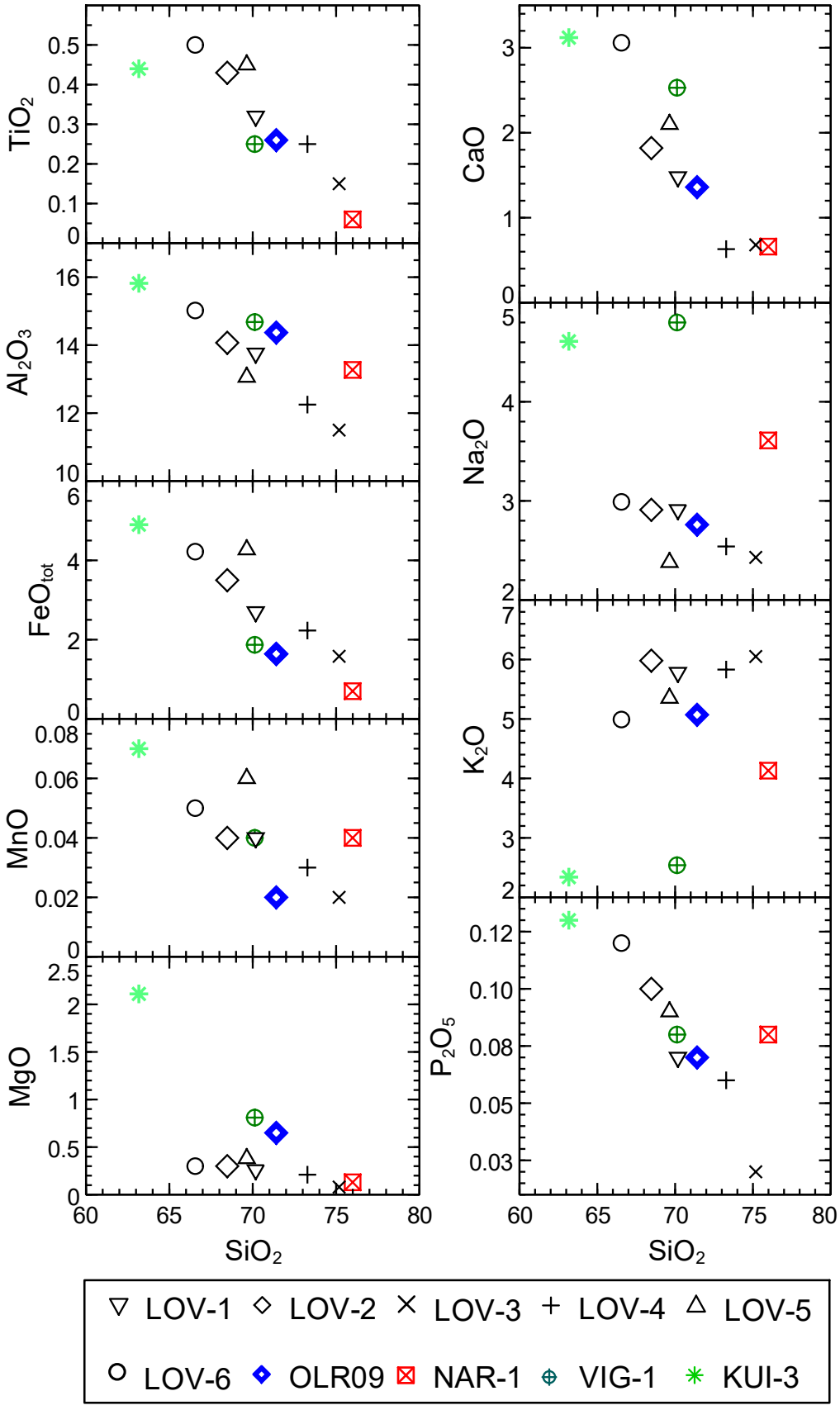

Figure 15. Whole-rock Harker diagrams (in wt.%).

Based on the S-I-A-M classification of granites (Whalen et al. 1987, Chappell & White 2001), samples LOV-1 to LOV-6 are A-type granites, OLR09 and NAR-1 are S-type granites, and VIG-1 and KUI-3 are I-type granites (Fig. 16). Simple major element discrimination between A- and S+I-types show no clear differences: according to Whalen et al. (1987), A-type granites should exhibit higher abundances of SiO_2, Fe, and K+Na, and lower abundances of Al, Mg, and Ca. The internal variation within A-type granites is in most cases higher than the variation between A- and S+I-types. SiO_2, particularly, is relatively low (66.55 – 70.18 wt.%) in all LOV-samples except LOV-3 and LOV-4. However, based on the mean composition of the aforementioned major cations, the requirements are met, but often just barely. Nonetheless, based on trace element compositions, clear differences begin to emerge. A-type granites should, in theory, contain higher abundances of Zn, Y, Nb, Zr, and REE, and lower abundances of V, and in this case the requirements are fulfilled (Whalen et al. 1987). Therefore, the LOV-samples are classified as A-type granites.

According to the criteria of Chappell & White (2001), and based on the previous trace element discrimination scheme, OLR09 and NAR-1 are classified as S-type granites, and VIG-1 and KUI-3 as I-type granites. In addition to characteristic mineralogy (e.g. muscovite and garnet in S-type granites, sphene in I-types), the SiO_2 contents in OLR09 and NAR-1 are high, A/CNK > 1.1, CIPW normative corundum > 1% (Appendix 5), CaO and Sr contents are lower (although for Sr in OLR09 only marginally), and K_2O and Rb contents are higher compared to VIG-1 and KUI-3. Although VIG-1 is relatively high in SiO_2 (70.12 wt.%), all other criteria indicate that both VIG-1 and KUI-3 are I-type granites, as A/CNK < 1.1, CIPW normative corundum < 1%, etc. VIG-1 and KUI-3 are effectively mirror images of OLR09 and NAR-1 in terms of the discriminating criteria by Chappell & White (2001).

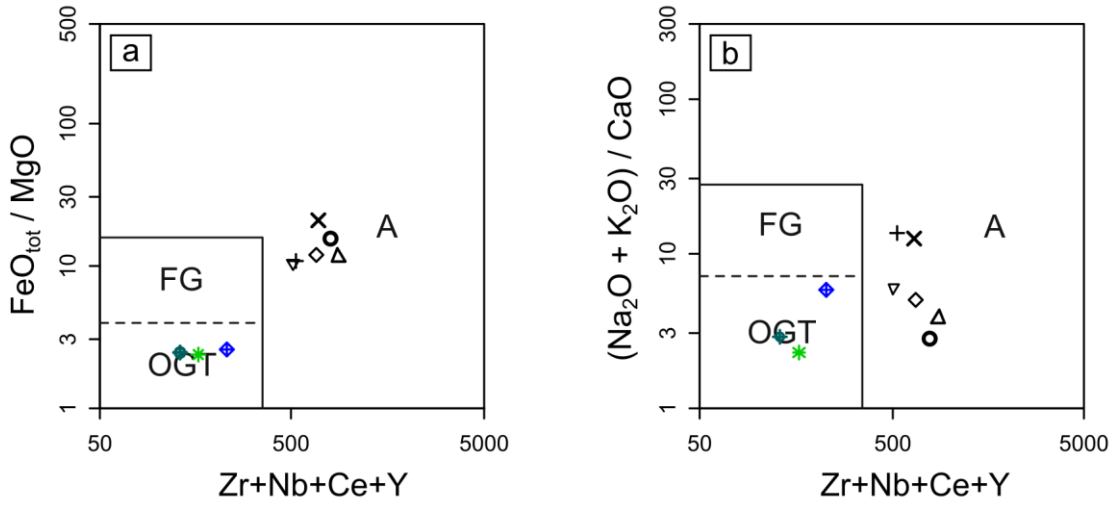

Figure 16. Geochemical discrimination diagrams of Whalen et al. (1987). (a) Zr+Nb+Ce+Y vs. FeO_{tot} / MgO, (b) Zr+Nb+Ce+Y vs. (Na_2O + K_2O) / CaO. Symbology as in Figs. 12 and 13. A = A-type granites; FG = fractionated felsic granites; OGT = unfractionated M-, I-, and S-type granites. NAR-1 is omitted from both plots due to lack of Ce.

Sample whole-rock chemistry was further assessed after the trace- and major element classifications of Pearce et al. (1984) and Frost et al. (2001). Although the two respective classifications do not delve into the alphabet classification of granitoids *sensu stricto*, they do share common characteristics with the S-I-A-M classification. I-type granitoids tend to plot in the volcanic arc (VAG) field in Pearce trace element diagrams, whereas S- and A-type granitoids tend to plot in the collision- (syn-COLG) and within plate granite (WPG) fields, respectively (Pearce et al. 1984). All A-type study samples plot in the WPG field, and I- and S-type samples in the VAG or syn-COLG fields, as is expected (Fig. 17).

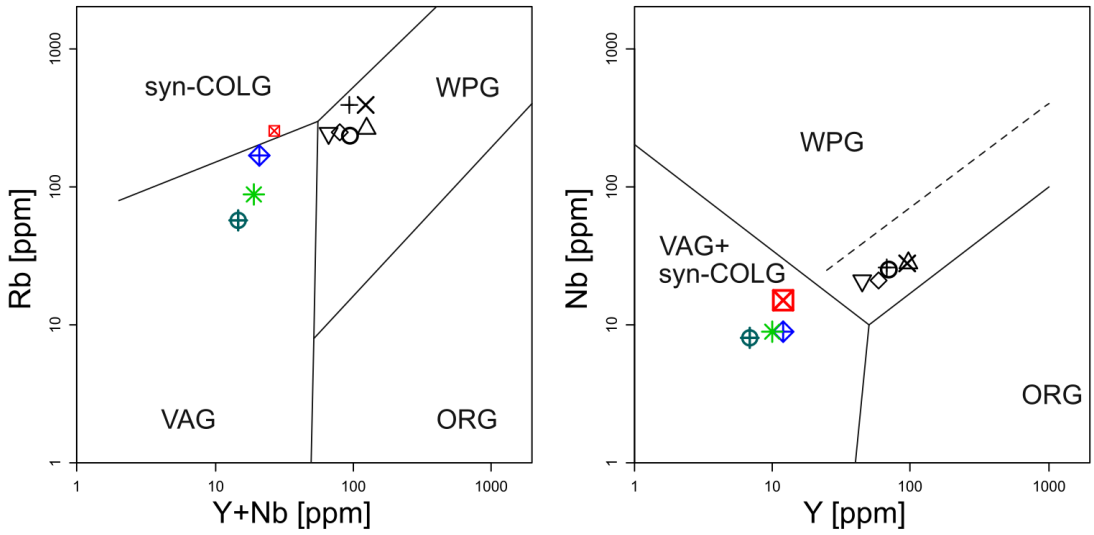

Figure 17. Tectonic discrimination diagrams after Pearce et al. (1984). Scales are logarithmic, and symbology as in Figs. 12, 13, and 14. syn-COLG = syn-Collision Granites; ORG = Ocean Ridge Granites; VAG = Volcanic Arc Granites; WPG = Within Plate Granites.

According to Frost et al. (2001), A-type granites are predominantly ferroan and alkali-calcic (LOV-1, LOV-2, LOV-3, LOV-4, LOV-6), but there are some ferroan calc-alkalic suites (LOV-5). Most A-type granites are metaluminous (LOV-2, LOV-3, LOV-5, LOV-6), but A-type granites may also be peraluminous (LOV-1, LOV-4). I-type granites are mostly magnesian and calc-alkalic (VIG-1) or calcic, but, again, there are some alkali-calcic (KUI-3) suites, as well. I-type granites may be metaluminous (VIG-1) or peraluminous (KUI-3), however they are predominantly metaluminous. S-type granites are peraluminous by definition (OLRO9, NAR-1), either magnesian (OLR09) or ferroan (NAR-1), and span from calcic to alkalic (OLR09 and NAR-1 are both calc-alkalic). Results for the Frost et al. (2001) classification are plotted in Fig. 18 and summarized in Table 7.

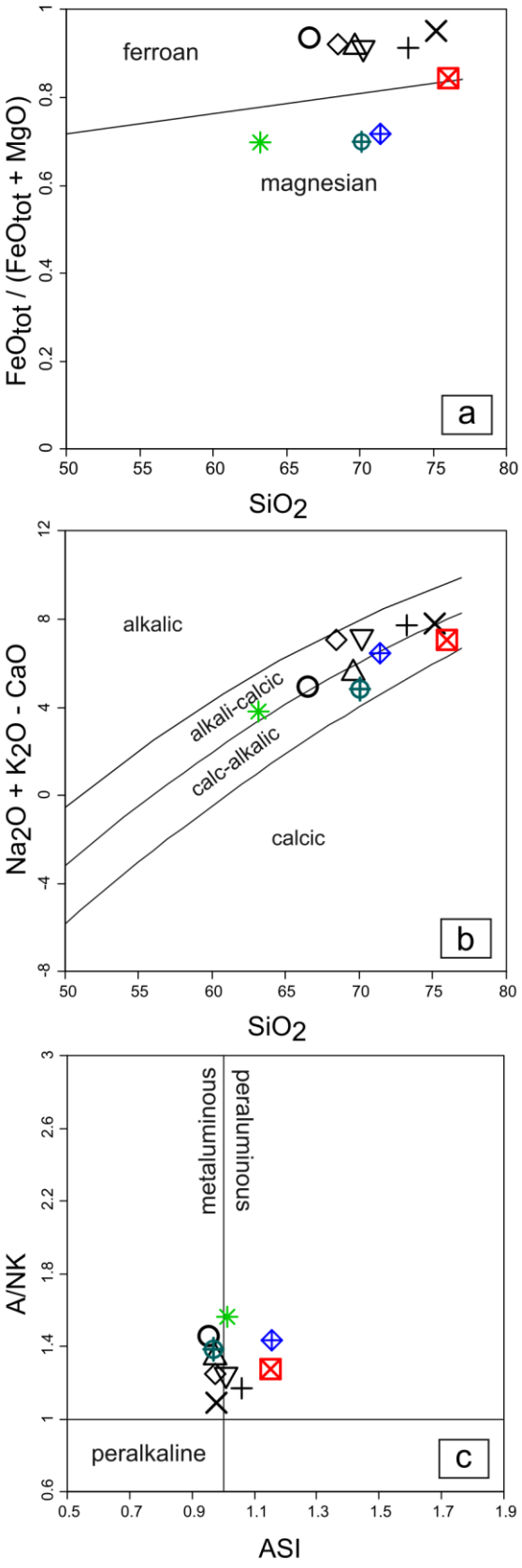

Figure 18. Samples plotted according to the classification of Frost et al. (2001). (a) Fe* vs. SiO_2, (b) MALI vs. SiO_2, (c) molecular Al_2O_3/Na_2O+K_2O vs. ASI. Symbology as in Figs 12, 13, 14, and 15.

Table 7. Sample classification after Frost et al. (2001) summarized.

Sample	Fe/Mg	MALI	ASI
LOV-1	ferroan	alkali-calcic	peraluminous
LOV-2	ferroan	alkali-calcic	metaluminous
LOV-3	ferroan	alkali-calcic	metaluminous
LOV-4	ferroan	alkali-calcic	peraluminous
LOV-5	ferroan	calc-alkalic	metaluminous
LOV-6	ferroan	alkali-calcic	metaluminous
OLR09	magnesian	calc-alkalic	peraluminous
NAR-1	ferroan	calc-alkalic	peraluminous
VIG-1	magnesian	calc-alkalic	metaluminous
KUI-3	magnesian	alkali-calcic	peraluminous

K/Rb and Ba/Rb were used as whole-rock fractionation indicators (Fig. 19). As groups, I-type granites are the least evolved, S-type granites are intermediate, and A-type granites are the most fractionated samples. However, VIG-1 is the least fractionated individual sample, and LOV-3, -4, and NAR-1 appear to be most fractionated individual samples. Thus, it is not definitive that all S-type granites are less fractionated than all A-type granites.

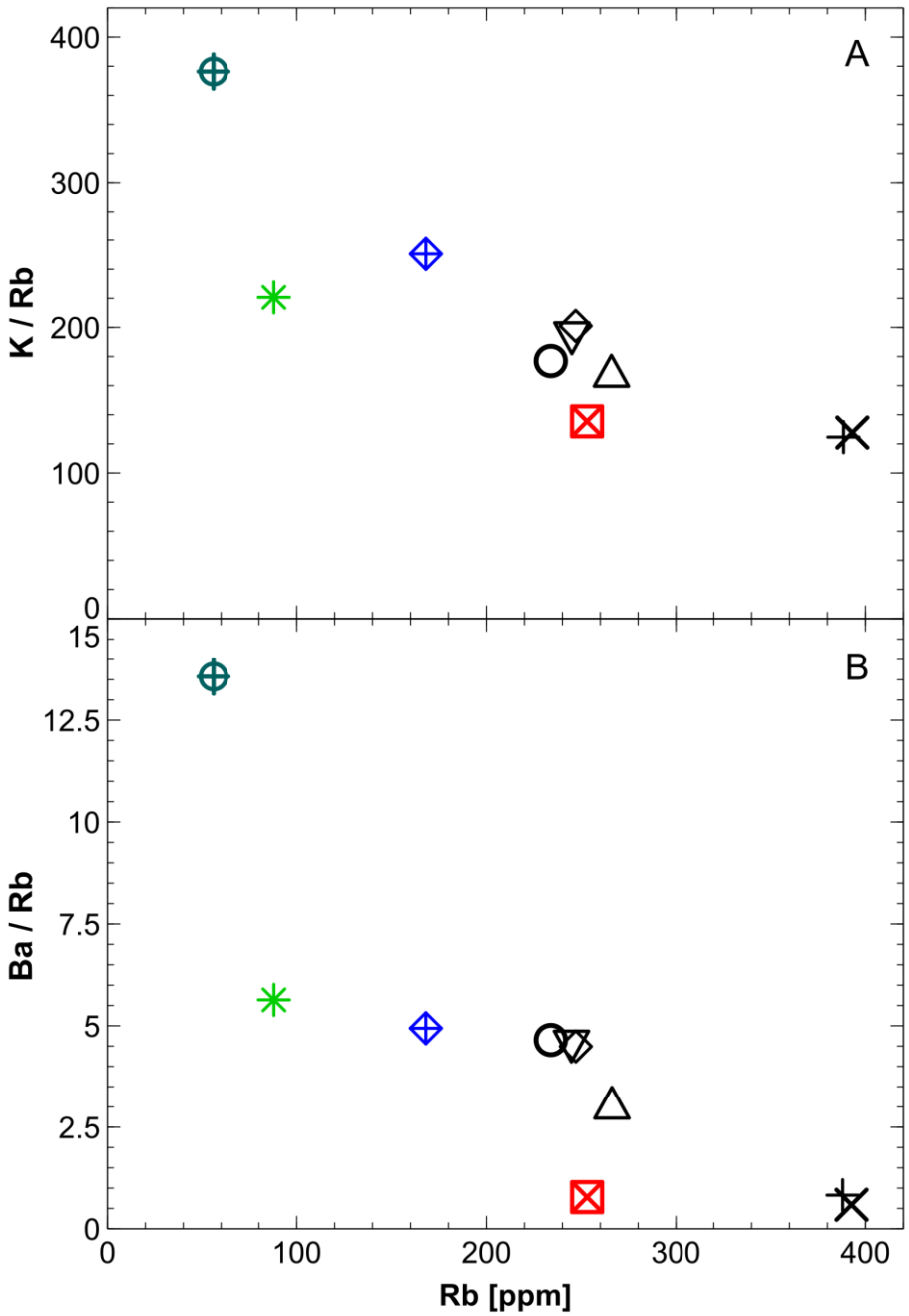

Figure 19. (A) K/Rb and (B) Ba/Rb ratios as whole-rock fractionation indicators. Symbology as in the previous figures in this sub-chapter.

4.3. *In situ* major element results (EPMA)

Biotite major element data for the selected representative samples (i.e. representative mineral grains) are reported in Table 8. The respective major element data for all

measured biotite grains are reported in Appendix 7.

All samples are within similar range with respect to Si, Ca, Na, and K (apfu). In terms of total Al, the less fractionated A-type samples (LOV-1, -2, -5, -6) are relatively depleted, I-type samples, OLR09, LOV-3 and -4 are intermediate, and NAR-1 is enriched. In terms of tetrahedral aluminum, however, all granite types are within 2.2 – 2.6 ^{IV}Al apfu, although S-type biotites are slightly more abundant than I-type biotites. A-type biotites are somewhat enriched in Ti (although A-type biotite concentrations span across the whole Ti apfu content range), S-type biotites are intermediate, and I-type biotites contain the lowest Ti concentrations. The clearest differences are exhibited in the Fe and Mg contents: A-type biotites and NAR-1 are Fe-rich, while OLR09 and I-type biotites are Fe-poor and thus contain more Mg.

The IMA nomenclature of micas (Rieder et al. 1998) recommends using end-member names in classifying micas. However, since the study samples do not exhibit ideal end-member behavior, an approximate classification based on the iron and tetrahedral aluminum content was used (Fig. 20). A-type biotites are iron-rich and identified as annitic: the Fe / Fe + Mg (apfu) varies from 0.79 to 0.97, while ^{IV}Al content varies from 2.22 to 2.50. In terms of iron-enrichment, the S-type biotites are more diverse. NAR-1 is comparable to the lower end of A-type biotites with a Fe / (Fe + Mg) ratio of 0.80 (i.e. annitic), while OLR09 is more phlogopitic with Fe / (Fe + Mg) ranging from 0.56 to 0.58. ^{IV}Al in S-type biotites varies from 2.40 to 2.54. I-type biotites are even more iron-depleted and phlogopitic: Fe / (Fe + Mg) ranges between 0.39 to 0.55 with VIG-1 being the most magnesian of all samples while the ^{IV}Al in I-type biotites varies from 2.23 to 2.39.

According to the *mgli* classification of Tischendorf et al. (1997, 2001), A-type biotites were identified mainly as annite and S-type biotites either as Mg biotite (OLR09) or Fe biotite/siderophyllite (overlapping criteria for NAR-1). All I-type biotites were identified as Mg biotite. Thus, in broad terms, the *mgli* classification supports the iron vs. tetrahedral aluminum classification: A-type biotites are, indeed, annite and Fe biotite/siderophyllite (NAR-1) can be identified as (magnesian) siderophyllite, and Mg biotites as ferroan phlogopite (Rieder et al. 1998, Tischendorf et al. 2001).

The dioctahedral mica grains measured from S-type granites (NAR-1) are classified as

muscovite according to both the mica recommendations of the IMA and Tischendorf et al. (1997). Major element oxide data is presented for the representative sample in Table 9, and all data points are reported in Appendix 8.

The amphibole grains measured from A-type granites (LOV-1, LOV-2.1, and LOV-2.2) are identified as hastingsite according to the recommendations of the IMA (Hawthorne et al. 2012). Major element oxide data for the representative samples are reported in Table 10, and all data points are disclosed in Appendix 9.

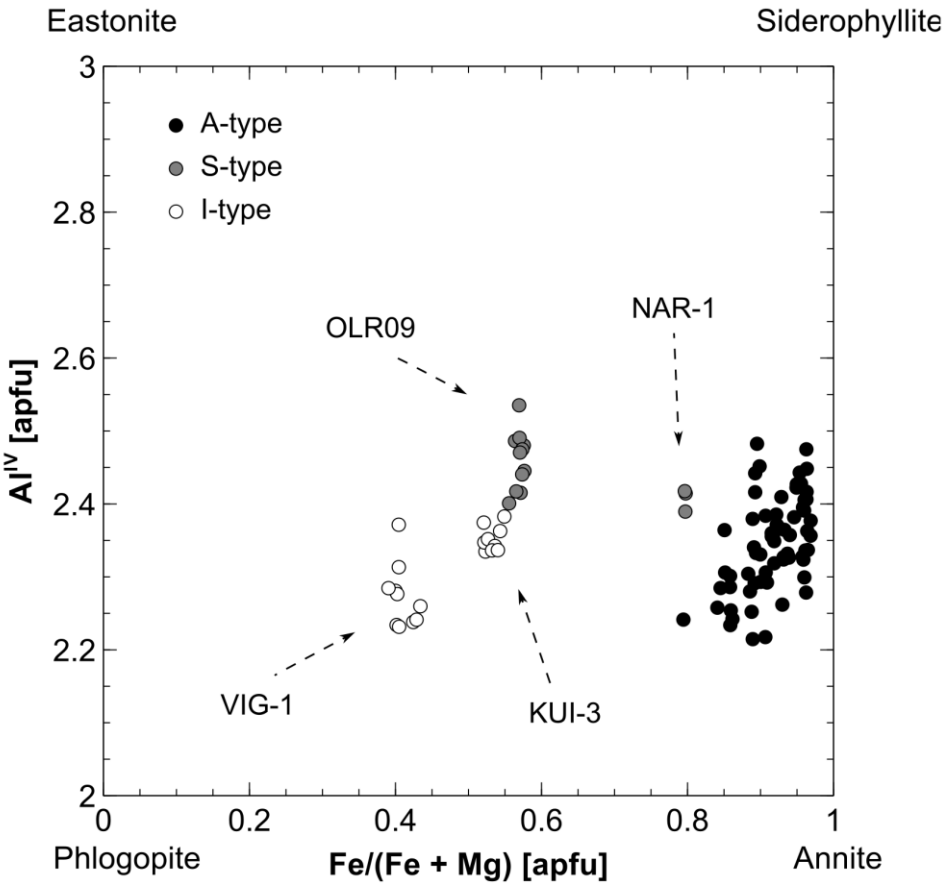

Figure 20. Classification of biotites based on Fe / (Fe + Mg) vs. tetrahedral aluminum.

Table 8. Major element composition of representative biotite analyses (in wt.%) determined by EPMA. Cations calculated on the basis of 22 oxygens.

	A-type								S-type		I-type	
	LOV-1	LOV-2.1	LOV-2.2	LOV-3	LOV-4	LOV-5	LOV-6.1	LOV-6.2	OLR09	NAR-1	VIG-1	KUI-3
	grain 8	grain 1	grain 10	grain 3	grain 10	grain 5	grain 4	grain 7	grain 11	grain 9	grain 8	grain 5
SiO_2	34.68	34.62	34.82	34.77	35.05	33.30	32.88	33.89	35.87	34.34	37.33	36.13
TiO_2	2.39	3.90	3.48	2.75	2.26	3.04	3.36	2.61	2.42	1.47	1.15	1.86
Al_2O_3	12.24	11.80	11.93	14.36	15.25	12.27	12.50	12.53	16.25	17.11	15.38	15.88
FeO	33.07	33.99	33.19	35.15	32.08	34.68	37.08	36.86	22.02	26.63	16.00	19.97
MgO	3.51	2.31	3.08	0.79	2.20	1.76	0.79	1.70	9.19	3.81	13.19	10.07
CaO	b.d.	b.d.	b.d.	b.d.	b.d.	b.d.	b.d.	b.d.	b.d.	b.d.	b.d.	b.d.
Na_2O	b.d.	b.d.	0.12	b.d.	0.11	b.d.	b.d.	b.d.	b.d.	b.d.	b.d.	b.d.
K_2O	8.44	8.98	8.83	8.47	8.74	8.37	8.12	8.13	9.00	8.74	9.03	9.21
Li_2O †	0.10	0.14	0.14	0.28	0.17	0.14	0.17	0.16	0.04	0.49	0.03	0.04
H_2O*	3.63	3.65	3.66	3.70	3.72	3.55	3.56	3.62	3.87	3.70	3.88	3.84
Total	98.05	99.38	99.24	100.27	99.59	97.11	98.46	99.49	98.65	96.28	95.98	97.02
Si	5.73	5.69	5.70	5.64	5.65	5.63	5.54	5.62	5.56	5.57	5.77	5.64
Al^{IV}	2.27	2.29	2.30	2.36	2.35	2.37	2.46	2.38	2.44	2.43	2.23	2.36
T-site total	8.00	7.98	8.00	8.00	8.00	8.00	8.00	8.00	8.00	8.00	8.00	8.00
Al^{VI}	0.12	0.00	0.00	0.39	0.54	0.08	0.02	0.07	0.52	0.84	0.57	0.57
Ti	0.30	0.48	0.43	0.34	0.27	0.39	0.43	0.32	0.28	0.18	0.13	0.22
Fe	4.57	4.67	4.55	4.77	4.32	4.90	5.22	5.11	2.85	3.61	2.07	2.61
Mg	0.87	0.57	0.75	0.19	0.53	0.44	0.20	0.42	2.12	0.92	3.04	2.35
Li †	0.06	0.09	0.09	0.19	0.11	0.09	0.11	0.11	0.02	0.32	0.02	0.03
M-site total	5.85	5.72	5.73	5.68	5.66	5.81	5.87	5.92	5.78	5.55	5.80	5.74
Ca	0.00	0.00	0.00	0.00	0.00	0.00	0.00	0.00	0.00	0.00	0.00	0.00
Na	0.00	0.00	0.04	0.00	0.03	0.00	0.00	0.00	0.00	0.00	0.00	0.00
K	1.78	1.88	1.85	1.75	1.80	1.80	1.74	1.72	1.78	1.81	1.78	1.84
I-site total	1.78	1.88	1.88	1.75	1.83	1.80	1.74	1.72	1.78	1.81	1.78	1.84
OH	4.00	4.00	4.00	4.00	4.00	4.00	4.00	4.00	4.00	4.00	4.00	4.00
Total	19.70	19.67	19.71	19.62	19.60	19.71	19.72	19.75	19.58	19.68	19.60	19.61
Al total	2.39	2.29	2.30	2.75	2.89	2.45	2.48	2.45	2.97	3.27	2.80	2.92
Fe/Fe+Mg	0.84	0.89	0.86	0.96	0.89	0.92	0.96	0.92	0.57	0.80	0.40	0.53
mgli ‡	0.80	0.47	0.66	0.01	0.42	0.35	0.08	0.31	2.10	0.60	3.01	2.32
feal ‡	4.75	5.15	4.97	4.72	4.05	5.21	5.63	5.37	2.61	2.95	1.63	2.26

b.d. = below detection limit at a 95% confidence level; * = calculated stoichiometrically; † = calculated from LA-ICP-MS analysis; ‡ = after Tischendorf et al. (1997).

Table 9. Major element composition of representative S-type muscovite from sample NAR-1 (in wt.%) determined by EPMA. Cations calculated on the basis of 22 oxygens.

S-type	
	NAR-1
	grain 2
SiO_2	45.37
TiO_2	b.d.
Al_2O_3	32.06
FeO	3.07
MgO	0.64
CaO	b.d.
Na_2O	0.37
K_2O	10.35
Li_2O †	0.15
H_2O*	4.31
Total	96.34
Si	6.31
Al^{IV}	1.69
T-site total	8.00
Al^{VI}	3.56
Ti	0.00
Fe	0.36
Mg	0.13
Li †	0.08
M-site total	4.05
Ca	0.00
Na	0.10
K	1.84
I-site total	1.94
OH	4.00
Total	18.07
Al total	5.25
Fe/Fe+Mg	0.73
mgli ‡	0.05
feal ‡	-3.21

b.d. = below detection limit at a 95% confidence level; * = calculated stoichiometrically; † = calculated from LA-ICP-MS analysis; ‡ = after Tischendorf et al. (1997).

Table 10. Major element composition of representative A-type amphiboles (in wt.%) determined by EPMA. Cations calculated on the basis of 24 oxygens. * = calculated.

	A-type		
	LOV-1	LOV-2.1	LOV-2.2
	grain 9	grain 8	grain 4
SiO_2	40.03	39.72	40.29
TiO_2	0.61	1.25	1.36
Al_2O_3	8.47	8.47	8.21
FeO	33.23	30.31	31.00
MgO	1.90	2.60	2.69
CaO	10.46	10.15	10.24
Na_2O	1.73	1.78	1.68
K_2O	1.44	1.55	1.48
Initial total	97.87	95.82	96.95
$Fe^{3+}/\Sigma Fe$*	0.15	0.06	0.11
FeO*	28.15	28.55	27.62
Fe_2O_3*	5.65	1.95	3.76
H_2O+*	1.85	1.86	1.87
Total	100.29	97.88	99.19
Si	6.46	6.53	6.53
Al	1.54	1.47	1.48
Ti	-	-	-
T-site total	8.00	8.00	8.00
Ti	0.07	0.15	0.17
Al	0.07	0.18	0.09
Fe^{3+}	0.69	0.24	0.46
Fe^{2+}	3.71	3.79	3.64
Mg	0.46	0.64	0.65
C-site total	5.00	5.00	5.00
Fe^{2+}	0.09	0.14	0.10
Mg	-	-	-
Ca	1.81	1.79	1.78
Na	0.10	0.08	0.12
B-site total	2.00	2.00	2.00
Ca	-	-	-
Na	0.44	0.49	0.41
K	0.30	0.33	0.31
A-site total	0.74	0.82	0.71
OH	2.00	2.00	2.00
Sum T+C+B+A	15.74	15.82	15.71
Subgroup	Ca	Ca	Ca

4.4. *In situ* trace element results (LA-ICP-MS)

4.4.1. Trace element concentrations

Representative trace element data from LA-ICP-MS measurments are reported in Table 11 for biotites, muscovites, and amphiboles. All mineral grain analyses are disclosed in Appendices 10, 11, and 12, respectively.

For the sake of brevity, ranges and differences between different granite types are discussed here only for critical and rare metals (Li, Be, B, Sc, Co, Ga, Ge, Nb, Cd, In, Sn, REEs, Hf). Zr and Ta are discussed in conjunction with Hf and Nb, respectively. Non-critical trace elements are reported in tables and plotted in figures, however.

Based on the LA-ICP-MS measurement data, biotites in A-type granites are – as a group - the most consistently Li-enriched. The highest Li contents are encountered in S-type granites (NAR-1; 2290 – 2380 ppm), but the lower end of the S-type group (OLR09; 131 – 167 ppm) are on par with the Li content in I-type granites, which is the least Li-enriched group in this study. Lithium in A-type biotites range from about 420 to 1330 ppm with LOV-3 and LOV-4 being the most enriched, followed by LOV-6, LOV-2, LOV-5, and LOV-1. In I-type biotites the Li-concent varies between about 152 and 226 ppm with KUI-3 exhibiting higher consistent abundances.

Biotite Be abundances are more peculiar: high relative abundances occur both in the least and most fractionated granites (VIG-1; NAR-1, LOV-3, LOV-4), and the more "intermediate" samples form a sort of pseudo-Be trough. This results in a horseshoe-shaped fractionation scatter plot (c.f. Fig. 22 B). Be contents vary from 0.3 to 7.2 ppm in A-type biotites, 0.1 – 2.2 ppm in S-type biotites, and 0.6 – 3.0 ppm in I-type biotites.

Highest B concentrations in biotites occur in A-type granites. S-type biotites are slightly depleted compared to I-type biotites, thus S-type samples could be inferred as the least B-enriched, but, overall, abundances are low regardless of granite type. B varies from 0.2 to 3.6 ppm in A-type biotites, 0.2 – 0.6 ppm in S-type biotites, and 0.3 – 0.8 ppm in I-type biotites.

Biotite scandium concentrations are somewhat enigmatic. The range of Sc concentrations is relatively large in all granite types: 1.9 – 74 ppm in A-type, 13 – 44 ppm in S-type, and 2.1 – 29 ppm in I-type granites. Highest concentrations occur in LOV-4 and LOV-3, but other less fractionated samples (OLR09, KUI-3) contain markedly high Sc abundances compared to other more fractionated samples.

Cobalt concentrations are lowest in A-type biotites, followed by S-type biotites (with OLR09 being the more Co-abundant S-type sample), and finally I-type biotites with the highest abundances. Abundances for Co range from about 9.0 to 35 ppm in A-type biotites, 16 – 58 ppm in S-type biotites, and 63 – 81 ppm in I-type biotites.

Gallium abundances are highly speculative as discussed in Chapter 3.5.2. Thus, Ga concentrations reported hereafter should be considered qualitative rather than quantitative. Nonetheless, it is indicated that Ga contents are highest in A-type biotites, followed by S-type biotites, and finally I-type biotites. Gallium ranges from about 7 to 64 ppm in A-type biotites, 6 – 42 ppm in S-type biotites, and 6 – 15 ppm in I-type biotites (it is assumed that KUI-3 does not contain Ga).

Ge abundances are are relatively low, but elevated in A-type biotites, and partly in S-type biotites (NAR-1), compared to I-type biotites. Thus, in the broad sense, Ge-enrichment increases in the order of I-type biotites < S-type biotites < A-type biotites. Ge varies from 2.6 to 8.6 ppm in A-type biotites, 2.7 – 4.2 ppm in S-type biotites, and 1.2 – 2.6 ppm in I-type biotites.

High relative Zr and Hf abundances occur in the less fractionated A-type biotites (LOV-1, LOV-2, LOV-5, LOV-6). The remaining Zr and Hf sample abundances decrease in the order of A-type biotites (LOV-3 and -4), KUI-3 (I-type), S-type biotites, and finally VIG-1 (I-type). Thus, it appears that Zr and Hf are enriched in the less fractionated A-type biotites in addition to the more fractionated I-type biotites. The cause for this odd behavior is unknown, but may originate from analytical errors. Nonetheless, Zr abundances range between 0.4 – 20 ppm in A-type biotites, 0.1 – 0.7 ppm in S-type biotites, and <0.1 – 4.3 in I-type biotites. The respective ranges for Hf are 0.1 – 2.8 ppm, <0.1 – 0.1 ppm, and <0.1 – 0.2 ppm.

Like Zr & Hf, niobium and tantalum exhibit similar relative characteristics. A-type biotites and NAR-1 (S-type) are enriched in both Nb and Ta, although NAR-1 is considerably more Ta-enriched than A-type biotites, whereas the most fractionated A-type biotites are somewhat more abundant in Nb compared to NAR-1. I-type biotites and OLR09 are largely Nb & Ta-depleted in comparison, although OLR09 contains the highest abundances of both Nb and Ta within these Nb & Ta-depleted samples. Nb content in A-type biotites varies from about 67 to 460 ppm, 42 – 360 ppm in S-type biotites, and 5.4 – 21 ppm in I-type biotites. Ta contents vary between 2.8 to 47 ppm, 3.1 – 97 ppm, and <0.1 – 1.6 ppm, respectively.

Cadmium and corrected ^{113}In contents were mostly below statistical detection limits, and as a results, only a handful of data points were collected. All biotite Cd measurements were below detection limits in LOV-2.1, LOV-3, LOV-6.1, LOV-6.2, and NAR-1. All other samples contained one measurement above detection limits, with the exception of LOV-5, which contained three. Based on these limited results, Cd ranges from 0.2 to 0.5 ppm in A-type biotites, 0.5 ppm in S-type biotites, and 0.2 – 0.3 ppm in I-type biotites. Data points above detection limits were more numerous for ^{113}In (9 Cd vs. 30 ^{113}In), however all analyses in I-type biotites and NAR-1 were below detection limits. Thus, concentration ranges can be given only for A- and S-type biotites: 0.1 – 0.9 ppm (A-type) and 0.4 – 0.5 ppm (S-type).

Table 11. Representative biotite, muscovite (red rows), and amphibole (green rows) LA-ICP-MS analysis data. Element abundances are in ppm.

Sample	Li	Be	B	Sc	Co	Ni	Cu	Zn	Ga!	Ge	Zr	Nb	Cd	^{113}In*	^{115}In*	Sn	Ba	Nd	Dy	Ho	Hf	Ta	Pb
LOV-1	450	1.1	1.7	8.9	25	3.5	23	780	27	3.8	1.4	82	b.d.	b.d.	0.2	115	1080	2.3	0.4	0.1	0.1	4.7	11.2
LOV-2.1	640	0.9	b.d.	9.5	28	3.6	0.1	1020	18	4.1	1.9	170	b.d.	b.d.	0.1	18	1540	0.1	b.d.	b.d.	0.2	8.0	6.0
LOV-2.2	660	0.9	1.0	8.8	30	3.8	0.1	1190	31	3.7	2.6	155	b.d.	b.d.	0.1	33	1760	b.d.	b.d.	b.d.	0.5	9.4	6.4
LOV-3	1320	3.3	b.d.	60	9.9	0.5	0.2	860	60	4.1	0.7	400	b.d.	0.3	0.6	93	340	b.d.	b.d.	b.d.	0.1	15.0	4.9
LOV-4	800	5.2	0.5	72	17.3	2.5	0.1	900	40	3.0	1.0	189	b.d.	0.4	0.5	62	321	0.2	0.1	<0.1	0.4	5.2	6.2
LOV-5	630	1.0	0.9	27.3	15.7	1.1	13.0	1180	28	3.6	6.7	96	b.d.	0.3	0.2	45	830	3.9	0.7	0.1	0.9	4.0	13.2
LOV-6.1	780	0.6	0.5	2.8	15.6	0.7	0.1	690	13	2.9	1.9	175	b.d.	b.d.	0.1	32	700	b.d.	b.d.	b.d.	0.1	16.3	9.4
LOV-6.2	760	0.9	0.4	19.8	20.0	1.0	0.1	1250	36	5.9	9.3	211	b.d.	0.2	0.1	39	314	0.1	<0.1	<0.1	1.3	22.4	8.0
OLR09	167	0.4	0.6	34	53	62	20.5	340	6	3.3	0.3	55	b.d.	b.d.	0.1	11.6	740	2.6	0.2	<0.1	<0.1	3.7	3.6
NAR-1	2290	2.2	0.2	13.4	17.1	19.3	0.5	1260	40	4.0	0.5	330	b.d.	b.d.	0.1	32	72	0.2	b.d.	b.d.	0.1	95	4.8
VIG-1	160	1.9	0.4	2.1	74	147	18	600	7	1.3	<0.1	9.4	b.d.	b.d.	<0.1	0.4	470	1.2	<0.1	<0.1	b.d.	0.1	2.7
KUI-3	207	0.6	0.3	20.1	65	126	0.6	330	NA	2.4	0.1	19.6	b.d.	b.d.	<0.1	1.9	1630	b.d.	b.d.	b.d.	<0.1	1.4	1.5
NAR-1	680	5.7	56	92	1.0	0.9	0.1	95	151	0.9	1.3	70	b.d.	b.d.	0.6	29	67	b.d.	<0.1	b.d.	0.1	2.6	4.6
LOV-1	8.5	15	1.9	101	9.9	0.6	0.4	940	39	7.7	190	53	0.7	3.6	3.7	860	81	290	71	14.3	12.3	3.6	7.7
LOV-2.1	10.4	12.9	0.6	89	23.0	2.5	0.4	860	41	8.1	163	110	1.1	1.3	1.1	7.9	115	500	90	17.6	10.8	5.3	8.4
LOV-2.2	9.3	14.3	0.8	94	23.0	2.5	0.4	920	41	8.5	135	87	1.4	0.9	1.3	9.9	89	440	82	16.3	8.0	3.1	8.4

b.d. = below detection limit; * = total indium concentration calculated from masses 113 and 115 (corrected for spectral interferences); <0.1 indicates an informational concentration; ! = corrected for doubly charged ^{138}Ba – concentrations informational and speculative; NA = not analyzed (assumed to be 0). See Chapter 3.5.2. for discussion.

Corrected ^{115}In produced more consistent results for biotites. Only six analyses were below detection limits, all in VIG-1. Highest ^{115}In abundances are encountered in A-type biotites (apexing in LOV-3 and -4), followed by S-type biotites, and then I-type biotites. ^{115}In concentrations range from 0.1 to 1.1 ppm in A-type biotites, 0.1 – 0.2 ppm in S-type biotites, and up to 0.1 ppm in I-type biotites.

Tin is similar to ^{115}In for the most part. A-type biotites contain the highest abundances, S-type biotites are intermediate, and I-type biotites are Sn-depleted relative to the other samples. However, the highest Sn abundances are encountered in LOV-1, and then followed by LOV-3 and -4. Sn abundances vary between about 13 and 330 ppm in A-type biotites, 12 – 37 ppm in S-type biotites, and 0.3 – 2.1 ppm in I-type biotites.

REE (Nd, Dy, Ho) abundances were generally very low in biotites, less than about 0.5 ppm. LOV-5, however, is comparably very high in REEs (up to about 26 ppm). VIG-1 is also relatively high in Nd (up to about 15 ppm), but not in Dy or Ho. Inspection of the respective ablation signals do not indicate inclusions or chemical zonation, which could cause concentration calculations to be abnormally high. Nd abundances range from <0.1 to 26 ppm in A-type biotites, <0.1 – 2.6 ppm in S-type biotites, and <0.1 – 15 ppm in I-type biotites. For Dy, the respective ranges are <0.1 – 2.9 ppm, <0.1 – 0.2 ppm, and <0.1 – 0.5 ppm. For Ho, the ranges are <0.1 – 0.7 ppm in A-type biotites, <0.1 ppm in S-type biotites, and up to 0.1 ppm in I-type biotites.

With respect to the biotites and amphiboles hosted by orthoclase ovoids in LOV-1, LOV-2.1, and LOV-2.2, only limited data is available (Appendices 8 and 9). Therefore, robust estimates about enrichment or depletion cannot be made. However, based on the limited data, the ovoid-hosted biotites and amphiboles do not appear to be enriched or depleted in any element compared to biotites and amphiboles that are not enclosed by orthoclase ovoids.

4.4.2. Muscovite and amphibole

Data for muscovites and amphiboles are mentioned and characterized only briefly, and the reader is referred to Table 11 for disclosure on representative element ranges. Since muscovites were measured only from one S-type granite sample (NAR-1), and amphiboles from one A-type granite sub-type (wiborgite; LOV-1, -2.1, and -2.2),

meaningful comparisons between different granite types cannot be made. Nevertheless, representative muscovite and amphibole abundances are ratioed to the respective S- and A-type sample representative biotites in Fig. 21.

Compared to biotite, muscovite appears to be depleted in Li, Co (considerably, hereafter *c*), Ge, Nb, Ta (*c*), and enriched in Be, B (*c*), Sc, Ga, Zr, In (*c*), and Hf. Concentrations of Sn are effectively similar in muscovite and biotite, and concentrations of Cd and Ho were below detection limit in both minerals. Nd was below detection limit in muscovite, and Dy in biotite. Thus, a ratio could not be calculated for these elements. Nonetheless, it is inferred that Nd is enriched in biotite relative to muscovite, and Dy in muscovite relative to biotite (to a small degree – the concentrations are low).

Amphiboles tend to be depleted in Li (*c*), Co, Nb, and Ta. Tin ratios are conflicting in that in LOV-1 Sn is *enriched*, whereas in LOV-2.1 and LOV-2.2 Sn is *depleted*. Moreover, Co appears to be more depleted in LOV-1 than in LOV-2's. However, the Co and Sn anomalies in LOV-1 are caused by Co and Sn outliers in amphibole. Nevertheless, Co, Ga, Nb, and Ta are only slightly depleted. Amphiboles are enriched in Be, Sc, Ga, Ge, Zr (*c*), In, REEs (*c*), and Hf (*c*). Concentrations of B are effectively similar in both minerals, and Cd, Dy, and Ho were below detection limit (the latter two elements only in LOV-2.1 and -2.2, in addition to Nd) in biotites so that a ratio could not be calculated for these elements. However, it is apparent that amphiboles are enriched relative to biotite in the "below detection limit" elements since all elements were above detection limit in all amphibole analyses.

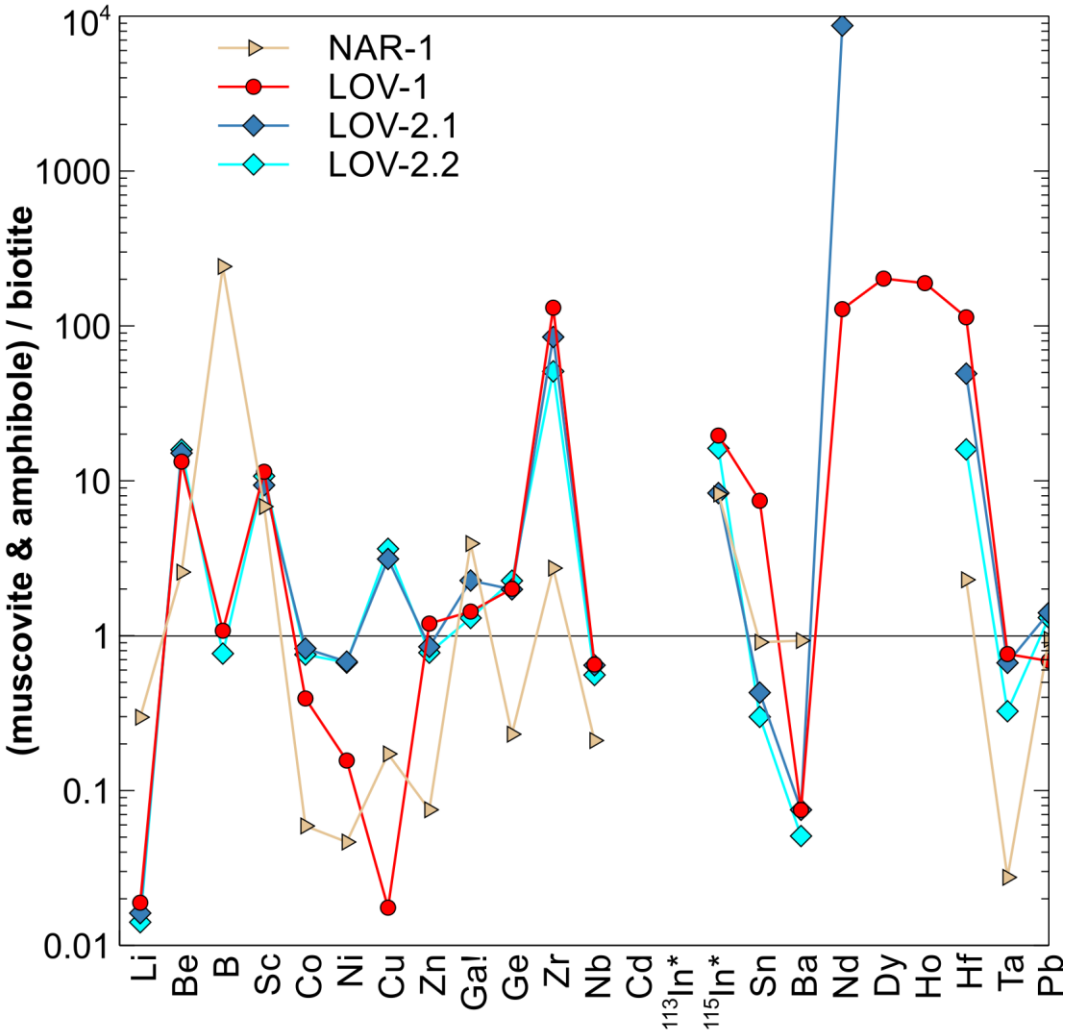

Figure 21. Representative muscovite (NAR-1) and amphibole (LOV-1, -2.1, and -2.2) concentrations ratioed to the respective representative biotite concentration (i.e. muscovite-NAR-1 / biotite-NAR-1, etc.). Missing data or gaps indicate that an element was below detection limit in biotite or muscovite. * = total indium concentration calculated from masses 113 and 115 (corrected for spectral interferences); ! = empirically corrected for doubly charged ^{138}Ba, see Chapter 3.5.2. for discussion.

4.4.3. Trace element fractionation trends

Many fractionation indicators used in literature (e.g. K/Rb, Ba/Rb, Nb/Ta, Zr/Hf, 1/TiO_2, Al/Ga, Ni/Co, to name a few) were considered as fractionation indicators for the study data. K/Rb is a often used fractionation indicator for granitic trioctahedral micas (Černý et al. 1985). However, since Rb was not included in the LA-ICP-MS analysis menu, an alternative was needed. Nb/Ta is another frequently used fractionation indicator, and was tested on the data. However, the Nb/Ta scheme was not suitable for the whole bulk of the study data, since the Nb contents in LOV-3 and -4 were largely scattered (Appendix 10),

and the Nb/Ta ratios were abnormally high in VIG-1 due to strong Ta depletion (Fig. 31 B; Nb/Ta 45 – 208). Moreover, the Nb/Ta ratio is more suitable for extremely fractionated granites, and most samples in this study do not fit this criterion (e.g. Taylor 1965, Černý et al. 1985).

Indeed, there is no perfect fraction indicator for rocks of broad genetic backgrounds. However, cobalt concentrations appeared to produce smooth curvilinear trends reminiscent of most fractionation plots used in literature. Cobalt has an affinity to Mg in granitic trioctahedral micas (Carr & Turekian 1961, Tischendorf et al. 2001), and since the more primitive samples were relatively high in Mg, and most evolved samples relatively high in Fe (Fig. 20, Table 8), a linear correlation was observed. Co as a fractionation indicator takes into account the abundances of Mg and Fe, which also form the clearest discrepancies between major element oxide contents in the study biotites. Thus, Co was selected as a fractionation indicator. However, to remain consistent with the Fe-dependent biotite classification (and with *mgli* to an extent), Mg / (Mg + Fe) was used as an auxiliary fractionation indicator. Element fractionation on the basis of Co are shown in Figs. 22 - 25, and on the basis of Mg / (Mg + Fe) in Appendix 13.

As a generalization, the relative contents of the following elements increase with advancing fractionation: Li, B (weakly), Ga, Ge, Zr & Hf, Nb & Ta, In, and Sn. Co contents decrease, whereas Sc does not exhibit any distinctive linear or curvilinear trends. Be is an oddity: when plotted as a function of advancing fractionation, Be produces a horseshoe-shaped trend. That is, the Be contents are relatively high in the least and most fractionated granites. REEs appear to increase with fractionation (albeit weakly), but the relatively high REE abundances in A-type biotites are limited to outliers from a single sample (LOV-5). Thus, any correlations with fractionation indicators are likely spurious.

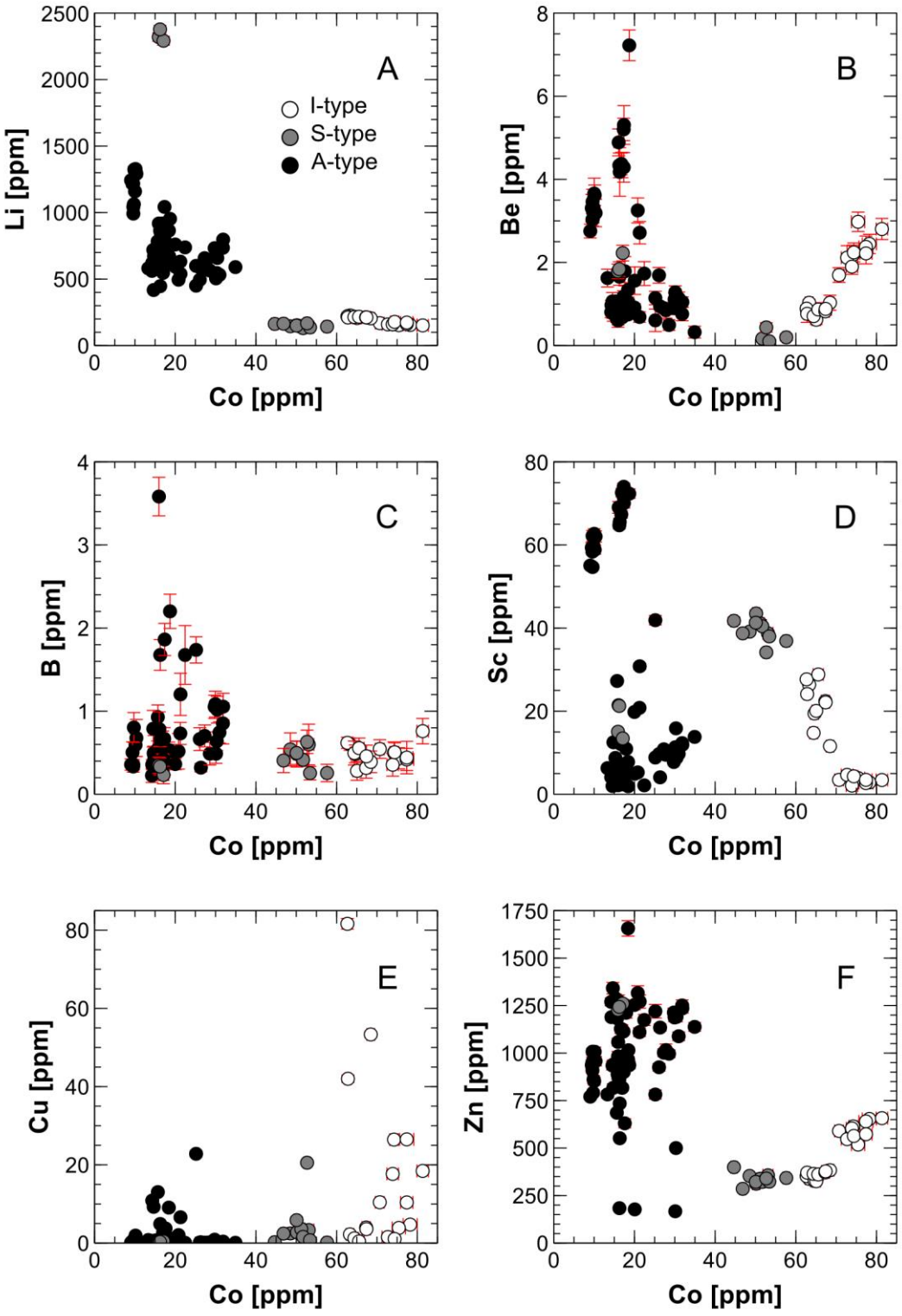

Figure 22. Biotite variation diagrams for A) Li, (B) Be, (C) B, (D) Sc, (E) Cu, and (F) Zn vs. Co. Error bars indicate a combined 1 σ of LA-ICP-MS transient signal noise and counting statistical errors.

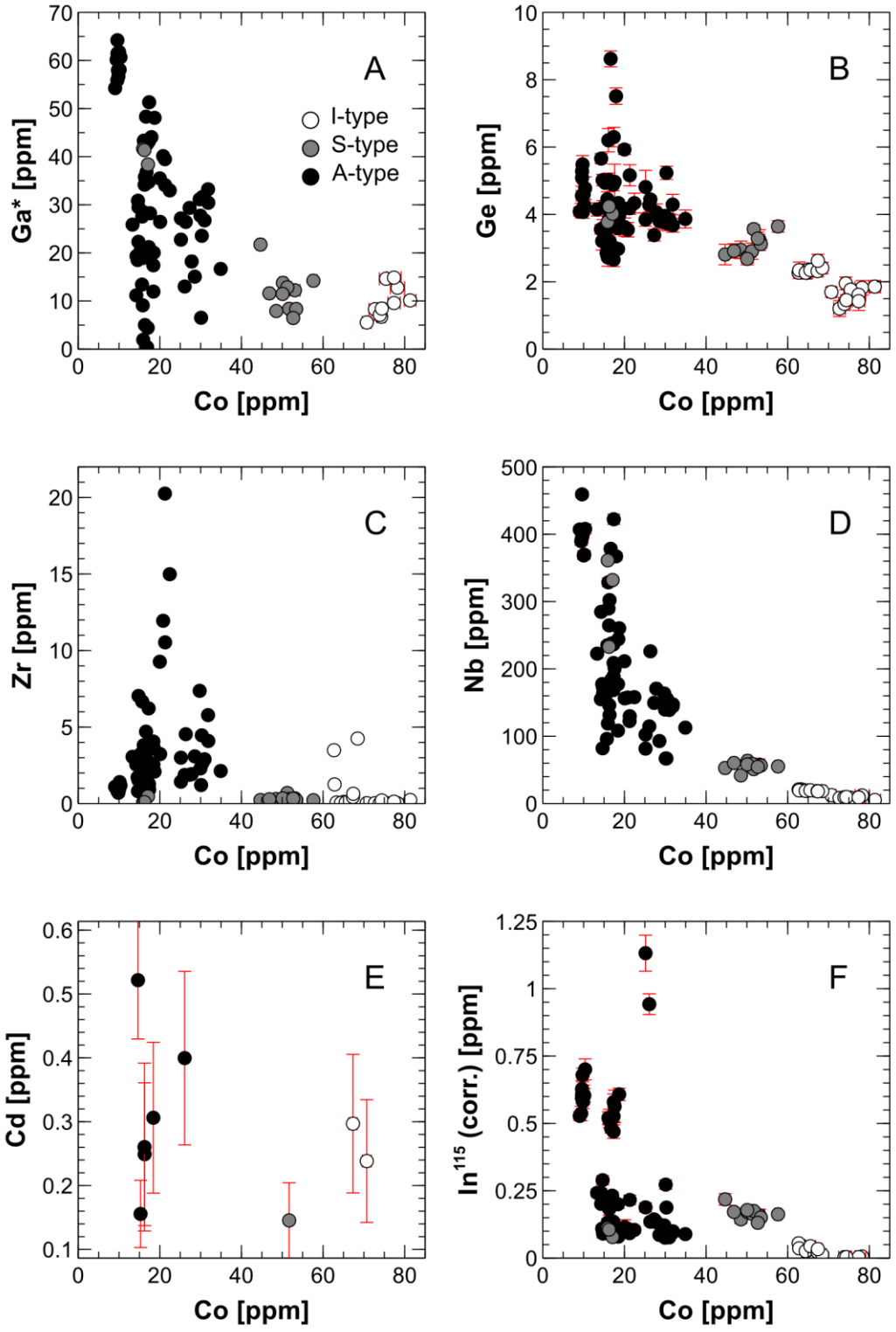

Figure 23. Biotite variation diagrams for (A) Ga, (B) Ge, (C) Zr, (D) Nb, (E) Cd, and (F) total In vs. Co (In concentration calculated from mass 115 and corrected for spectral interferences). Note that Ga concentrations (*) have been empirically corrected for doubly charged ^{138}Ba, and the reported concentrations are speculative. See Chapter 3.5.2. for discussion. Error bars indicate a combined 1 σ of LA-ICP-MS transient signal noise and counting statistical errors.

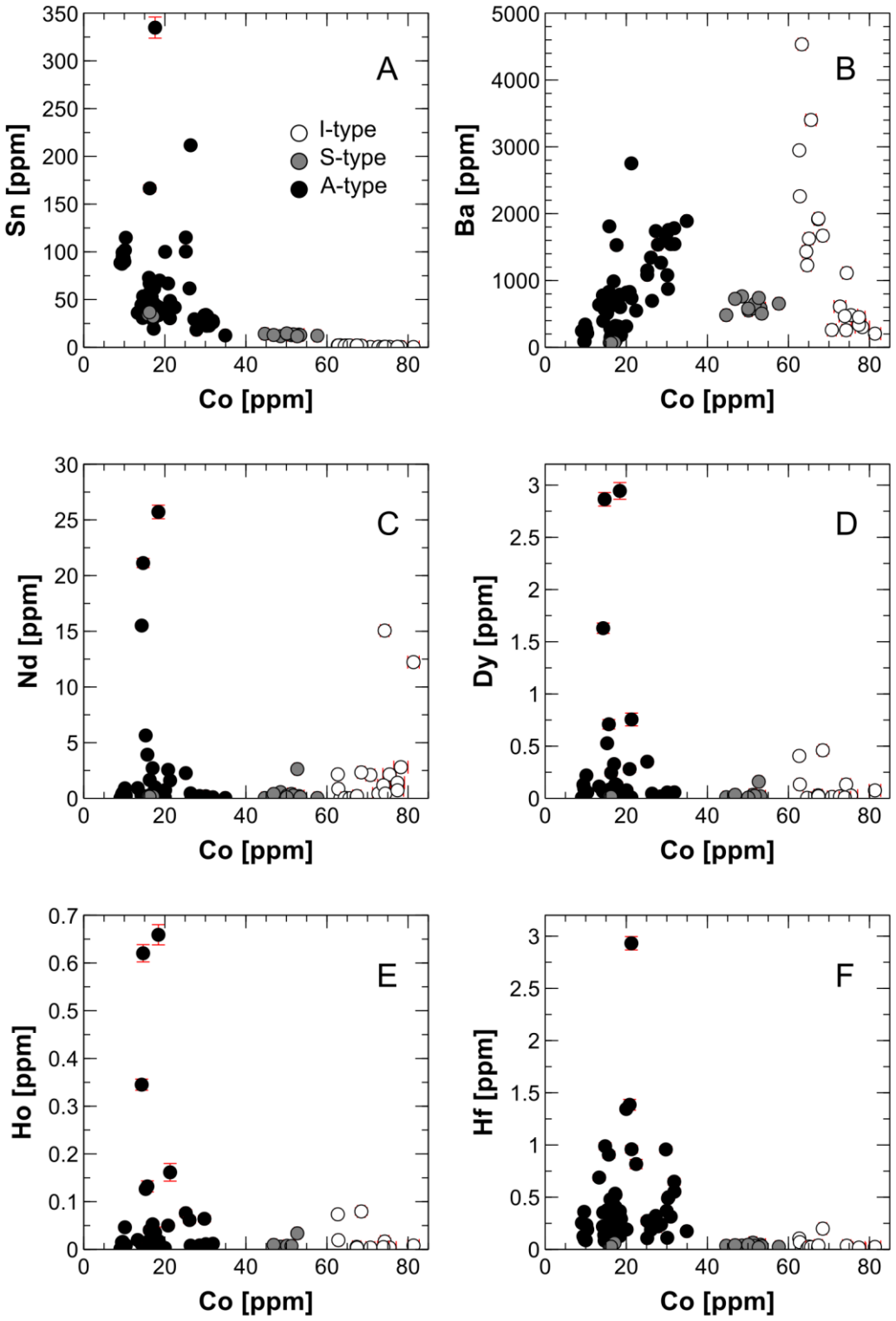

Figure 24. Biotite variation diagrams for (A) Sn, (B) Ba, (C) Nd, (D) Dy, (E) Ho, and (F) Hf vs. Co. Error bars indicate a combined 1 σ of LA-ICP-MS transient signal noise and counting statistical errors.

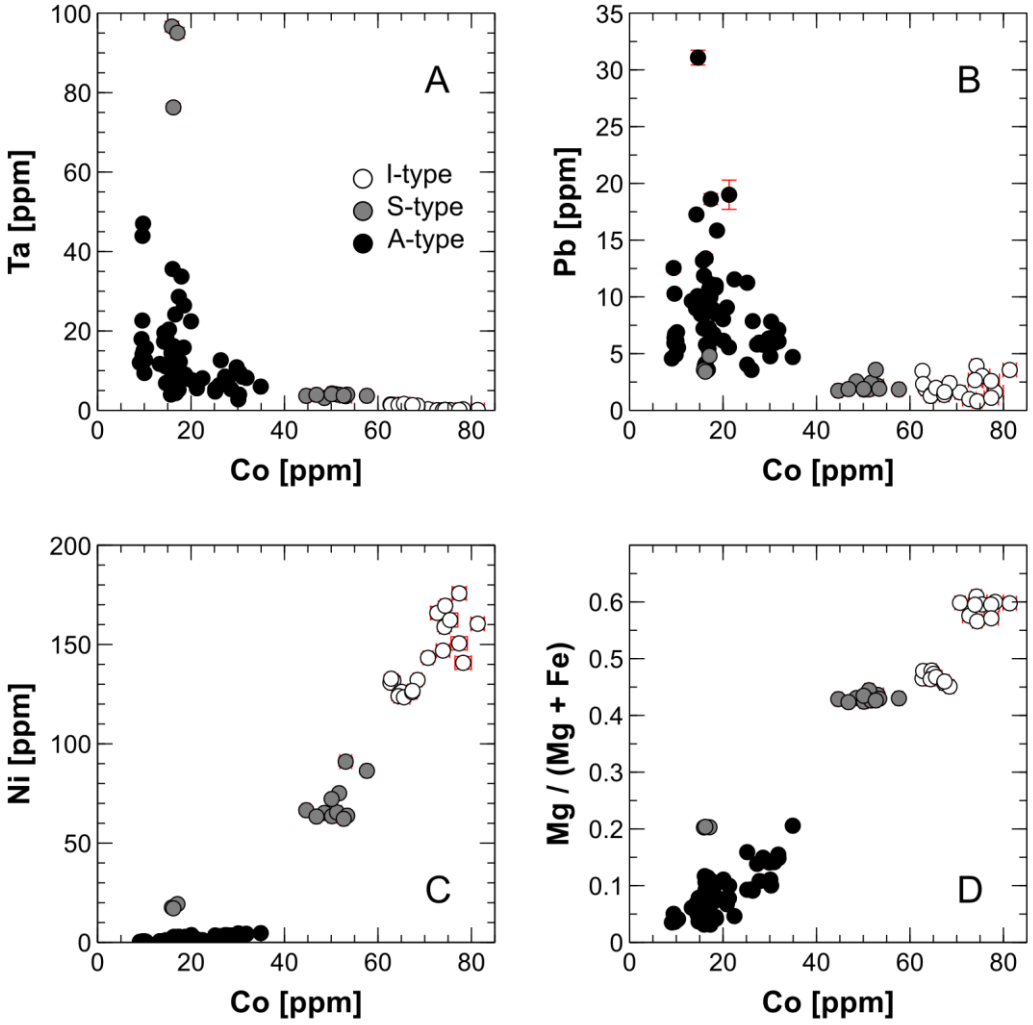

Figure 25. Biotite variation diagrams for (A) Ta, (B) Pb, (C) Ni, and (D) Mg/(Mg+Fe) apfu vs. Co. Error bars indicate a combined 1 σ of LA-ICP-MS transient signal noise and counting statistical errors.

4.4.4. Other trace element correlations

Linear or curvilinear trends between elements in biotites other than Mg, Fe, Co, and Ni were relatively scarce. That is, most elements correlate with Mg and Co, and therefore by extension with Fe and Ni, but otherwise correlations were mostly weak and trends were scattered. The strongest non-ferromagnesian correlations and trends were exhibited in Li, Be, Sc, Ge, Zr & Hf, Nb & Ta, and REEs (Figs. 26 – 30), although even many of the strongest (in a relative sense) correlations and trends were somewhat weak or interpretative.

Lithium (Fig. 26) appears to correlate linearly with Al and K once the Li content in biotite

reach a level above of about 500 ppm (Al: correlation is insignificant below 500 ppm Li; $r_{>500\ ppm\ Li}$ = 0.78 // K: $r_{<500\ ppm\ Li}$ = insignifcant; $r_{>500\ ppm\ Li}$ = 0.52). Likewise, linear Li-correlation is evident with Nb & Ta (Nb: r_{all} = 0.77; $r_{all\ -\ NAR\text{-}1}$ = 0.87 // Ta: r_{all} = 0.81), and Li-Ba exhibit somewhat curvilinear correlation from about 2500 ppm down to about 500 ppm Li.

Correlations for Be are weak (Fig. 27), and likely spurious, but nonetheless, slight positive linear correlation is indicated between Be and Na (r = 0.58). Be in A-type biotites seems to correlate positively with Al (r = 0.89), and negatively in S- or I-type biotites (r = insignificant). Be and Sc appear mostly uncorrelated visually, however r_{all} = 0.72, and in LOV-3 and LOV-4 r = 0.81.

Weak positive and linear correlation is exhibited between Sc (Fig. 28) and Na (r = 0.62), and negative curvilinear correlation between Sc and Ca. That is, the higher the Ca content, the lower the Sc content. The correlations between Sc and In, Sn, Nd are highly speculative, but are reminiscent of a negative curvilinear correlation.

Likewise, Germanium (Fig. 29) shows weak linear correlations with Si, K, (corrected) Ga, and Pb (r_{Si} = -0.56, r_K = -0.50, r_{Ga} = 0.58, r_{Pb} = 0.50), but somewhat stronger correlation with Nb (r = 0.72).

Zr & Hf (r = 0.91), Nb & Ta (r_{all} = 0.61, $r_{all\ –\ NAR\text{-}1}$ = 0.80), and REEs ($r_{Nd\text{-}Dy}$ = 0.87, $r_{Nd\text{-}Ho}$ = 0.86, $r_{Dy\text{-}Ho}$ = 1.00) correlate mainly only with each other (Fig. 30). That is, Zr is correlated with Hf, but not with other elements, etc. However, Nb is an exception to this in that Nb appears to correlate curvilinearly with Ba (r = -0.45).

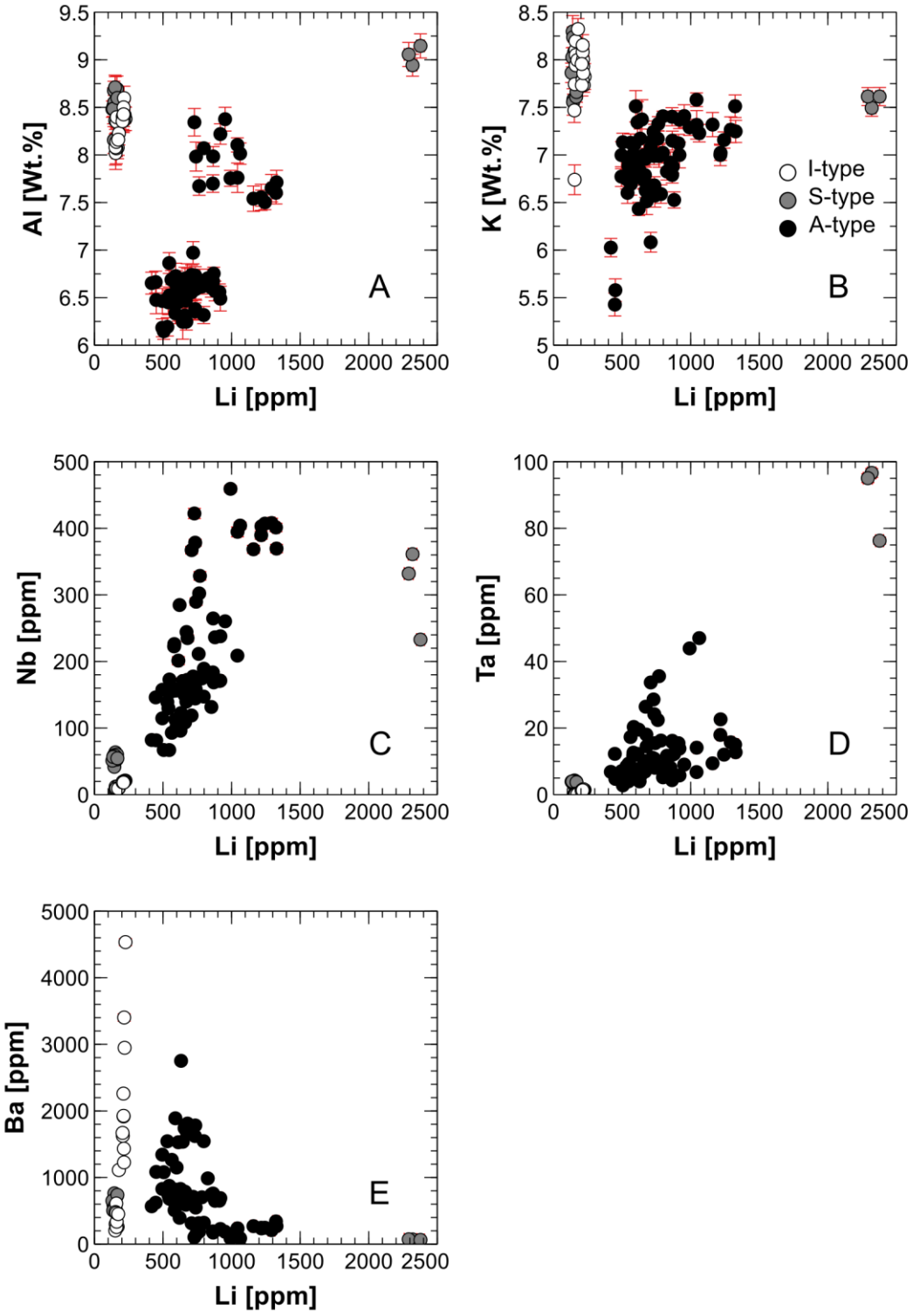

Figure 26. Biotite variation diagrams for (A) Al vs. Li, (B) K vs. Li, (C) Nb vs. Li, (D) Ta vs. Li, (E) Ba vs. Li. Error bars indicate a combined 1 σ of LA-ICP-MS transient signal noise and counting statistical errors.

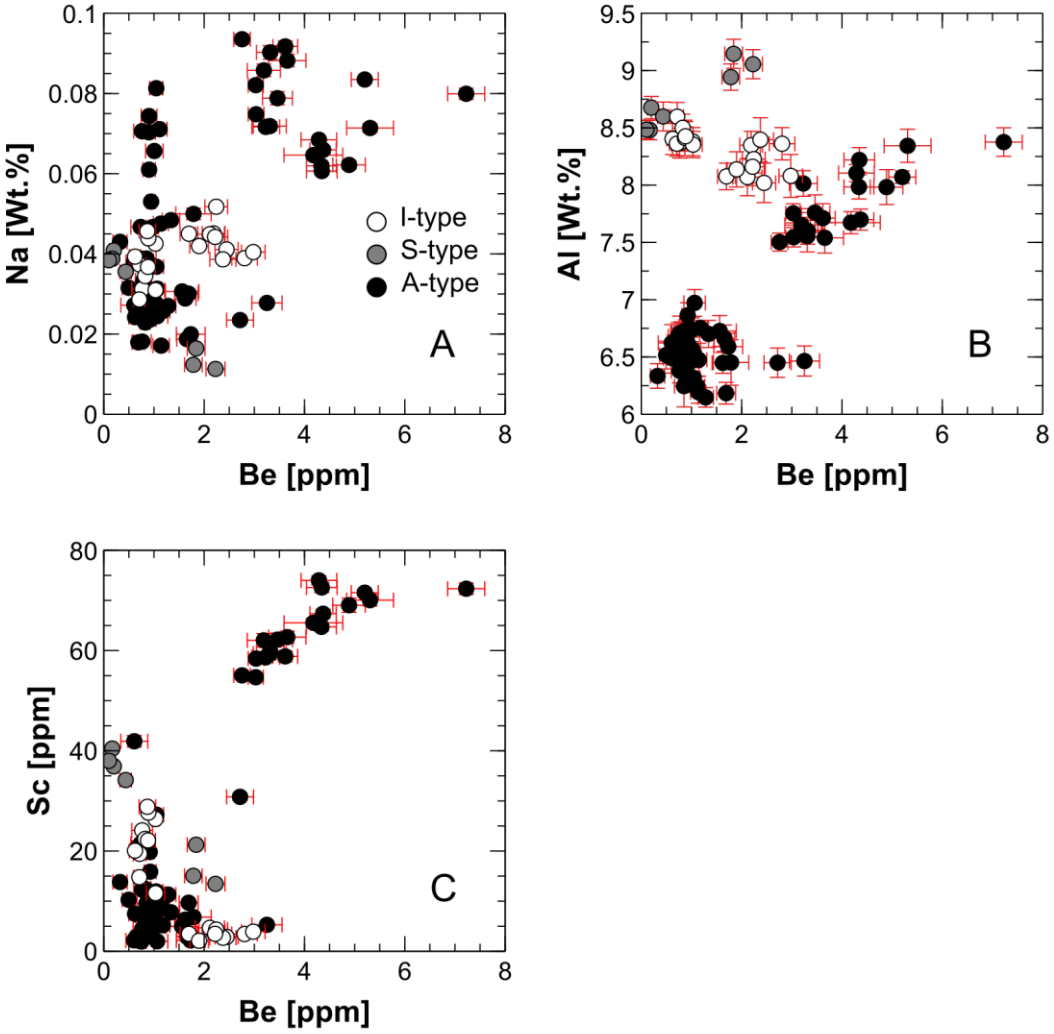

Figure 27. Biotite variation diagrams for (A) Na vs. Be, (B) Al vs. Be, and (C) Sc vs. Be. Error bars indicate a combined 1 σ of LA-ICP-MS transient signal noise and counting statistical errors.

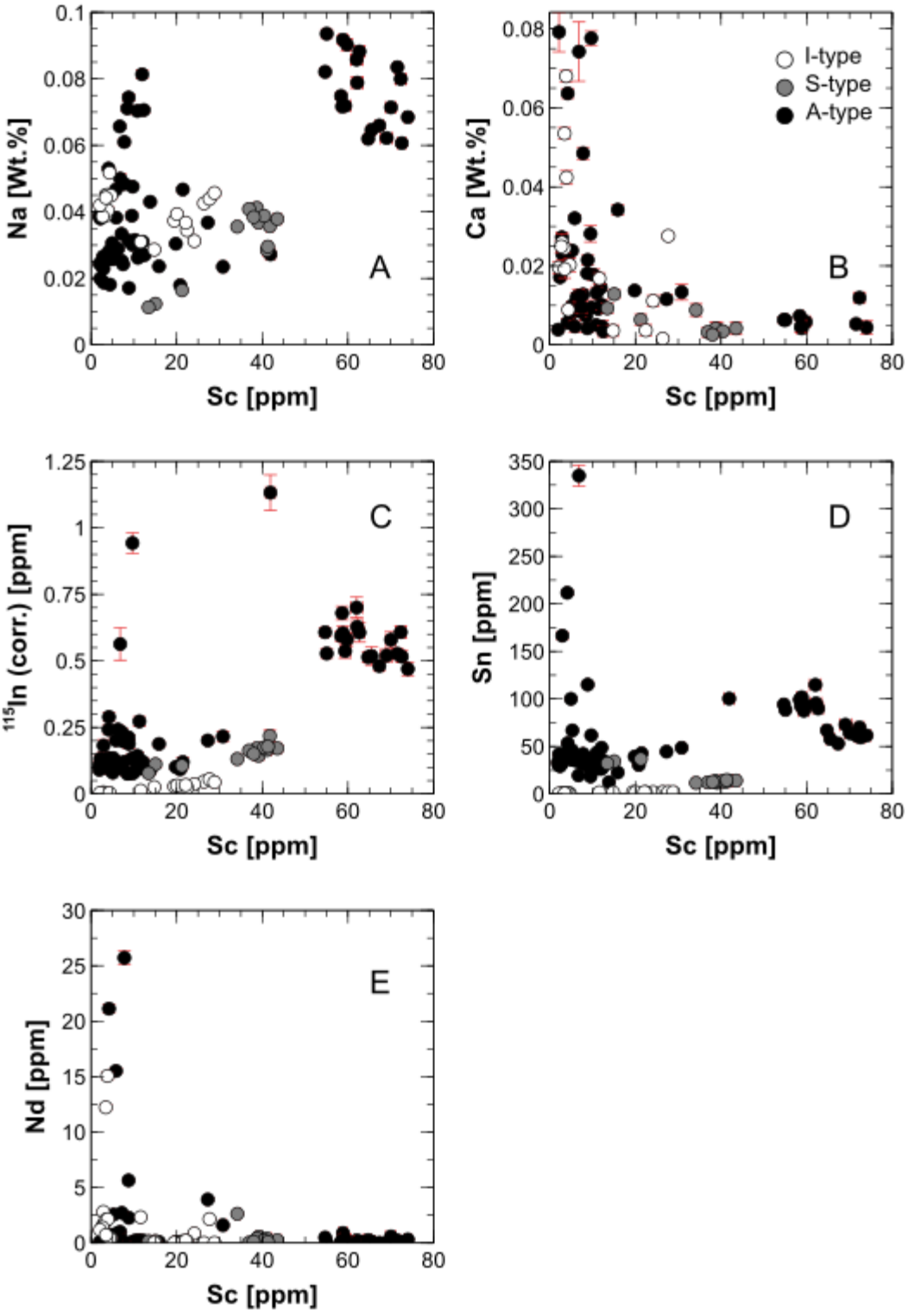

Figure 28. Biotite variation diagrams for (A) Na vs. Sc, (B) Ca vs. Sc, (C) In vs. Sc, (D) Sn vs. Sc, and (E) Nd vs. Sc. "^{115}In (corr.) [ppm]" refers to the total indium concentration calculated from mass 115 that has been corrected for spectral interferences. Error bars indicate a combined 1 σ of LA-ICP-MS transient signal noise and counting statistical errors.

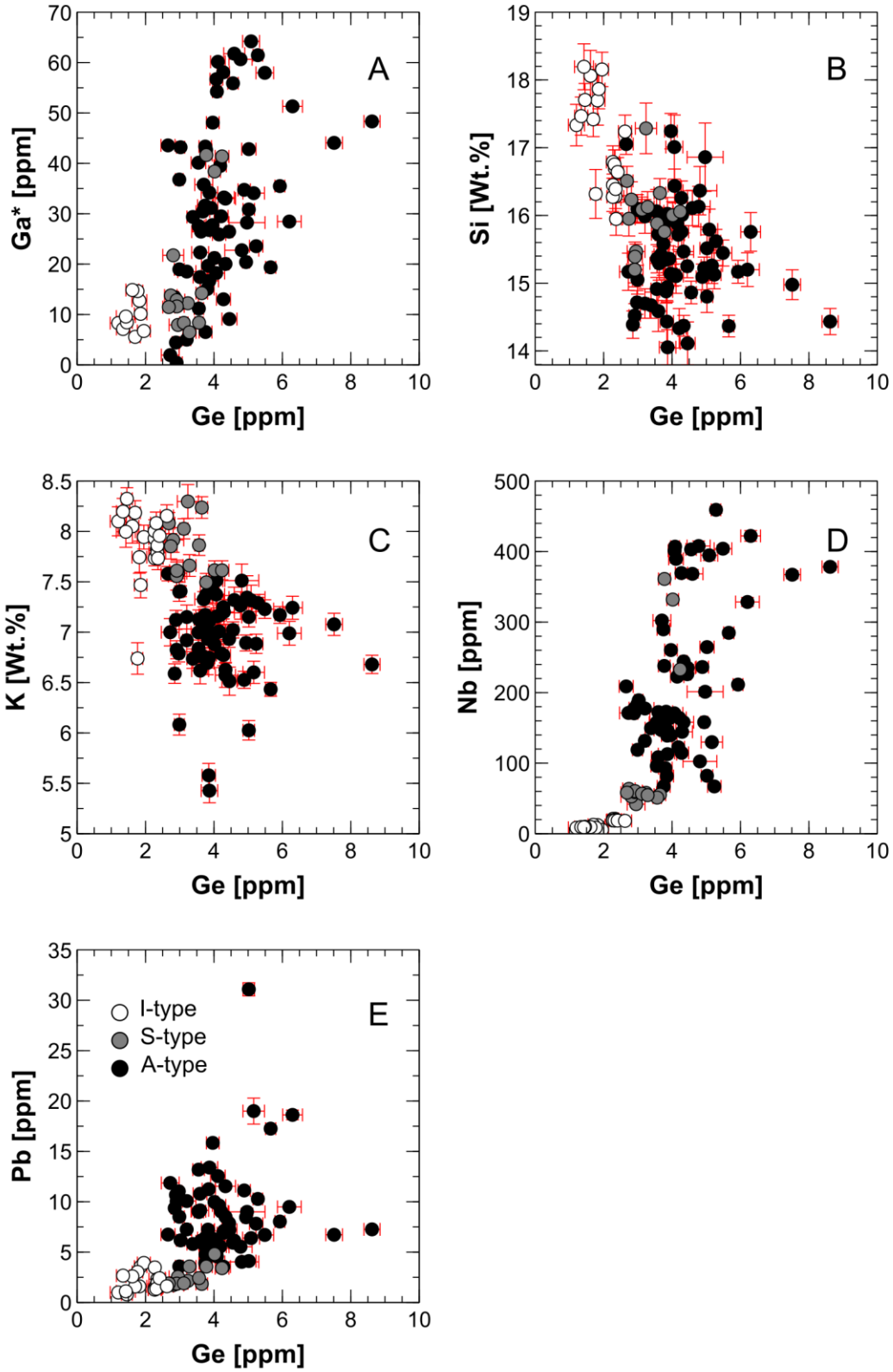

Figure 29. Biotite variation diagrams for (A) Ga vs. Ge, (B) Si vs. Ge, (C) K vs. Ge, (D) Nb vs. Ge, and (E) Pb vs. Ge. Note that Ga concentrations (*) have been empirically corrected for doubly charged ^{138}Ba, and thus the reported concentrations are speculative. See Chapter 3.5.2. for discussion. Error bars indicate a combined 1 σ of LA-ICP-MS transient signal noise and counting statistical errors.

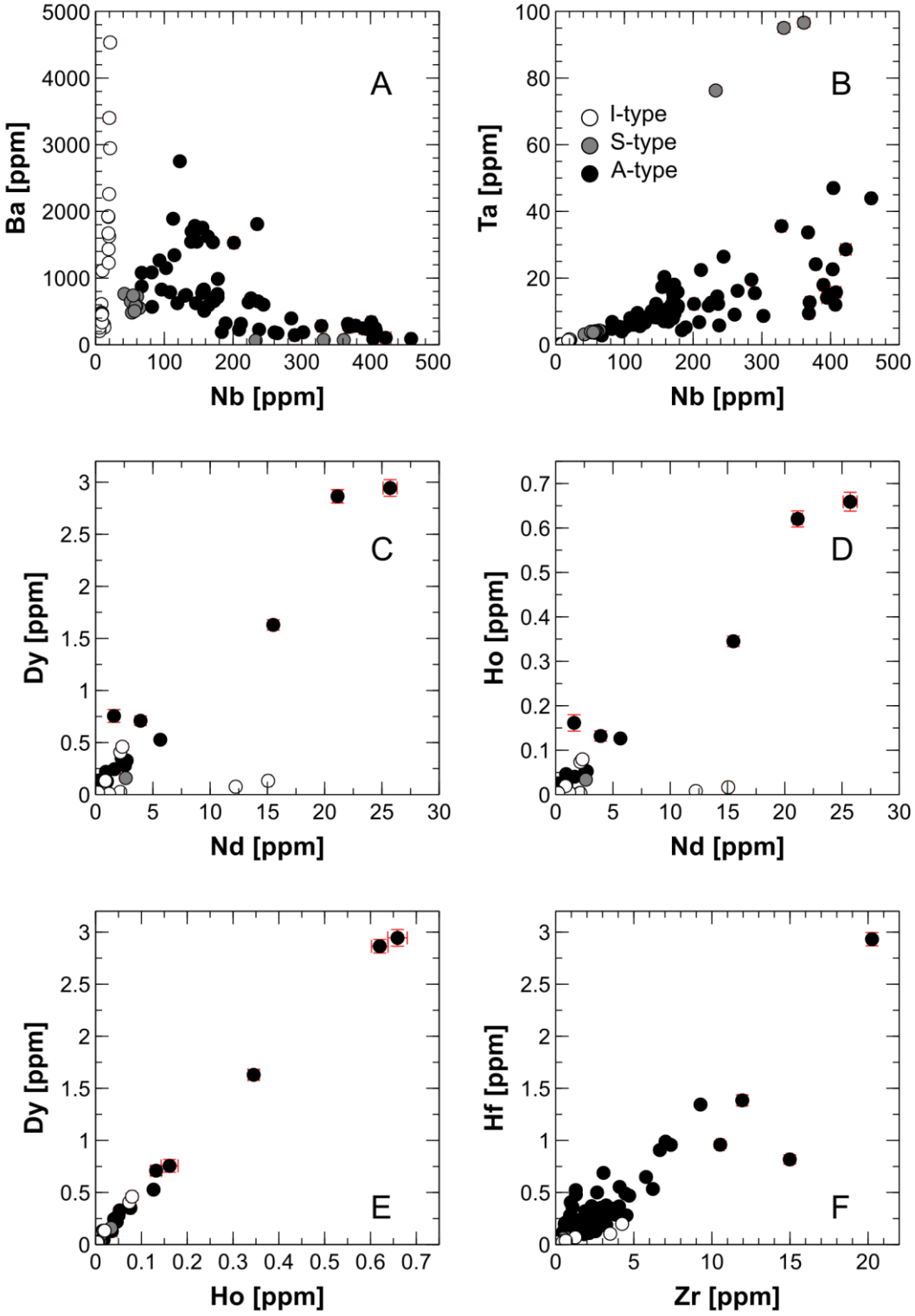

Figure 30. Biotite variation diagrams for (A) Ba vs. Nb, (B) Ta vs. Nb, (C) Dy vs. Nd, (D) Ho vs. Nd, (E) Dy vs. Ho, and (F) Hf vs. Zr. Error bars indicate a combined 1 σ of LA-ICP-MS transient signal noise and counting statistical errors.

4.4.5. Bulk trace elements vs. in situ trace elements

Representative biotite trace element data were ratioed to the respective whole-rock and Granite Average (after Turekian & Wedepohl 1961) data to approximate which elements are enriched or depleted relative to the bulk rock and Granite Average chemistry (Fig. 31). A Granite Average was used because the amount and meaningfulness of the corresponding elements measured from both whole-rock and biotites are relatively low (Ni, Cu, Zn, Zr, Nb, Ba).

Compared to whole-rock data, all representative biotites are enriched in Zn and Nb, and depleted in Zr. As a whole, A-type biotites are the least Zr-depleted, followed by S-type biotites and finally I-type biotites, whereas Zn & Nb -enrichment decreases in the sequence S-type biotites > A-type biotites > I-type biotites. Ni is enriched in S- and I-type biotites, and is either enriched or depleted in A-type biotites. Excluding outliers, Cu is likely depleted in, at least, all A-type biotites.

Compared to the Granite Average value (Turekian & Wedepohl 1961), all representative biotite samples are enriched in Li, Co, Zn, Ge, and depleted in B, Cu, Zr & Hf, Cd, REEs, and Pb. Be is enriched in LOV-3 and LOV-4 and depleted in all remaining samples. In contrast, Ga is depleted in I-type biotites but enriched in A- and S-type samples. Indium is enriched in LOV-1, -3, -4, and -5 but depleted in others. Nb, Ta, and Sn are enriched in NAR-1 and A-type biotites but depleted in OLR09 and I-type biotites. Ni is enriched in S- and I-type biotites, but depleted in A-type biotites. Sc and Ba exhibit variable characteristics, i.e. they are both enriched and depleted within the S-I-A granite types.

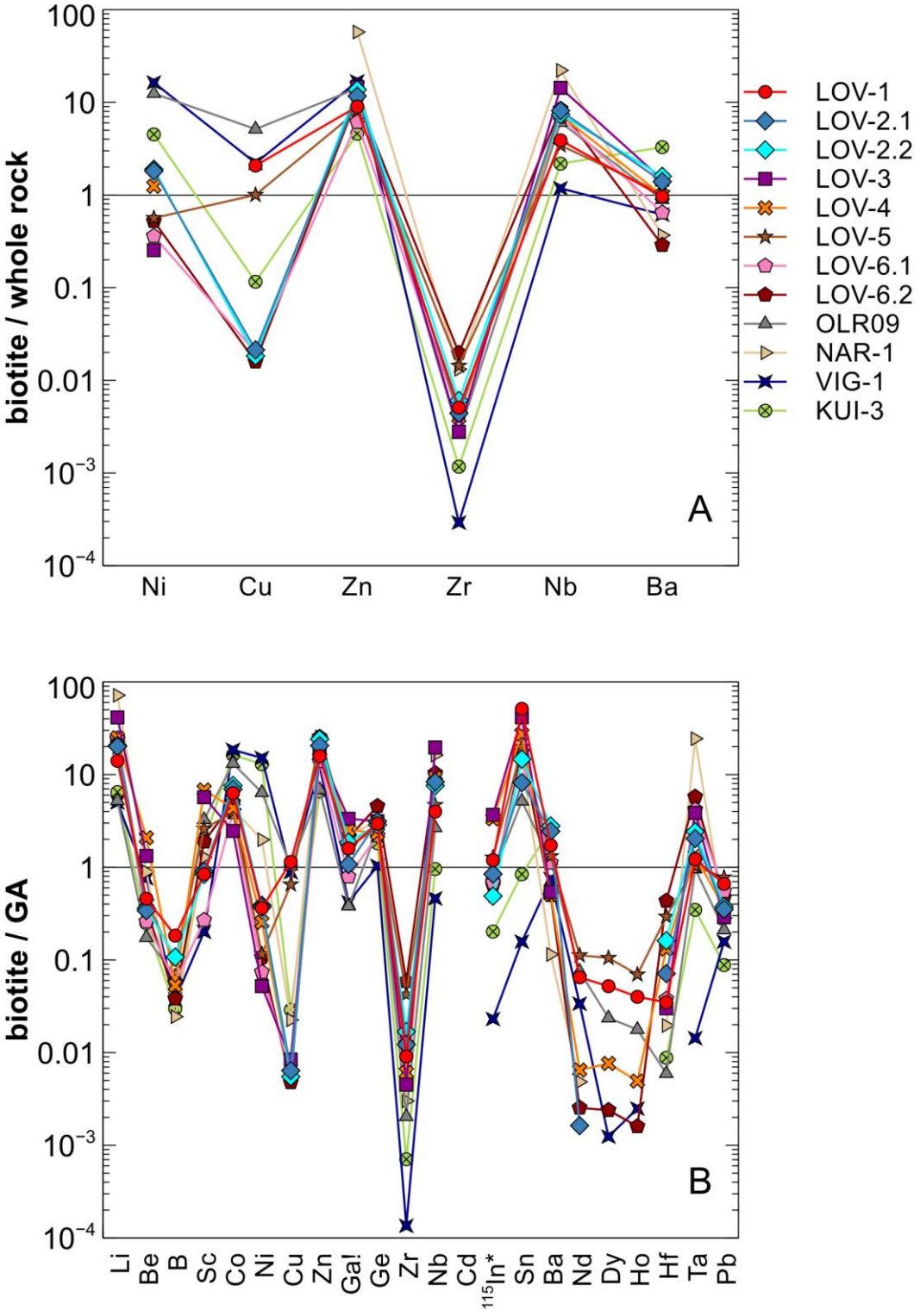

Figure 31. Representative biotite analyses ratioed to whole-rock analysis data (A) and Granite Average (GA) data (B) after Turekian & Wedepohl (1961). Missing data or gaps in (A) indicate that an element was below detection limit in whole-rock analysis, whereas in (B) gaps indicate that an element was below detection limit in biotite analysis. * = total indium concentration calculated from mass 115 (corrected for spectral interferences); ! = empirically corrected for doubly charged ^{138}Ba, see Chapter 3.5.2. for discussion.

5. DISCUSSION

First, it should be noted that the trace element distribution in granitic trioctahedral micas is a function of many factors, e.g. temperature, pressure, crystal fractionation (of micas and other phases), metasomatic processes, to name a few. The evaluation of all these factors, with respect to the study samples, and in addition to references from literature, are far beyond the scope of this study. Thus, in order to simplify discussion, the initial approximations are – unless stated otherwise – that the distribution of trace elements in granitic trioctahedral micas is correlated mainly with (a) granite type (i.e. type of parental magma composition) or (b) progressing fractionation. Moreover, it is assumed that elements fractionate only on a charge and ionic radius basis (c.f. Blundy & Wood 2003).

5.1. Bulk rock and other analyzed phases vs. biotite

If trace elements are used as fractionation indicators, they should ideally be identical in both whole-rock and minerals. However, with the trace element menus used in this study (Table 6, Table 11), this was not possible. Nevertheless, the employed bulk rock fractionation indicators (Fig. 17) and biotite fractionation indicators (Figs. 22 – 25, Appendix 13) predominantly correlate with one another. The I-type samples (VIG-1, KUI-3) are the least fractionated samples, followed closely by OLR09. A-type samples LOV-1, -2, -5, and -6 are more evolved compared to the I-type samples and OLR09, but more primitive compared to LOV-3, -4, and NAR-1. With respect to A-type granite fractionation, the interpretation that LOV-3 and -4 are the most fractionated A-type samples is supported by the textural, mineralogical, and field criteria in literature (Haapala 1995, Rämö & Haapala 2005, Valkama et al. 2016).

When the analyzed whole-rock trace element compositions are compared to the respective biotite trace element compositions (Fig. 31), it is difficult to give a comprehensive overview of which elements are enriched and which are not on the basis of the S-I-A classification. This is because many elements appear both enriched and depleted within the respective alphabet groups. For example, Ni appears to be enriched in biotites in LOV-1, LOV2, and LOV-4, but depleted in LOV-3, LOV-5, and LOV-6.

Moreover, VIG-1 appears to be depleted in Ba, whereas KUI-3 is enriched. These discrepancies may result from, for instance, instrumental error, different instrument sensitivities, poor sample representativeness (e.g. apparent Cu enrichment in LOV-1, LOV-5, and OLR09 are caused by Cu outliers in the representative biotite data), or because sample populations are low. That is, it is not very meaningful to state that 50 % of I-type samples are enriched in some element with a sample size of two. Another explanation would be that these trace elements are not dominantly controlled by the micas, but rather by several minerals, e.g. feldspars (for Ba) and oxides or sulfides (for Ni). However, the discrepancies are most likely caused by the combined effect of low sample size, sample representativeness, and trace element partitioning between different mineral phases. Because the studied samples represent a wide spectrum of granitoid magmatism (and in some cases metasomatism), generalizations are difficult to make owing to the plethora of factors that control trace element partitioning in evolving melts.

Despite these inconsistencies, the whole-rock and Granite Average values agree in that Ni is enriched in S- and I-type biotites, that Zn is enriched in all biotites, and that Zr (and Cu if outliers are excluded) is depleted in all biotites. Moreover, both plots (Fig. 31) show that Ba enrichment and depletion are variable, as it should be depending on how much K-feldspar the samples contain. Because Be, Nb & Ta, In, and Sn enrichment are often associated with late-stage fractionation (Černý et al. 1985), the observation that A-type granites and NAR-1 are the most evolved samples is supported by the apparent enrichment (on basis of bt/GA) of these elements.

As for the other analyzed mineral phases (amphibole and muscovite), limited data is available. Thus, comparisons were made only on element partitioning between amphibole/muscovite and biotite (Fig. 21). These comparisons largely reflect partition coefficients in literature: Zr and REEs are more readily incorporated in amphibole, whereas Ba in biotites (Arth 1976). Bea et al. (1994) report high partition coefficients (biotite/melt) for Li, Be, Sc, Ni, Zn, Nb, Ta, and low partition coefficients for Ba, Cu, Pb, REEs. No partition coefficients are given for amphiboles, but other than Be and Sc (and Ba, c.f. Arth 1976), which appear to be enrinched in hornblende (Fig. 21), trace elements are distributed according to the coefficients of Bea et al. (1994), i.e. Li, Ni, Zn, etc. are enriched in biotite. The biotite/muscovite partition coefficients of Neves (1997) indicate that Li, Co, Ni, Zn, Nb, Ta, and Pb are more readily incorporated in biotite, whereas Sc,

Ba, Ga, and Sn have an affinity to muscovite. Apart from Sn, Ba, and Pb, whose muscovite/biotite ratios are close to 1 (Fig. 21), the element-mineral affinities of Neves (1997) are mirrored by the study data.

No partition coefficients were found from literature for elements B, Ge, Cd, and In. Thus, quality checks regarding these elements cannot be made, but it is implied, rather interestingly, that indium may be incorporated more readily (by an order of magnitude) in both amphibole and muscovite. Similarly, Be and Sc appear to be more compatible with amphibole than with biotite.

5.2. Comparison of biotite to previous studies

5.2.1. Framework for comparison

Based on the study dataset, it is indicated that the following trace element abundances increase in biotites with advancing fractionation (approximately I-type < S-type < A-type, Figs. 22 – 25): Li, B, Ga, Ge, Zr & Hf, Nb & Ta, In, Sn, and Pb. Co and Ni contents decrease in the same sequence, whereas Be and Zn show more complex behavior in that their concentrations are relatively high in the least and most fractionated samples. Moreover, the following "other" trace element correlations are implied (Figs. 26 – 30): (a) Li vs. Al, K, Nb & Ta, Ba, (b) Be vs. Na, Al, Sc, (c) Sc vs. Na, Ca, In, Sn, Nd, (d) Ge vs. Si, K, Ga, Nb, Pb, and (e) Nb vs. Ba.

These correlations and implications were compared to analogous *in situ* data from three recent papers: Berni et al. (2017), Breiter et al. (2017), and Michallik et al. (2017). To the best of author's knowledge, comprehensive studies on *in situ* trioctahedral mica trace element distributions (of contrasting granite types) are limited to one paper: Breiter et al. (2017), in which trioctahedral micas from Central European A-, S-, and I-type granitoids were analyzed. The study suggests that there are no major differences between "common" A-S-I-type granites with respect to biotite trace element distributions, although the more highly fractionated A- and S-type biotites are clearly more abundant in incompatible trace elements (Li, Ga, Ge, Nb, In, Sn, Ta; Sc decreases) compared to I-type biotites.

Compared to Breiter et al. (2017), the papers (and data) by Michallik et al. (2017) and

Berni et al. (2017) are more narrow in scope. Michallik et al. (2017) analyzed trioctahedral micas from the Luumäki pegmatite and associated granites, whereas Berni et al. (2017) analyzed trioctahedral micas from the Kymi pegmatite and associated granites. The Luumäki and Kymi pegmatites represent the late-stage fractionation (and hydrothermal) products of the Wiborg batholith, however, and since the main bulk of data from this study are associated with the earlier stages of Wiborg batholith evolution (A-type samples), data from Michallik et al. (2017) and Berni et al. (2017) were used to identify potential trends, similarities, or differences within the A-type biotites. However, it is noted that the data used from Michallik et al. (2017) represents the respective pegmatite host granite (wiborgite), whereas the data from Berni et al. (2017) represents the early and intermediary stages of the Kymi pegmatite intrusion (late-stage porphyritic and equigranular granites).

Furthermore, it is noted that the trace elements Li, Ga, Nb & Ta, and Sn were the only elements analyzed in all three reference studies. Be and B (+ Zn, Ba, Pb) were not analyzed by Breiter et al. (2017), whereas Sc, Ge, and In were not analyzed by Michallik et al. (2017), and REEs were not analyzed in any reference study. Zr and Hf were analyzed only by Michallik et al. (2017).

5.2.2. Comparison

When study data is juxtaposed with data from Berni et al. (2017), Breiter et al. (2017), and Michallik et al. (2017), three general trends become evident: **(1)** critical and other rare metal concentrations tend to increase with decreasing MgO content in biotites, **(2)** most of the "other" trace element correlations (a-e in *5.2.1.*) are likely spurious, and **(3)** there are, indeed, no clear differences between A- and S-type biotites (both types may contain high amounts of incompatible trace elements), but I-type biotites generally contain lower amounts of critical and rare metals.

With respect to **(1)**, critical and rare metals (or elements) Li, B, Be, Zr & Hf, and Nb & Ta plotted vs. MgO wt.% produce curvilinear trends akin to Figs. 22 – 25, whereas Sc, In, and Sn produce similar, but more scattered curvilinear trends (Fig. 32). For Sc and Ge, the trends resemble curvilinear correlation, but outliers imply that the correlations may be spurious. Zr and Hf plots are effectively unchanged. Thus, it is indicated that concentrations of Li, B, Be, Zr & Hf, Nb & Ta, In, Sn, and possibly Sc and Ge, increase

with progressing fractionation, which are in concert with most of related literature (e.g. Černý et al. 1985, Tischendorf et al. 2001, Van Lichtervelde et al. 2008, Zaraisky et al. 2009, Johan et al. 2012, Li et al. 2015, Xie et al. 2015, Simons et al. 2017).

As to **(2)**, the apparent "other" correlations (Figs. 26 – 30) exhibited in this study largely disappear when juxtaposed with the reference data. The exceptions to this rule are the correlations between (a) Li vs. Al, K, Ba, (b) Ge vs. K, Ga, Pb, and (c) Nb vs. Ba, out of which (a) Li vs. Ba and (c) Nb vs. Ba are effectively unchanged (in shape), whereas the other correlations plot distinctive trends (Fig. 33). Other weaker correlations, i.e. (e) Li vs. Nb, Ta, (f) Be vs. Al, Sc, and (g) Sc vs. In (Fig. 34) are more scattered compared to (a) – (c), but may exhibit broader trends. Moreover, an additional correlation (albeit weak) was identified between In and Zn (Fig. 35).

Implications from the more robust "other" correlations are: biotites may accommodate large quantities of Li starting at c. 10 – 11 wt.% Al and c. 8 wt.% K. Likewise, Ge fractionation may be monitored by interlayer K-cations, and Ge and Pb may be linearly correlated, or at least in the Wiborg batholith A-type granites. The ionic radii for $^{VI}Ge^{2+}$ and $^{VI}Pb^{4+}$ are 0.73 Å and 0.775 Å, respectively (Shannon 1976). Thus, it is speculated 'that Ge^{2+} and Pb^{4+} *might* substitute for e.g. 3 $^{VI}Mg^{2+}$ (0.72 Å), which is corroborated by the apparent increase in Ge and Pb contents with decreasing Mg abundances (Appendix 13: Figs. 2 and 4), although the absolute abundance variation between samples is generally low.

Extremely Li-enriched biotites appear to contain low amounts of Nb and Ta, which may be related to the fact that extremely Li-rich biotites tend to be associated with F-rich granites, and F-rich fluids may dissolve Nb and Ta (Timofeev et al. 2015, 2017, Breiter et al. 2017) into the liquid phase. Thus, Nb and Ta might have precipitated earlier or later than Li-rich biotites, and, as a result, extremely Li-rich biotites are poor in Nb and Ta.

Be tends to substitute for $(SiO_4)^{4-}$ as $(BeO_4)^{6-}$ (Taylor 1965), and since ^{IV}Al substitutes for ^{IV}Si (Johan et al. 2012), Be is likely correlated with Al through common affiliation. This is corroborated by the observation that Be tends to correlate negatively with ^{IV}Al (apfu) and positively with ^{VI}Al (apfu). The correlation between Be and Sc is more difficult to explain, but may be related to the their common affiliation with Ti^{4+} (Taylor 1965).

Relatively little is known about the geochemical characteristics of In (Cook et al. 2011, Valkama et al. 2016), but Sc and In may be expected to behave similarly (Taylor 1965), owing to their similar ionic radii and charges ($^{VI}Sc^{3+}$ 0.745 Å, $^{VI}In^{3+}$ 0.8 Å), which might be reflected in Fig. 34 E1. As for In and Zn (Fig. 35), they are often affiliated in sphalerite (Cook et al. 2011), which was identified as an accessory phase in A-type granites. The interplay between In and Zn might thus be reflected in coexisting biotites, although this hypothesis cannot be confirmed in the present study due to lack of accessory mineral data.

Concerning **(3)**, Figs. 32 – 34 illustrate rather well that there are no clear differences between highly fractionated A- and S-type biotite enrichment patterns, although indium appears to be more abundant in A-type biotites (Fig. 32 E), but not by a large margin (ca. 2 ppm). Nonetheless, I-type biotites are relatively depleted in comparison, owing to (in part) their higher Mg contents. Many critical and rare metals have a closer affinity to Fe than Mg, which is one factor, but clearly insufficient in explaining why I-type biotites are relatively depleted, and why there are no obvious differences between A- and S-type biotites.

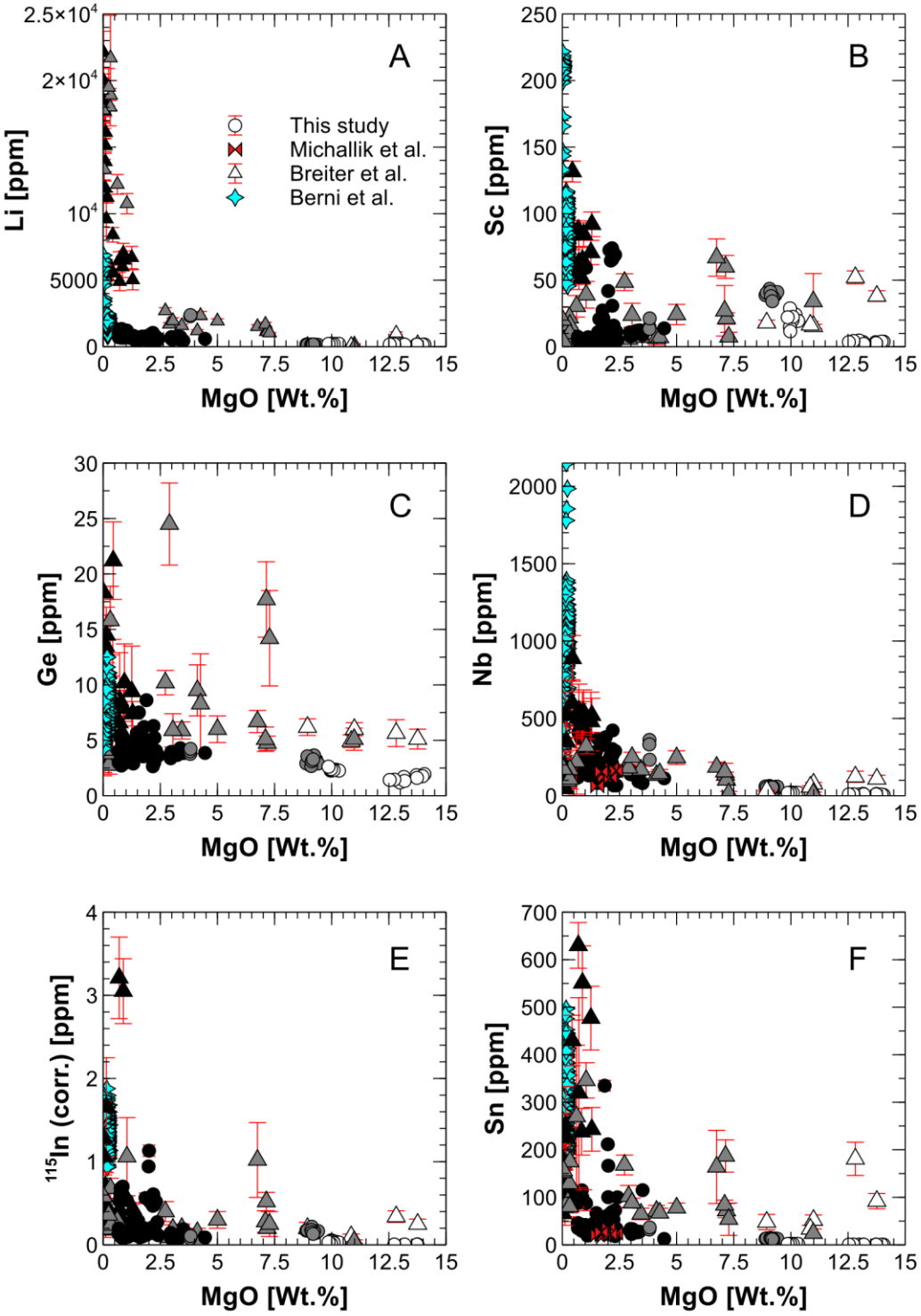

Figure 32. Biotite variation diagrams with MgO wt.% as the abscissa for (A) Li as an example of curvilinear correlation similar to Fig. 22, (B) Sc, (C) Ge, (D) Nb, (E) total In concentration calculated from mass 115 (corrected for spectral interferences), and (F) Sn. Symbol colors for A-, S-, and I-type biotites as in Fig. 22. Error bars for data from this study indicate a combined 1 σ of LA-ICP-MS transient signal noise and counting statistical errors, whereas error bars for data from Breiter et al. (2017) indicate one standard deviation from reported sample mean compositions.

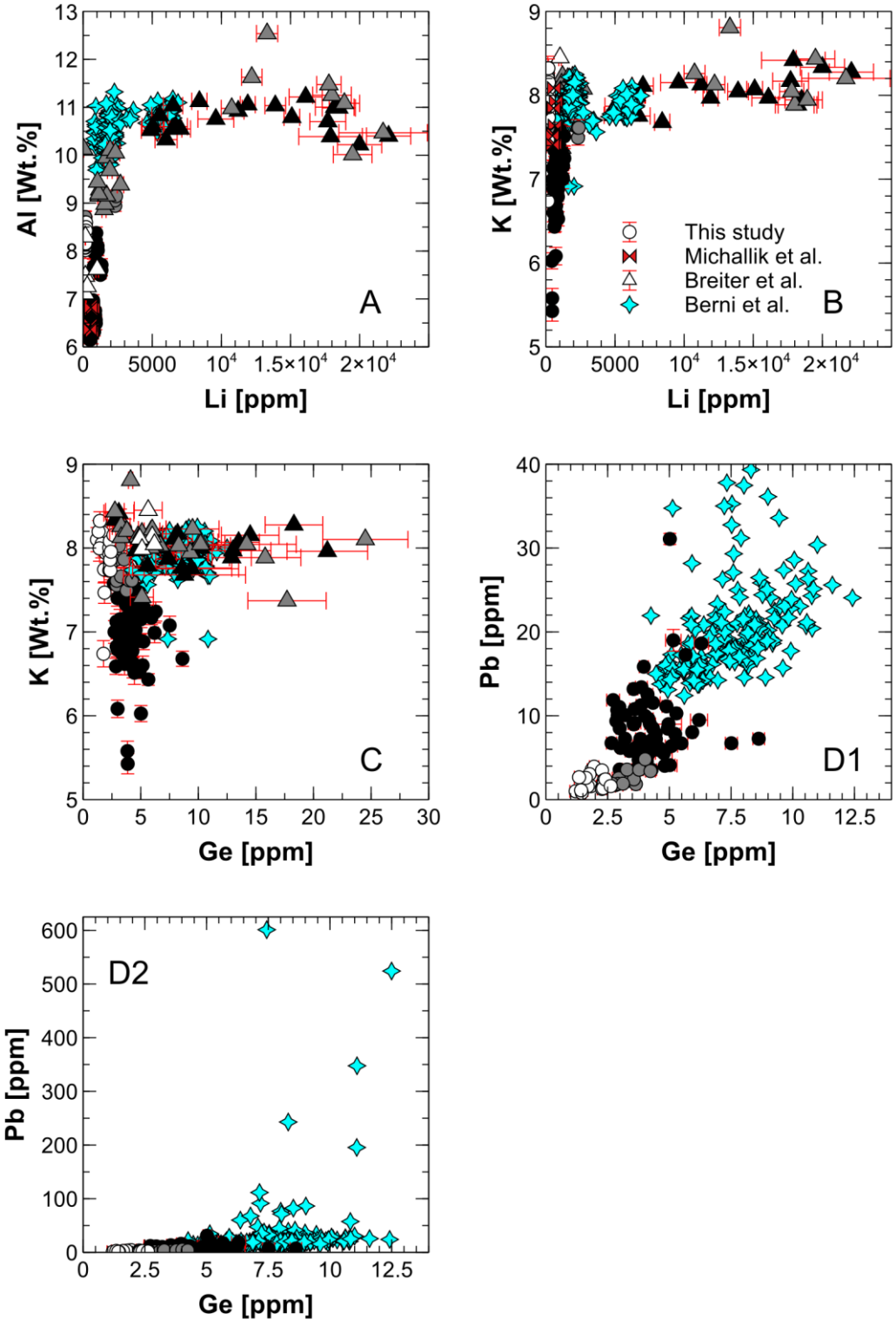

Figure 33. Biotite variation diagrams for (A) Al vs. Li, (B) K vs. Li, (C) K vs. Ge, (D1) Pb vs. Ge plotted without outliers, and (D2) Pb vs. Ge plotted with outliers. Symbology and error bars as in Fig. 32.

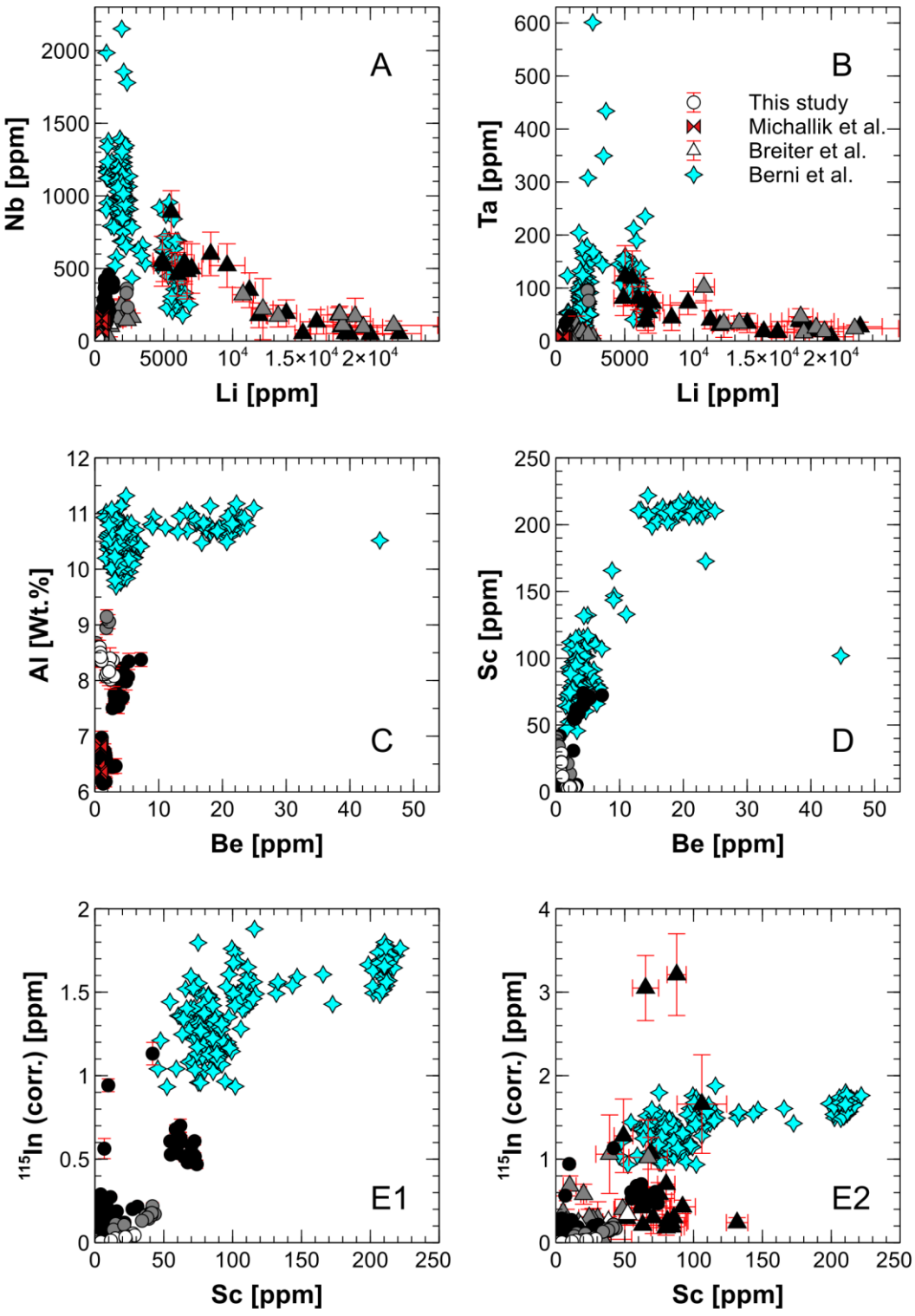

Figure 34. Biotite variation diagrams for (A) Nb vs. Li, (B) Ta vs. Li, (C) Al vs. Be, (D) Sc vs. Be, (E1) In vs. Sc plotted without data from Breiter et al. (2017), and (E2) In vs. Sc plotted with data from Breiter et al. (2017). "^{115}In (corr.) [ppm]" refers to the total In concentration calculated from mass 115 (corrected for spectral interferences). Symbology and error bars as in Fig. 32.

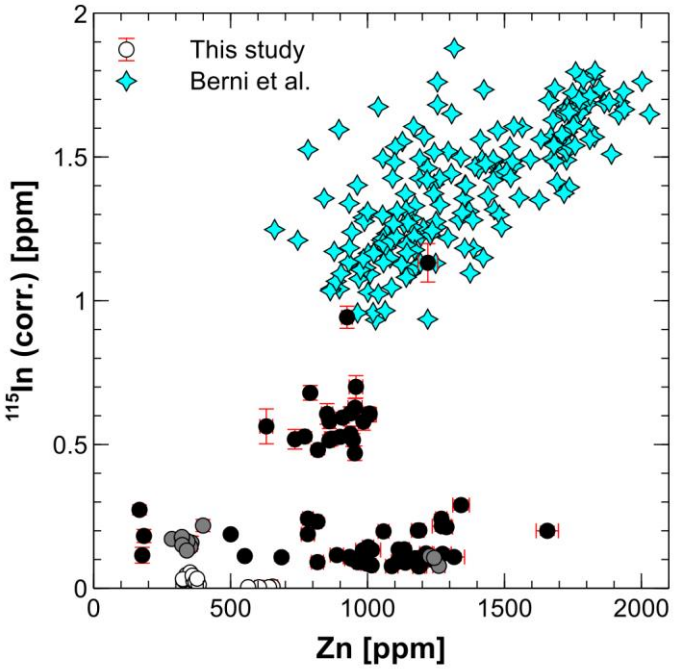

Figure 35. Biotite variation diagram for In vs. Zn. "115In (corr.) [ppm]" refers to the total In concentration calculated from mass 115 (corrected for spectral interferences). Symbology and error bars as in Fig. 32.

The dominant, and perhaps obvious, reason is that critical and rare metals simply do not concentrate and form (economic) deposits as a function of their parental magma composition *sensu stricto*. That is, economic deposits associated with granitoid magmatism are typically found in highly evolved, multi-stage pegmatite and greisen systems, which may be derived from any alphabet granite magma (S-I-A-M), given the right conditions during their magmatic evolution, metasomatic processes, or both (e.g. Chappell & White 2001, Černý et al. 2005). Pegmatites and greisenized deposits are typically affiliated with A- and S-type granites, however, since I-type (and M-) magmas tend to be more mafic and primitive, and thus require a more complex evolutionary path to produce critical and rare metal deposits. Nonetheless, it is no coincidence that the overwhelming majority of literature related to metalliferous granitoid deposits study (or specify) pegmatite intrusions and greisen deposits (e.g. Taylor 1965, Černý et al. 1985, Chappell & White 2001, Tischendorf et al. 2001, Van Lichtervelde et al. 2008, Pirajno 2009, Zaraisky et al. 2009, Johan et al. 2012, Roda-Robles et al. 2012, Xie et al. 2015, and all references therein) as sources of incompatible rare metals. Critical and rare metal concentrations do tend to increase with advancing fractionation (i.e. in residual melts) – but not because, but rather regardless of their magma source.

5.3. Evidence of metasomatism

Given the above considerations, why did the study data, then, indicate that A-type biotites contain more critical and rare metals? The likely explanation is two-fold: first, the number of samples is low, as discussed previously. Thus, there is a chance that correlations may be spurious, especially since S- and I-type granites are underrepresented relative to the A-type granites (2 I-type, 2 S-type vs. 6 A-type samples). Secondly, all sampled A-type granites show signs of metasomatism. The textural and mineralogical evidence of metasomatism in A-type samples include sericitic and saussuritic replacement textures (and minerals), myrmekite alteration (Fig. 36), and hematite accumulations (Fig. 37). Since elevated critical and rare metal concentrations are often affiliated with metasomatic processes, it is possible that the apparent (relatively) high trace metal concentrations are partly caused by metasomatism. The Sarvlaxviken bay area granites (LOV-1 to -4, Fig. 1) host multiple generations of greisenized Li-As-W-Zn-Mn-Cu-Pb-Sn-Mo-Bi-Be-In-bearing veins (Valkama et al. 2016), which could be reflected in the host rock biotite compositions. With respect to LOV-5 and -6, the alteration exhibited in them is not related to any known mineralization or deposit, and their genetic relationships with LOV-1 to -4 are unknown, but were likely deposited in the early stages of Wiborg batholith magmatism.

Be that as it may, the degree of metasomatic alteration in biotites is difficult to estimate because F or Cl were not analyzed, and the fluorine and chlorine contents in biotites are often used as a clues in assessing hydrothermal alteration (e.g. Johan et al. 2012, Li et al. 2015, Xie et al. 2015, Berni et al. 2017). The A-type samples host numerous relatively large fluorite inclusions which are coeval with ferromagnesian phases. This indicates that F was present in large quantities at some point during the system evolution, but whether this is reflected in biotite compositions is unknown.

Compositional zoning, which implies hydrothermal alteration, is characteristic to micas in highly fractionated granitoids (Li et al. 2015), although compositional zoning may also develop through magmatic processes. Nonetheless, these features can be identified with an electron microscope. BSE and SE imaging showed no signs of mica zoning apart from

a few exsolved grains in LOV-6. However, these grains were not analyzed. Indeed, mineral grains in this study were selected with the express intent of picking unaltered mineral grains. This implies that even though the bulk rock may be altered to some degree, the analyzed mineral grains should be relatively unaltered in comparison – but this does not prove that biotites did not exchange elements with a fluid phase, either. Ultimately, it is difficult to accurately prove or disprove the contribution of metasomatic processes to biotite chemistry, but it is possible that trace element fractionation in the A-type samples are not wholly due to magmatic processes.

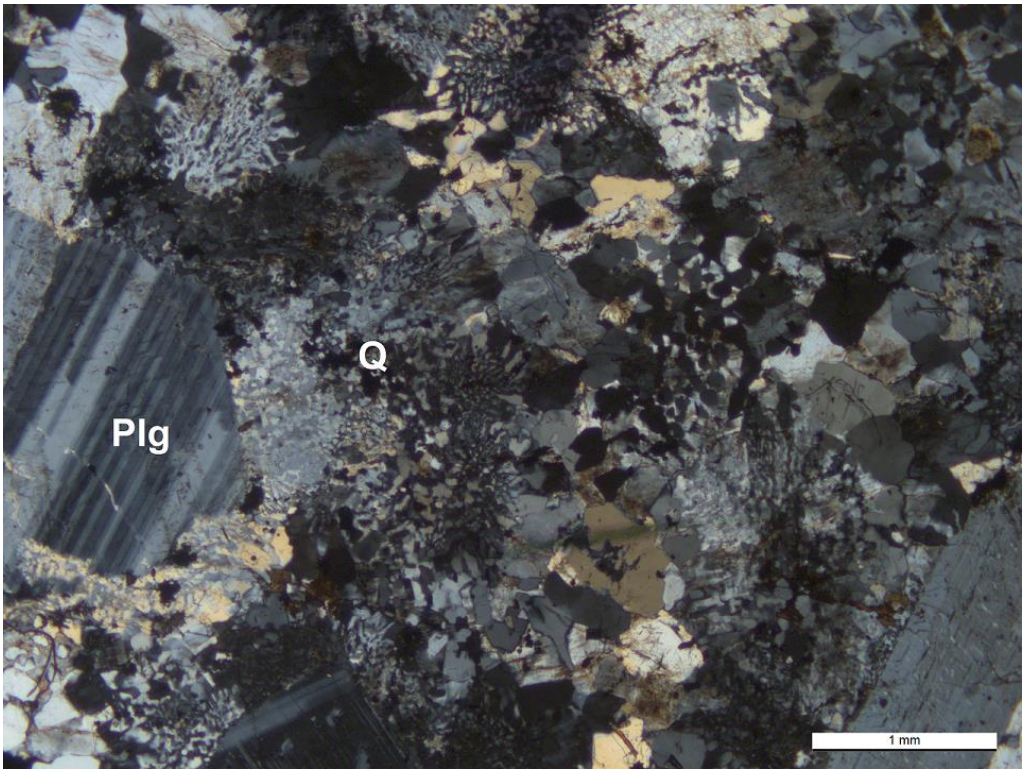

Figure 36. An example of extreme myrmekite alteration (in context of this study) from LOV-6. Cross-polarized view. Plg = Plagioclase; Q = quartz.

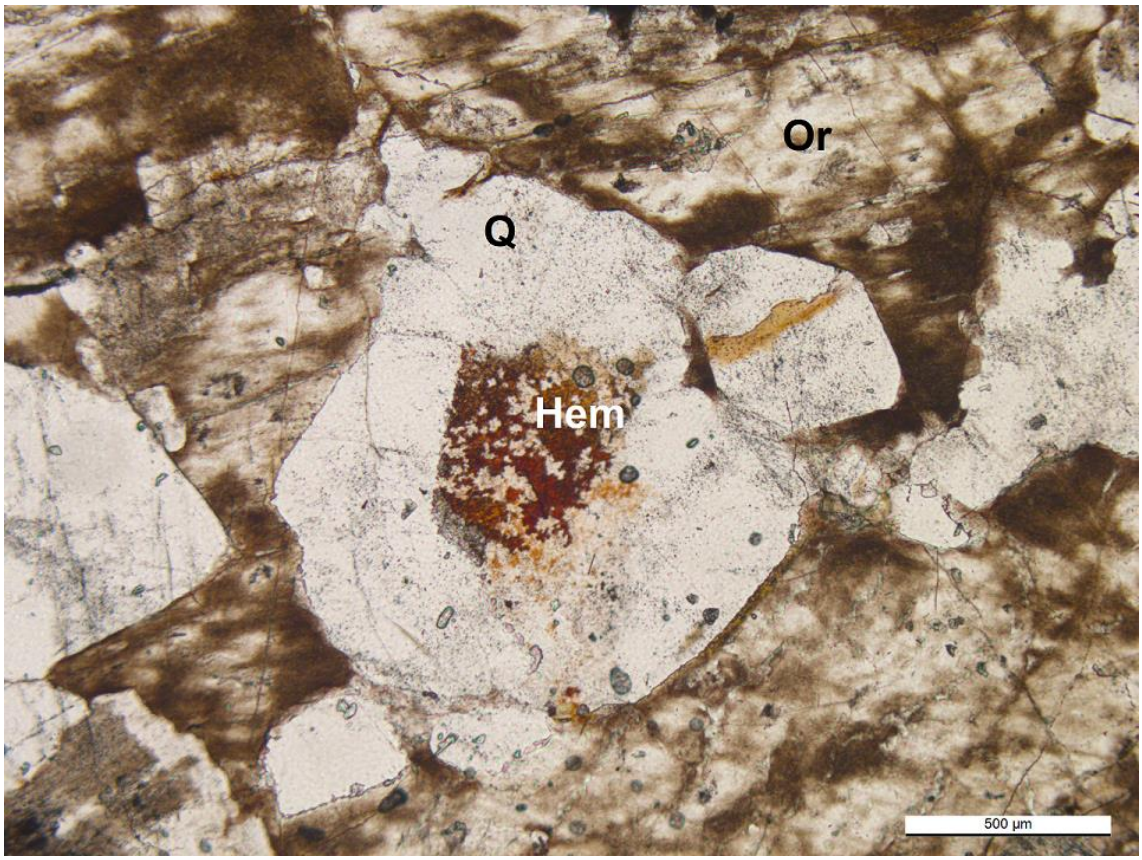

Figure 37. Hematite (Hem) accumulation in quartz (Q) surrounded by microperthitic orthoclase (Or). Plane-polarized view from LOV-4.

6. CONCLUSIONS

Based on comparing whole-rock data to *in situ* biotite data, biotite acts as a major host for Zn, and in most cases for Nb. Supplementing these findings with average granite trace element data from literature, it is indicated that biotite may act as a major host for Li, Co, Ge, Sn, and Ta, and in some cases for Sc and Ga as well. These trace elements may be concentrated by subsequent hydrothermal alteration which lets the biotite break down, forming ore vein deposits. Furthermore, it is indicated that Co abundances in trioctahedral micas decrease with advancing fractionation, which is linearly correlated with the Mg-content in biotites. That is, highly fractionated biotites are Mg-poor and also relatively depleted in Co. Conversely, relatively primitive and Mg-rich biotites contain high amounts of Co. Thus, Co may be used as fractionation indicator in LA-ICP-MS studies if major element data are unavailable.

Based on using Co as a fractionation indicator, it is implied that at levels below ca. 20 ppm Co, (significant) critical and rare element (Li, Be, B, Sc, Ga, Ge, Zr, Nb, Ta, In, Sn, in addition to Zn and Pb) enrichment may be expected to occur, hence Co could be used as an exploration tool. However, it is noted that the absolute abundances and differences between granite types in this study are often low (e.g. Be < 10 ppm), but the relative differences are distinctive. Nonetheless, juxtaposing the study data with that from literature, it is indicated that critical and other rare metals do indeed tend to concentrate with advancing fractionation, but independently from the magma source type (S-I-A-M). However, A- and S-type granites are often more fractionated than I- or M-type granites, and thus typically contain more critical metals in comparison.

Indium *may* have an affinity to A-type granites, but the current data is largely inconclusive in this respect. Moreover, it is indicated that indium and scandium fractionation may be correlated, in addition to Be & Al, and Be & Sc. Although the data on amphiboles and muscovites are very limited, it is indicated that amphiboles and muscovites incorporate Be, Sc, Zr, and In (and REEs for amphiboles) more readily than biotites by an order of magnitude or more. Since S-type granites (namely two-mica granites) appear to incorporate many critical (and specialty) metals in relatively high quantities, focusing future critical metal research on two-mica granite deposits might prove lucrative. Likewise, A-type granites may host significant In deposits, and amphibole minerals could prove a suitable petrogenetic indicators for In exploration.

As a final note, economic deposits of critical and rare metals are often associated with pegmatite and greisen deposits, which may be derived from all alphabet granites, although more commonly from S- and A-type granites. Thus, “common” granites are not expected to host significant critical metal deposits, unless they are affiliated with pegmatite intrusions or greisenization.

7. ACKNOWLEDGEMENTS

I wish to express my sincerest thanks and deepest gratitude to my supervisors Thomas Wagner, Tobias Fusswinkel, and Anselm Loges for all the help and guidance throughout this project, and for introducing me to this challenging subject. Moreover, I extend my gratitude (in no particular order) to Seija Kultti, Pasi Heikkilä, Henrik Kalliomäki, Radoslaw Michallik, Stefan Andersson, Aku Heinonen, Jussi Heinonen, Helena Korkka, the famous renaissance man Aleksi Aalto, my parents, and all who provided support and answers to my countless questions.

8. REFERENCES

Arth, J.G. 1976. Behaviour of trace elements during magmatic processes – a summary of theoretical models and their applications. Journal of Research of the U.S. Geological Survey, 4, 41-47.

Andersson, S.S., Wagner, T., Jonsson, E., and Michallik, R.M. 2018. Mineralogy, paragenesis and mineral chemistry of REE minerals in the Olserum-Djupedal REE-phosphate mineralization, SE Sweden. American Mineralogist, in press.

Bea, F., Pereira, M.D., and Stroh, A. 1994. Mineral/leucosome trace-element partitioning in a peraluminous migmatite (a laser ablation-ICP-MS study). Chemical Geology, 117, 291-312.

Berglund, M. and Wieser, M. 2011. Isotopic compositions of the elements 2009 (IUPAC Technical Report). Pure and Applied Chemistry, Vol. 83, 2, 397-410.

Berni, G.V., Wagner, T., Fusswinkel, T., and Wenzel, T. 2017. Magmatic-hydrothermal evolution of the Kymi topaz granite stock, SE Finland: Mineral chemistry evidence for episodic fluid exsolution. Lithos, 292-293, 401-423.

Blundy, J. and Wood, B. 2003. Partitioning of trace elements between crystals and melts. Earth and Planetary Science Letters, 210, 383-397.

Breiter, K., Vaňková, M., Galiová, M.V., Korbelová, Z., and Kanický, V. 2017. Lithium and trace-element concentrations in trioctahedral micas from granites of different geochemical types measured via laser ablation ICP-MS. Mineralogical Magazine, Vol. 81 (1), 15-33.

Carr, M.H. and Turekian, K.K. 1961. The geochemistry of cobalt. Geochimica et Cosmochimica Acta, Vol. 23, 9-60.

Černý, P., Blevin, P.L., Cuney, M., and London, D. 2005. Granite-Related Ore Deposits. In: Hedenquist, J.W., Thompson, J.F.H., Goldfarb, R.J., and Richards, J.P. (eds), Economic Geology 100th Anniversary Volume, 337-370.

Černý, P., Meintzer, R.E., and Anderson, A.J. 1985. Extreme fractionation in rare-element granitic pegmatites: selected examples of data and mechanisms. Canadian Mineralogist, Vol. 23, 381-421.

Chappell, B.W. and White, A.J.R. 2001. Two contrasting granite types: 25 years later. Australian Journal of Earth Sciences, 48, 489-499.

Cook, N.J., Sundblad, K., Valkama, M., Nygård, R., Ciobanu, C.L., and Danyushevsky, L. 2011. Indium mineralization in A-type granites in southeastern Finland: Insights into mineralogy and partitioning between coexisting minerals. Chemical Geology, 284, 62-73.

Deer, W.A., Howie, R.A., and Zussman, J. 1992. An Introduction to the Rock-Forming Minerals. 2nd edition. Longman Scientific & Technical, London, 696.

European Commission. 2015. Report on Critical Raw Materials for the EU – Critical Raw Materials Profiles.

Frost, B.R., Barnes, C.G., Collins, W.J., Arculus, R.J., Ellis, D.J., and Frost, C.D. 2001. A Geochemical Classification for Granitic Rocks. Journal of Petrology, Vol. 42, 2033-2048.

Fryer, B.J., Jackson, S.E., and Longerich, H.P. 1995. The design, operation and role of the laser-ablation microprobe coupled with an inductively coupled plasma-mass spectrometer (LAM-ICP-MS) in the earth sciences. The Canadian Mineralogist, Vol. 33, 303-312.

Geological Survey of Finland. 2017. Spatial data products. Page visited 10.11.2017. <https://hakku.gtk.fi/en/locations/search>

Geological Survey of Sweden. 2017. SGU map viewer. Page visited 10.11.2017. <https://apps.sgu.se/kartvisare/index-en.html>

Guillong, M., Meier, D., Murray, A., Heinrich, C., and Yardley, B. 2008. Appendix A6; SILLS; a MATLAB-based program for the reduction of laser ablation ICP-MS data of homogeneous materials and inclusions. Short Course Series – Mineralogical Association of Canada 40, 328-333.

Haapala, I. 1995. Metallogeny of the Rapakivi Granites. Mineralogy and Petrology, 54, 149-160.

Hawthorne, F.C., Oberti, R., Harlow, G.E., Maresch, W.V., Martin, R.F., Schumacher, J.C., and Welch, M.D. 2012. IMA report, nomenclature of the amphibole supergroup. American Mineralogist, Vol. 97, 2031-2048.

Icenhower, J. and London, D. 1995. An experimental study of element partitioning among biotite, muscovite, and coexisting peraluminous silicic melt at 200 MPa (H_2O). American Mineralogist, Vol. 80, 1229-1251.

Janoušek, V., Farrow, C.M., and Erban, V. 2006. Interpretation of whole-rock geochemical data in igneous geochemistry: introducing Geochemical Data Toolkit (GCDkit). Journal of Petrology, Vol. 47, 1255-1259.

Johan, Z., Strnad, L., and Johan, V. 2012. Evolution of the Cínovec (Zinnwald) granite cupola, Czech Republic: composition of feldspars and micas, a clue to the origin of W, Sn mineralization. The Canadian Mineralogist, Vol. 50, 1131-1148.

Kleinhanns, L.C., Fischer-Gödde, M, and Hansen, B.T. 2012. Sr-Nd isotope and geochemical characterization of the Paleoproterozoic Västervik formation (Baltic Shield, SE-Sweden): a southerly exposure of Svecofennian metasiliciclastic sediments. International Journal of Earth Sciences, 101, 39-55.

Kleinhanns, L.C., Whitehouse, M.J., Nolte, N., Baero, W., Wilsky, F., Hansen, B.T., and Schoenberg, R. 2015. Mode and timing of granitoid magmatism in the Västervik area (SE Sweden, Baltic Shield): Sr-Nd isotope and SIMS U-Pb age constraints. Lithos, 212-215, 321-337.

Li, J., Huang, X-L., He, P-L., Li, W-X., Yu, Y., and Chen, L. 2015. In situ analyses of micas in the Yashan granite, South China: Constraints on magmatic and hydrothermal evolutions of W and Ta-Nb bearing granites. Ore Geology Reviews, Vol. 65, 793-810.

Locock, A.J. 2014. An Excel spreadsheet to classify chemical analyses of amphiboles following the IMA 2012 recommendations. Computers & Geosciences, Vol. 62, 1-11.

Michallik, R.M., Wagner, T., Fusswinkel, T., Heinonen, J.S., and Heikkilä, P. 2017. Chemical evolution and origin of the Luumäki gem beryl pegmatite: constraints from mineral trace element chemistry and fractionation modeling. Lithos, 274-275, 147-168.

Moss, R.L., Tzimas, E., Kara, H., Willis, P., and Kooroshy, J. 2011. Critical Metals in Strategic Energy Technologies – Assessing Rare Metals as Supply-Chain Bottlenecks in Low-Carbon Energy Technologies. Institute for Energy and Transport, European Commission, Luxembourg.

Neves, L.J.P.F. 1997. Trace element content and partitioning between biotite and muscovite of granitic rocks: a study in the Viseu region (Central Portugal). European Journal of Mineralogy, Vol. 9, 849-857.

Nolte, N., Kleinhanns, I.C., Baero, W. and Hansen, B.T. 2011. Petrography and whole-rock geochemical characteristics of Västervik granitoids to syenitoids, southeast Sweden: constraints on petrogenesis and tectonic setting at the southern margin of the Svecofennian domain. GFF, 133: 3-4, 173-196.

O'Brien, H.E., Nurmi, P.A., and Karhu, J.A. 1993. Oxygen, hydrogen and strontium isotopic compositions of gold mineralization in the late archean Hattu schist belt, Ilomantsi, Eastern Finland. In: Nurmi, P.A., Sorjonen-Ward, P. (Eds.) Geological Development, Gold Mineralisation and Exploration Methods in the Late Archaean Hattu Schist Belt, Ilomantsi, Eastern Finland. Geological Survey of Finland, Special Paper 17, pp. 291-306.

Pearce, J.A., Harris, N.B.W., and Tindle, A.G. 1984. Trace Element Discrimination Diagrams for the Tectonic Interpretation of Granitic Rocks. Journal of Petrology, Vol. 25, 956-983.

Pirajno, F. 2009. Hydrothermal Processes and Mineral Systems. Springer, Netherlands, 1250 p.

Ranta, E. 2017. Fluid-rock reactions in the carbonatites of the Grønnedal-Íka alkaline complex, South Greenland. MSc. Thesis, University of Helsinki, Faculty of Science, Department of Geosciences and Geography, 61 p.

Reed, G.C. 2013. Amended and restated techinal report for Olserum REE deposit, southern Sweden. Tasman Metals, Vancouver, 85 p.

Rieder, M., Cavazzini, G., Dyakonov, Y.S., Frank-Kamenetskii, V.A., Gottardi, G., Guggenheim, S., Koval, P.V., Mueller, G., Neiva, A.M.R., Radoslovich, E.W., Robert, J.L., Sassi, F.P., Takeda, H., Weiss, Z., and Wones, D.R. 1998. Nomenclature of the micas. The Canadian

Mineralogist, Vol. 36, 905-912.
Rock, N.M.S., Webb, J.A., McNaughton, N.J., and Bell, G.D. 1987. Nonparametric estimation of averages and errors for small data-sets in isotope geoscience: a proposal. In: New Developments and Applications in Isotope Geoscience. Chemical Geology (Isotope Geoscience Section), 66, pp. 163-177.
Rock, N.M.S. 1988. Summary Statistics in Geochemistry: A Study of the Performance of Robust Estimates. Mathematical Geology, Vol. 20, No. 3, pp 243-275.
Roda-Robles, E., Pesquera, A., Gil-Grespo, P., Torres-Ruiz, J. 2012. From granite to highly evolved pegmatite: A case study of the Pinilla de Fermoselle granite-pegmatite system (Zamora, Spain). Lithos, 153, 192-207.
Rollinson, H.R. 1993. Using Geochemical Data: Evaluation, Presentation, Interpretation. Longman, Essex, 352 p.
Rämö, O.T. and Haapala, I. 2005. Rapakivi granites. In: Lehtinen, M., Nurmi, P.A., and Rämö, O.T. (eds). Precambrian Geology of Finland – Key to the Evolution of the Fennoscandian Shield. Developments in Precambrian Geology, Vol. 14, 533-566.
Shannon, R.D. 1976. Revised Effective Ionic Radii and Systematic Studies of Interatomic Distances in Halides and Chalcogenides. Acta Crystallographica, A32, 751-767.
Simons, B., Andersen, J.C.Ø., Shail, R.K., and Jenner, F.E. 2017. Fractionation of Li, Be, Ga, Nb, Ta, In, Sn, Sb, W and Bi in the peraluminous Early Permian Variscan granites of the Cornubian Batholith: Precursor processes to magmatic-hydrothermal mineralisation. Lithos, 278-281, 491-512.
Sorjonen-Ward. P. 1993. An overview of structural evolution and lithic units within and intruding the late Archaean Hattu schist belt, Ilomantsi, eastern Finland. In: Nurmi, P.A., Sorjonen-Ward, P. (Eds.) Geological Development, Gold Mineralisation and Exploration Methods in the Late Archaean Hattu Schist Belt, Ilomantsi, Eastern Finland. Geological Survey of Finland, Special Paper 17, pp. 9-102.
Sorjonen-Ward, P., Hartikainen, A., Nurmi, P.A., Rasilainen, K., Schaubs, P., Zhang, Y. and Liikanen, J. 2015. Exploration targeting and geological context of gold mineralisation in the Neoarchean Ilomantsi greenstone belt in eastern Finland. In: Maier, W.D., Lahtinen, R., O'Brien, H. (Eds.), Mineral Deposits of Finland, Elsevier, pp. 435-466.
Streckeisen, A. 1974. Classification and nomenclature of plutonic rocks recommendations of the IUGS subcommission on the systematics of Igneous Rocks. Geologische Rundschau, Vol. 63, 773-786.
Taylor, S.R. 1965. The application of trace element data to problems in petrology. Physics and Chemistry of the Earth, Vol. 6, 133-213.
Thomas, R. 2013. Chapter 14: Review of Interferences. In: Practical Guide to ICP-MS: A Tutorial for Beginners. 3rd edition. CRC Press, Boca Raton, 133-142.
Timofeev, A., Migdisov, A.A., and Williams-Jones, A.E. 2015. An experimental study of the solubility and speciation of niobium in fluoride-bearing aqueous solutions at elevated temperature. Geochimica et Cosmochimica Acta, 158, 103-111.
Timofeev, A., Migdisov, A.A., and Williams-Jones, A.E. 2017. An experimental study of the solubility and speciation of tantalum in fluoride-bearing aqueous solutions at elevated temperature. Geochimica et Cosmochimica Acta, 197, 294-304.
Tischendorf, G., Gottesmann, B., Förster, H.-J., and Trumbull, R.B. 1997. On Li-bearing micas: estimating Li from electron microprobe analyses and an improved diagram for graphical representation. Mineralogical Magazine, Vol. 61, 809-834.
Tischendorf, G., Förster, H.-J., and Gottesmann, B. 2001. Minor- and trace-element composition of trioctahedral micas: a review. Mineralogical Magazine, Vol. 65, 249-276.
Turekian, K. K. and Wedepohl, K.H. 1961. Distribution of the Elements in Some Major Units of the Earth's Crust. Geological Society of America Bulletin, Vol. 72, 175-192.
Vaasjoki, M., Rämö, O. T. and Sakko, M. 1991. New U-Pb ages from the Wiborg rapakivi area: constraints on the temporal evolution of the rapakivi granite-anorthosite-diabase dyke association of southeastern Finland. Precambrian Res. 51, pp. 227-243.
Vaasjoki, M., Sorjonen-Ward, P. and Lavikainen, S. 1993. U-Pb age determination and sulphide Pb-Pb characteristics from the late Archaean Hattu schist belt, Ilomantsi, eastern Finland. In:

Nurmi, P.A., Sorjonen-Ward, P. (Eds.), Geological Development, Gold Mineralisation and Exploration Methods in the Late Archaean Hattu Schist Belt, Ilomantsi, Eastern Finland. Geological Survey of Finland, Special Paper 17, pp. 103-132.

Valkama, M., Sundbland, K., Nygård, R., and Cook, N. 2016. Mineralogy and geochemistry of indium-bearing polymetallic veins in the Sarvlaxviken area, Lovisa, Finland. Ore Geology Reviews, 75, 206-219.

Van Lichtervelde, M., Grégoire, M., Linnen, R.L., Béziat, D., and Salvi, S. 2008. Trace element geochemistry by laser ablation ICP-MS of micas associated with Ta mineralization in the Tanco pegmatite, Manitoba, Canada. Contribution to Mineralogy and Petrology, 155, 791-806.

Whalen, J.B., Currie, K.L., and Chappell, B.W. 1987. A-type granites: geochemical characteristics, discrimination and petrogenesis. Contributions to Mineralogy and Petrology, 95, 407-419.

Xie, L., Wang, R.C., Groat, L.A., Zhu, J.C., Huang, F.F., and Cempírek, J. 2015. A combined EMPA and LA-ICP-MS study of Li-bearing mica and Sn-Ti oxide minerals from the Qiguling topaz rhyolite (Qitianling District, China): The role of fluorine in origin of tin mineralization. Ore Geology Reviews, Vol. 65, 779-792.

Zaraisky, G.P., Aksyuk. A.M., Devyatova, V.N., Udoratina, O.V., and Chevychelov, V.Yu. 2009. The Zr/Hf Ratio as a Fractionation Indicator of Rare-Metal Granites. Petrology, Vol. 17, 25-45.

9. APPENDICES

APPENDIX 1

Table A. EPMA biotite, sanidine, and diopside standards of known composition measured as unknowns.

	07 Bt STD (known) wt.%	41 Snd STD (known) wt.%	21 Diopside STD (known) wt.%	07 Bt STD (unknown) wt.%	41 Snd STD (unknown) wt.%	21 Diopside STD (unknown) wt.%
SiO_2	38.72	64.67	55.37	36.88	64.97	55.78
TiO_2	1.77	na	0.08	0.98	b.d.	b.d.
Al_2O_3	15.13	18.76	0.09	14.33	18.10	b.d.
FeO	10.72	0.18	0.05	10.30	b.d.	b.d.
MgO	19.52	na	18.62	18.74	b.d.	18.42
CaO	0.1	na	25.73	b.d.	b.d.	25.02
Na_2O	na	3.01	na	0.09	2.94	b.d.
K_2O	9.91	12.11	na	9.76	12.07	b.d.

na = not analyzed; b.d. = below detection limit at a 95% confidence interval.

Table B. EPMA wt.% ratios of measured standard compositions to known standard compositions multiplied by 100 %.

	07 Bt STD (unknown)/(known)	41 Snd STD (unknown)/(known)	21 Diopside STD (unknown)/(known)
SiO_2	95.24	100.47	100.74
TiO_2	55.10	na	na
Al_2O_3	94.68	96.46	na
FeO	96.05	na	na
MgO	96.00	na	98.93
CaO	na	na	97.22
Na_2O	na	97.69	na
K_2O	98.52	99.66	na

na = not applicable.

APPENDIX 2

Table A. Results for duplicate EPMA analyses. Major oxide element data expressed as wt.%.

(continued)	Sample/spot no.	SiO_2	TiO_2	Al_2O_3	FeO	MgO	CaO	Na_2O	K_2O
Grain 2	LOV-1/3	33.83	3.02	12.19	35.62	1.85	0.46	b.d.	8.10
	LOV-1/4	33.48	2.92	12.13	34.74	1.99	0.19	b.d.	7.65
	LOV-1/5	33.78	3.11	12.34	34.64	1.85	0.18	b.d.	8.52
Grain 3	LOV-1/6	34.07	2.56	12.18	35.36	1.99	b.d.	b.d.	8.24
	LOV-1/7	34.00	3.08	12.09	34.72	1.90	b.d.	b.d.	8.57
	LOV-1/8	33.82	3.07	11.91	33.35	1.97	b.d.	0.11	8.18
Grain 2	LOV-2.1/2	39.75	1.44	8.52	30.83	1.94	9.81	1.76	1.48
	LOV-2.1/3	39.38	1.43	8.58	30.60	1.99	10.14	1.85	1.53
	LOV-2.1/4	39.05	1.56	8.60	30.21	1.65	10.09	1.65	1.53
Grain 1	LOV-4/1	34.91	2.59	15.38	32.68	2.23	b.d.	0.14	8.36
	LOV-4/2	34.50	2.52	15.83	33.38	2.19	b.d.	0.17	8.53
	LOV-4/3	33.44	2.39	15.06	33.03	2.05	b.d.	0.10	8.11
Grain 2	LOV-4/4	34.30	2.92	15.32	32.23	2.17	b.d.	0.13	8.43
	LOV-4/5	35.76	2.71	14.60	31.07	2.44	b.d.	b.d.	8.81
	LOV-4/6	34.91	2.29	14.90	30.78	2.26	b.d.	0.13	8.33
Grain 3	LOV-4/7	33.97	2.43	15.53	32.57	2.06	b.d.	b.d.	8.36
	LOV-4/8	34.15	1.90	15.37	32.33	2.08	b.d.	b.d.	8.31
	LOV-4/9	35.06	1.89	15.03	31.35	2.26	b.d.	b.d.	8.13
Grain 5	LOV-4/11	34.61	2.08	15.77	32.61	2.20	b.d.	0.14	8.54
	LOV-4/12	35.01	2.35	15.61	31.41	2.21	0.09	b.d.	8.66
	LOV-4/13	36.09	2.21	15.15	31.12	2.50	b.d.	b.d.	8.90
Grain 9	LOV-4/17	35.45	2.77	15.16	31.94	2.26	b.d.	0.11	8.59
	LOV-4/18	35.43	2.74	15.08	31.11	2.31	b.d.	0.13	8.81
	LOV-4/19	35.51	2.57	15.00	31.31	2.27	b.d.	b.d.	8.57
	LOV-4/20	35.35	2.46	14.79	31.03	2.28	b.d.	b.d.	8.73
Grain 10	LOV-4/21	35.59	2.61	14.85	31.14	2.27	b.d.	0.11	8.88

(continued)	Sample/spot no.	SiO_2	TiO_2	Al_2O_3	FeO	MgO	CaO	Na_2O	K_2O
	LOV-4/22	35.62	2.74	14.73	30.90	2.26	b.d.	0.13	8.87
	LOV-4/23	35.05	2.26	15.25	32.08	2.20	b.d.	0.11	8.74
Grain 4	LOV-5/4	33.21	2.14	12.69	36.67	1.64	b.d.	b.d.	7.93
	LOV-5/5	33.03	2.37	12.65	36.97	1.47	b.d.	b.d.	7.93
	LOV-5/6	33.64	1.81	12.66	36.22	1.80	b.d.	b.d.	7.71
	LOV-5/7	33.83	3.75	12.42	36.13	1.57	b.d.	0.17	8.28
	LOV-5/8	33.72	3.24	12.28	35.14	1.61	b.d.	b.d.	8.06
Grain 7	LOV-5/11	33.41	2.44	12.38	35.75	1.41	b.d.	b.d.	7.90
	LOV-5/12	33.26	2.18	12.29	35.88	1.47	b.d.	b.d.	8.23
	LOV-5/13	33.03	2.07	12.65	36.83	1.43	b.d.	b.d.	7.89
Grain 2	LOV-6.1/2	32.98	2.66	12.76	37.36	1.26	0.12	b.d.	7.98
	LOV-6.1/3	32.69	3.04	12.35	35.96	0.88	0.09	b.d.	8.06
	LOV-6.1/4	33.56	3.80	12.72	35.56	1.13	b.d.	0.13	8.44
Grain 4	LOV-6.1/6	32.78	3.01	12.34	36.70	0.78	0.10	b.d.	7.86
	LOV-6.1/7	32.88	3.36	12.50	37.08	0.79	b.d.	b.d.	8.12
	LOV-6.1/8	32.82	2.94	12.37	36.55	0.77	0.08	b.d.	8.01
Grain 6	LOV-6.1/10	33.31	2.90	12.41	37.75	1.10	b.d.	0.12	8.08
	LOV-6.1/11	33.63	2.23	12.59	37.98	1.11	b.d.	0.13	7.90
	LOV-6.1/12	33.30	2.85	12.46	36.97	1.16	0.09	0.19	7.79
	LOV-6.1/13	33.34	3.03	12.38	36.47	1.43	b.d.	0.14	8.01
Grain 1	VIG-1/1	37.02	0.92	15.36	16.79	14.13	b.d.	b.d.	8.55
	VIG-1/2	37.97	1.24	15.36	16.46	13.71	b.d.	b.d.	9.40
	VIG-1/3	37.55	1.47	15.15	16.34	13.75	b.d.	b.d.	9.72
Grain 2	VIG-1/4	37.09	1.36	15.24	16.37	12.71	0.32	b.d.	9.08
	VIG-1/5	37.88	1.04	15.35	15.42	12.93	0.24	0.11	9.19
	VIG-1/6	37.31	1.27	15.26	15.73	13.16	0.21	b.d.	9.17
Grain 3	VIG-1/7	36.59	0.65	15.66	16.30	14.22	0.21	b.d.	8.02
	VIG-1/8	36.31	0.92	15.62	16.35	14.49	0.18	b.d.	7.82
	VIG-1/9	37.32	0.72	15.80	16.45	13.71	0.23	b.d.	8.41
Grain 4	VIG-1/10	36.85	0.66	15.58	15.76	14.08	0.15	b.d.	7.79
	VIG-1/11	37.30	0.83	15.78	16.05	14.06	0.22	b.d.	8.19

(continued)	Sample/spot no.	SiO_2	TiO_2	Al_2O_3	FeO	MgO	CaO	Na_2O	K_2O
Grain 5	VIG-1/12	37.09	0.82	15.39	15.71	13.56	0.22	b.d.	8.17
	VIG-1/13	37.40	1.26	15.35	16.86	12.91	b.d.	b.d.	9.31
	VIG-1/14	37.64	1.22	15.25	17.06	12.98	b.d.	b.d.	9.43
	VIG-1/15	36.99	0.93	15.30	16.60	12.81	b.d.	b.d.	8.93
Grain 6	VIG-1/16	35.08	1.53	15.25	17.15	14.31	b.d.	b.d.	7.01
	VIG-1/17	35.11	1.70	15.56	16.38	14.73	0.14	b.d.	6.67
	VIG-1/18	36.06	1.24	15.27	16.91	13.97	0.12	b.d.	7.61
Grain 7	VIG-1/19	37.35	1.30	15.87	16.63	13.73	b.d.	b.d.	8.50
	VIG-1/20	37.08	1.22	15.71	16.31	14.20	b.d.	b.d.	8.49
	VIG-1/21	37.66	1.23	15.69	16.12	13.32	b.d.	b.d.	8.76
Grain 8	VIG-1/22	37.33	1.15	15.38	16.00	13.19	b.d.	b.d.	9.03
	VIG-1/23	36.93	1.23	15.39	16.18	13.86	b.d.	b.d.	8.60
	VIG-1/24	37.65	1.11	15.58	15.83	13.11	b.d.	b.d.	9.14
Grain 9	VIG-1/25	37.67	1.56	15.40	17.17	12.81	b.d.	b.d.	9.44
	VIG-1/26	37.99	1.60	15.55	17.41	12.74	b.d.	b.d.	9.70
	VIG-1/27	37.98	1.52	15.61	17.02	12.93	b.d.	0.09	9.34
Grain 10	VIG-1/28	37.77	1.19	15.57	16.39	12.66	b.d.	0.11	9.42
	VIG-1/29	37.53	1.50	15.42	16.78	12.54	b.d.	b.d.	9.51
	VIG-1/30	37.76	1.32	15.47	16.41	13.15	b.d.	b.d.	9.02

b.d. = below detection limit at a 95 % confidence interval.

APPENDIX 3

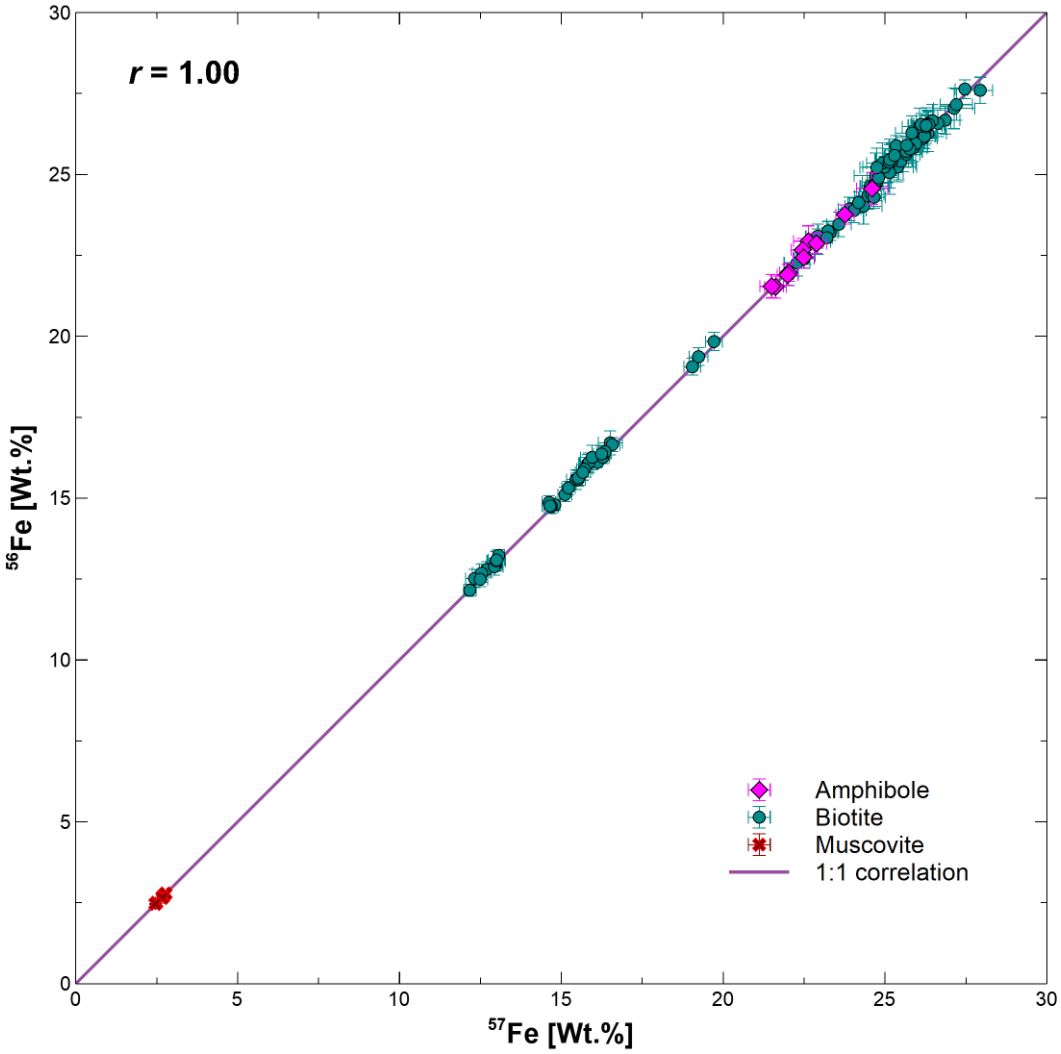

Figure 1. Fe masses 57 vs. 56 analyzed by LA-ICP-MS. Error bars indicate a combined 1 σ of LA-ICP-MS transient signal noise and counting statistical errors.

APPENDIX 4

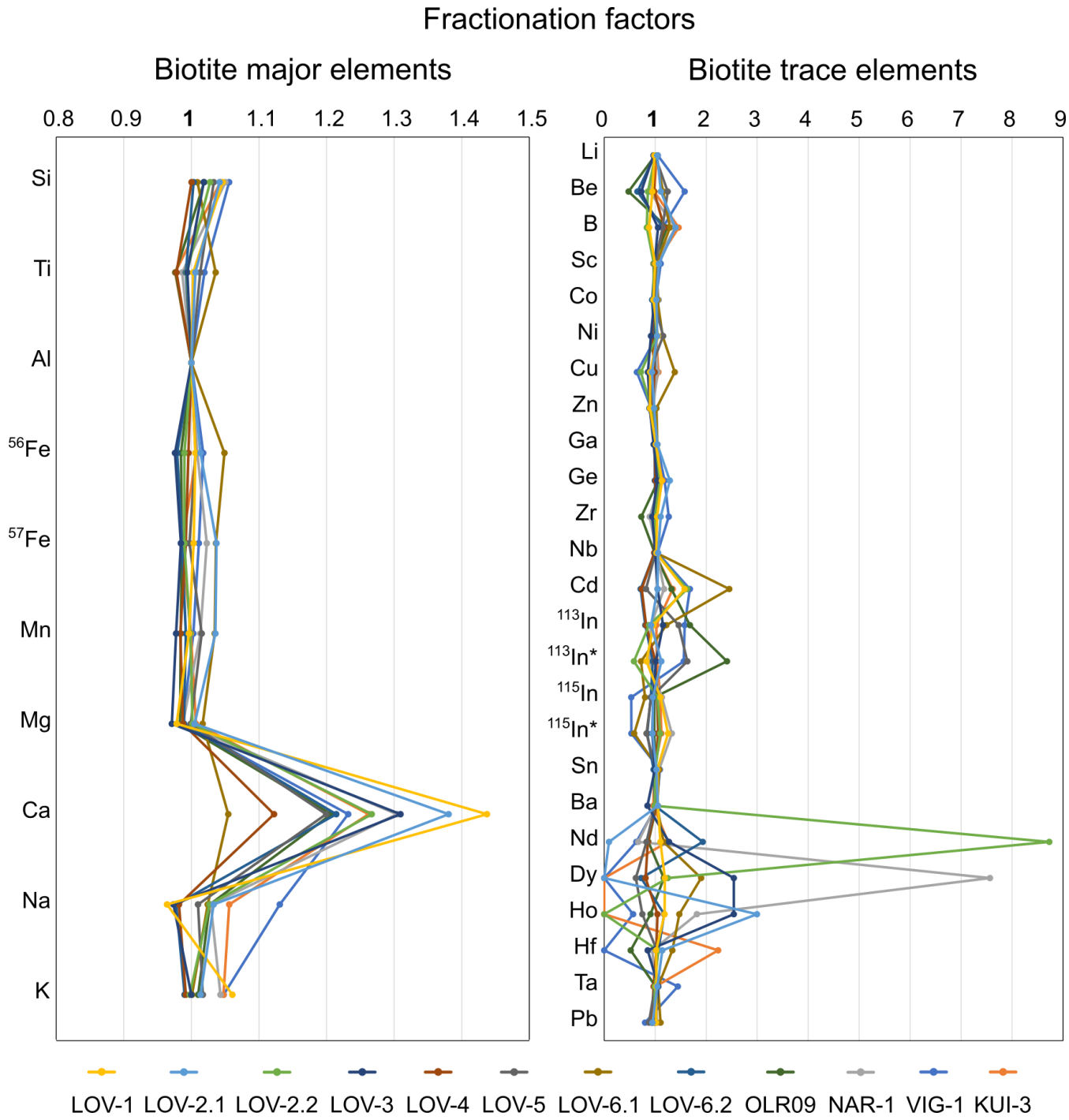

Figure 1. Calculated fractionation factors for selected biotite samples. Note the different scales for major and trace elements. Asterisk (*) refers to elements corrected for isobaric interferences, whereas "^{113}In" and "^{115}In" refer to the total In concentrations calculated from masses 113 and 115, respectively. Fractionation factors were calculated with in-house software based on Fryer et al. (1995).

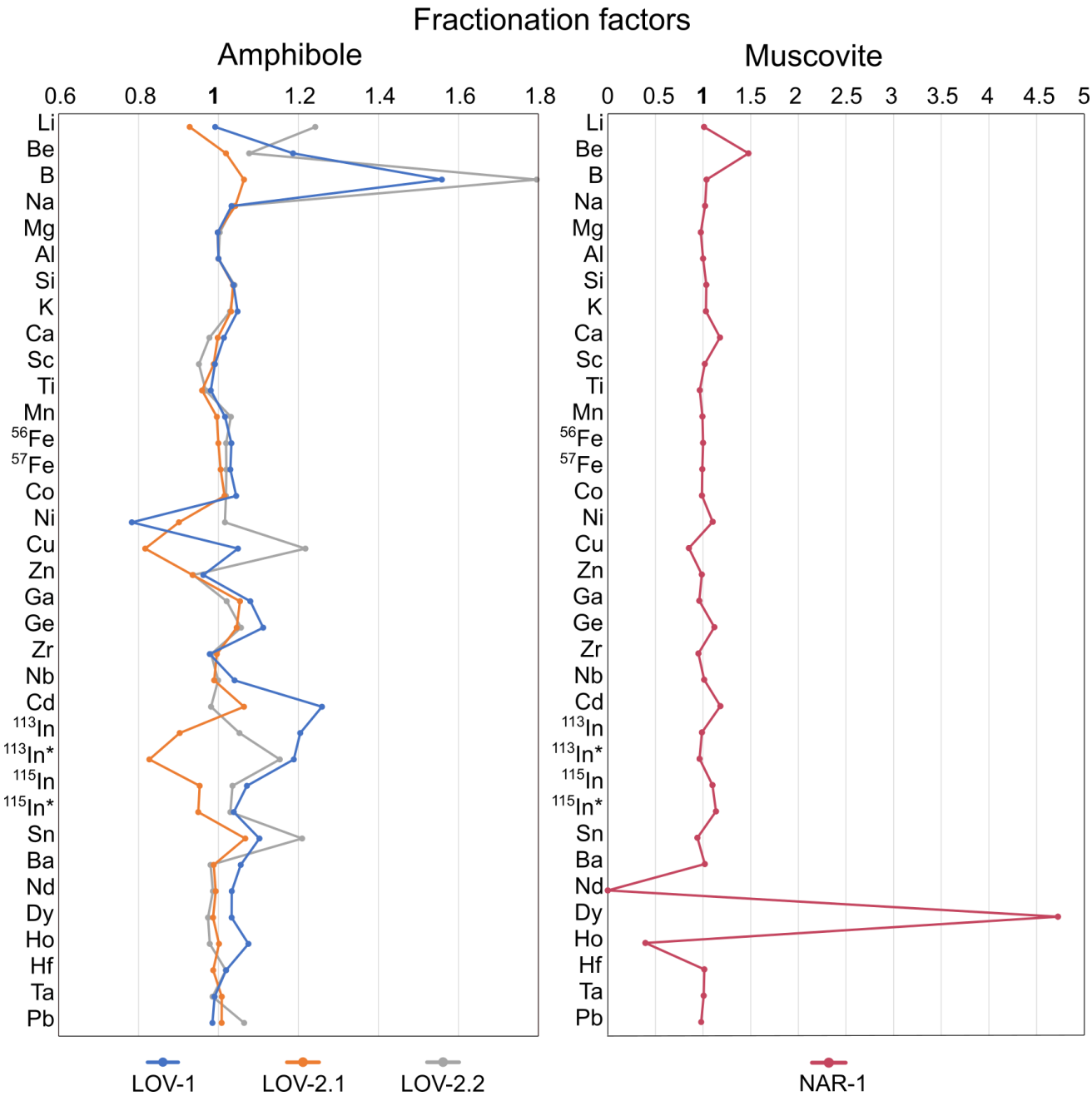

Figure 2. Calculated fractionation factors for selected amphibole and muscovite samples. Note the different scales. Asterisk (*) refers to elements corrected for isobaric interferences, whereas "^{113}In" and "^{115}In" refer to the total In concentrations calculated from masses 113 and 115, respectively. Fractionation factors were calculated with in-house software based on Fryer et al. (1995).

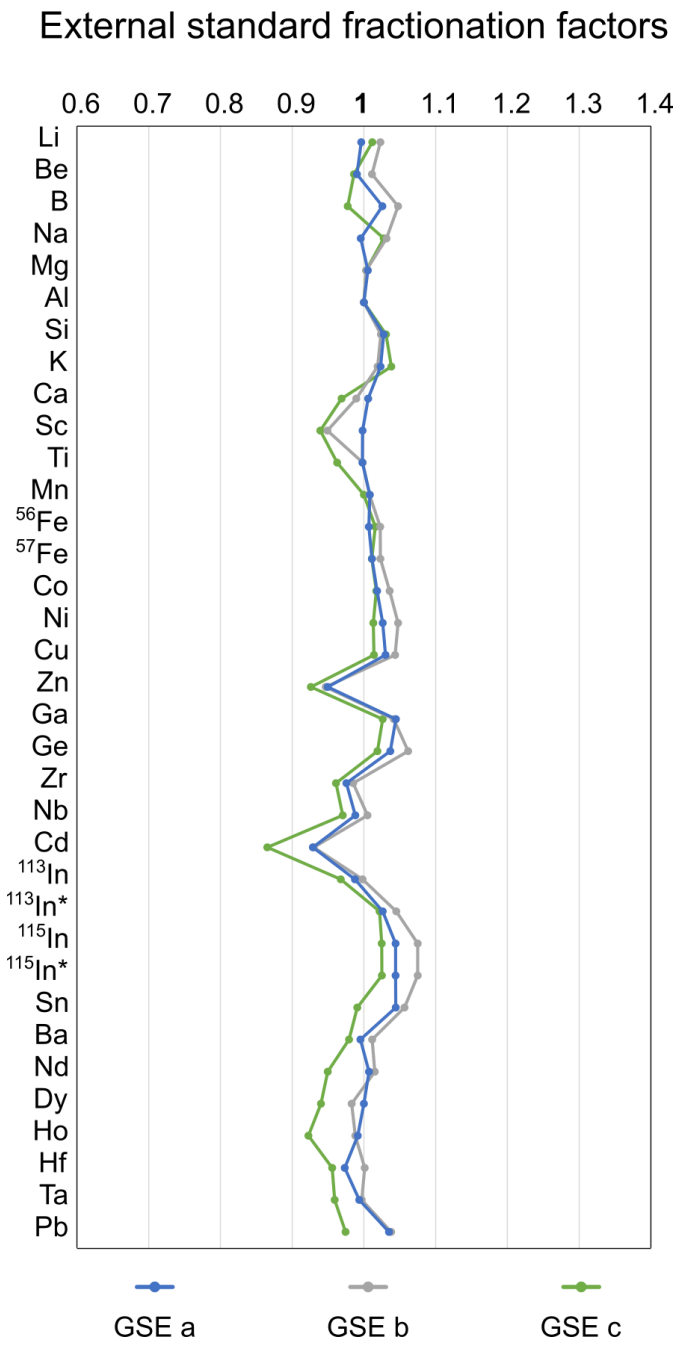

Figure 3. Calculated fractionation factors for selected external GSE-1G standards. Asterisk (*) refers to elements corrected for isobaricl interferences, whereas "^{113}In" and "^{115}In" refer to the total In concentrations calculated from masses 113 and 115, respectively. Fractionation factors were calculated with in-house software based on Fryer et al. (1995).

APPENDIX 5

Table A. CIPW normative minerals calculated with GCDkit software (Janoušek et al. 2006) on the basis of ("fine" fraction, see Chapter 3.1.) bulk rock composition.

	LOV-1	LOV-2	LOV-3	LOV-4	LOV-5	LOV-6	OLR09	NAR-1	VIG-1	KUI-3
Q	25.73	22.12	35.29	33.01	27.38	20.55	31.08	37.24	24.89	14.12
C	0.19	0.00	0.00	0.76	0.00	0.00	2.04	1.85	0.00	0.34
Or	34.16	35.34	35.75	34.45	31.62	29.49	29.96	24.41	15.01	13.83
Ab	24.62	24.62	20.56	21.49	20.14	25.30	23.35	30.55	40.62	39.01
An	6.89	7.67	2.60	2.73	9.15	12.82	6.29	2.75	11.01	14.63
Di	0.00	0.62	0.57	0.00	0.60	1.38	0.00	0.00	0.86	0.00
Hy	5.15	6.21	2.59	4.26	7.85	7.04	4.24	1.59	4.68	13.66
Il	0.61	0.82	0.29	0.48	0.86	0.95	0.49	0.11	0.48	0.84
Ap	0.17	0.24	0.05	0.14	0.21	0.28	0.17	0.19	0.19	0.31
Σ	97.51	97.63	97.70	97.32	97.79	97.82	97.62	98.68	97.73	96.73

Q = quartz; C = corundum; Or = orthoclase; Ab = albite; An = anorthite; Di = diopside; Hy = hypersthene; Il = ilmenite; Ap = apatite.

APPENDIX 6

Table A. Sample whole-rock composition comparison between the “fine” fraction (F) and “coarse” fraction (C) results, as determined by WD-XRF. Oxide element and total rows are expressed as wt.%, and trace element rows as ppm. All iron is assumed to be ferrous.

	LOV-1		LOV-2		LOV-3		LOV-4		LOV-5		LOV-6		OLR09		NAR-1		VIG-1		KUI-3	
	F	C	F	C	F	C	F	C	F	C	F	C	F	C	F	C	F	C	F	C
SiO_2	70.18	67.22	68.47	66.49	75.18	74.32	73.28	73.22	69.64	67.81	66.55	65.66	71.41	71.91	75.99	74.28	70.12	68.17	63.17	63.08
TiO_2	0.32	0.33	0.43	0.46	0.15	0.2	0.25	0.27	0.45	0.59	0.50	0.52	0.26	0.3	0.06	0.06	0.25	0.26	0.44	0.46
Al_2O_3	13.76	15.2	14.07	14.96	11.50	11.86	12.25	12.31	13.06	13.51	15.02	15.63	14.37	14.04	13.27	13.99	14.68	15.54	15.82	15.82
FeO	2.70	2.87	3.50	3.48	1.58	1.94	2.23	2.33	4.27	4.78	4.22	4.14	1.64	1.89	0.70	0.63	1.87	1.96	4.90	5
MnO	0.04	0.04	0.04	0.05	0.02	0.02	0.03	0.03	0.06	0.07	0.05	0.05	0.02	0.02	0.04	0.02	0.04	0.05	0.07	0.07
MgO	0.26	0.26	0.30	0.3	0.08	0.09	0.21	0.21	0.38	0.41	0.30	0.29	0.65	0.73	0.13	0.13	0.81	0.95	2.11	2.18
CaO	1.48	1.54	1.82	2.07	0.68	0.62	0.63	0.68	2.10	2.4	3.06	3.46	1.36	1.47	0.66	0.69	2.53	2.48	3.12	3.3
Na_2O	2.91	3.16	2.91	3.3	2.43	2.57	2.54	2.54	2.38	2.53	2.99	3.05	2.76	2.73	3.61	4	4.80	5.04	4.61	4.52
K_2O	5.78	6.73	5.98	5.86	6.05	6.02	5.83	5.72	5.35	5.26	4.99	4.87	5.07	4.61	4.13	4.46	2.54	2.89	2.34	2.41
P_2O_5	0.07	0.07	0.10	0.1	0.02	0.02	0.06	0.06	0.09	0.15	0.12	0.13	0.07	0.07	0.08	0.06	0.08	0.09	0.13	0.15
Sub-total	97.50	97.42	97.62	97.07	97.69	97.66	97.31	97.37	97.78	97.51	97.80	97.80	97.61	97.77	98.67	98.32	97.72	97.43	96.71	96.99
V	6	6	8	8	b.d.	4	8	b.d.	8	4	b.d.	b.d.	26	31	7	7	33	30	84	86
Cr	b.d.	b.d.	b.d.	b.d.	b.d.	6	b.d.	b.d.	b.d.	b.d.	b.d.	b.d.	b.d.	9	b.d.	12	15	19	76	77
Ni	b.d.	b.d.	2	b.d.	2	4	2	b.d.	2	4	2	2	5	5	b.d.	3	9	11	28	27
Cu	11	15	6	7	b.d.	b.d.	b.d.	b.d.	13	13	6	8	4	5	b.d.	b.d.	8	8	5	7
Zn	87	84	87	84	59	64	60	64	147	149	112	97	24	27	22	26	36	39	71	67
Rb	245	284	247	241	393	404	388	388	266	265	234	225	168	166	253	273	56	65	88	92
Sr	152	173	152	160	37	38	56	53	164	170	231	256	507	482	65	77	594	613	662	664
Y	45	45	59	62	95	82	68	74	97	101	70	70	12	13	12	14	7	6	10	12
Zr	282	343	436	406	254	395	239	264	464	647	470	522	123	151	36	40	73	91	95	118
Nb	21	24	21	25	28	34	26	31	28	29	25	25	9	10	15	11	8	7	9	9
Ba	1127	1446	1105	1178	233	233	324	332	792	784	1091	1152	829	729	196	222	760	858	496	513

La	98	63	81	80	166	54	111	96	151	99	112	110	43	46	b.d.	b.d.	21	14	34	29
Ce	162	112	144	143	287	90	193	187	268	177	198	183	81	78	b.d.	b.d.	39	30	48	54
U	9	7	9	8	11	14	17	17	6	7	7	3	5	6	13	14	2	2	2	b.d.
Total	97.71	97.68	97.86	97.30	97.85	97.80	97.46	97.53	98.02	97.76	98.06	98.07	97.79	97.95	98.74	98.39	97.89	97.61	96.89	97.17
Type	A	A	A	A	A	A	A	A	A	A	A	A	S	S	S	S	I	I	I	I
A/CNK	1.00	0.99	0.97	0.96	0.98	1.00	1.05	1.06	0.97	0.95	0.95	0.94	1.15	1.16	1.14	1.10	1.00	0.99	0.96	0.98
Fe* *	0.91	0.92	0.92	0.92	0.95	0.96	0.91	0.92	0.92	0.92	0.93	0.93	0.72	0.72	0.84	0.83	0.70	0.67	0.70	0.70
MALI*	7.21	8.35	7.07	7.09	7.80	7.97	7.74	7.58	5.63	5.39	4.92	4.46	6.47	5.87	7.08	7.77	4.81	5.45	3.83	3.63
ASI*	1.01	1.00	0.97	0.97	0.98	1.00	1.06	1.07	0.97	0.96	0.95	0.95	1.16	1.16	1.15	1.11	0.97	0.98	1.01	1.00

Type = S-I-A-M classification of granitoids after Whalen et al. (1987) and Chappell & White (2001); b.d. = below detection limit; * = after Frost et al. (2001); Fe* = FeOtot/(FeOtot + MgO); MALI = Modified alkali-lime index; ASI = Aluminum saturation index (corrected for apatite).

APPENDIX 7

Table A. Major element composition of A-type biotite samples LOV-1, LOV-2.1, and LOV-2.2 (in wt.%) determined by EPMA. Cations calculated on the basis of 22 oxygens.

	LOV-1						LOV-2.1		LOV-2.2										
	grain 2	grain 3	grain 4	grain 5	grain 7	grain 8	grain 1	grain 7	grain 1	grain 3	grain 6	grain 7	grain 8	grain 9	grain 10	grain 11	grain 12	grain 13	grain 14
SiO_2	33.83	34.07	33.73	33.39	34.01	34.68	34.62	34.90	33.76	34.28	33.37	33.17	34.76	34.25	34.82	34.66	34.70	34.48	34.02
TiO_2	3.02	2.56	3.25	2.73	3.09	2.39	3.90	3.10	1.91	2.48	1.78	0.73	3.20	2.77	3.48	3.05	3.59	3.48	3.51
Al_2O_3	12.19	12.18	12.59	12.71	12.31	12.24	11.80	11.97	12.51	11.62	11.68	12.97	11.90	11.70	11.93	12.05	11.94	11.80	12.01
FeO	35.62	35.36	34.92	34.50	33.83	33.07	33.99	30.68	34.94	33.90	34.36	35.90	32.78	32.74	33.19	32.86	33.13	32.44	32.29
MgO	1.85	1.99	2.01	2.41	3.33	3.51	2.31	4.46	2.01	2.37	1.99	2.25	2.95	3.03	3.08	3.37	3.24	2.98	2.99
CaO	0.46	b.d.	b.d.	b.d.	b.d.	b.d.	b.d.	b.d.	b.d.	b.d.	b.d.	b.d.	b.d.	b.d.	b.d.	b.d.	b.d.	b.d.	b.d.
Na_2O	b.d.	b.d.	b.d.	b.d.	b.d.	b.d.	b.d.	b.d.	b.d.	b.d.	b.d.	b.d.	0.13	b.d.	0.12	b.d.	0.12	b.d.	0.14
K_2O	8.10	8.24	8.34	7.67	7.95	8.44	8.98	8.48	8.98	8.87	8.11	7.79	8.62	8.52	8.83	8.89	8.89	8.45	8.13
Li_2O †	0.13	0.13	0.10	0.13	0.12	0.10	0.14	0.13	0.13	0.11	0.11	0.12	0.14	0.11	0.14	0.16	0.17	0.14	0.16
H_2O*	3.60	3.59	3.61	3.57	3.63	3.63	3.65	3.64	3.56	3.56	3.47	3.51	3.63	3.57	3.66	3.64	3.67	3.61	3.59
Total	98.81	98.11	98.54	97.11	98.27	98.05	99.38	97.34	97.80	97.17	94.87	96.44	98.11	96.69	99.24	98.70	99.45	97.38	96.84
Si	5.63	5.70	5.61	5.61	5.63	5.73	5.69	5.75	5.68	5.78	5.77	5.66	5.75	5.76	5.70	5.70	5.67	5.73	5.69
Al^{IV}	2.37	2.30	2.39	2.39	2.37	2.27	2.29	2.25	2.32	2.22	2.23	2.34	2.25	2.24	2.30	2.30	2.30	2.27	2.31
T-site total	8.00	8.00	8.00	8.00	8.00	8.00	7.98	8.00	8.00	8.00	8.00	8.00	8.00	8.00	8.00	8.00	7.97	8.00	8.00
Al^{VI}	0.02	0.10	0.08	0.13	0.03	0.12	0.00	0.07	0.17	0.08	0.16	0.27	0.06	0.07	0.00	0.04	0.00	0.05	0.05
Ti	0.38	0.32	0.41	0.34	0.38	0.30	0.48	0.38	0.24	0.31	0.23	0.09	0.40	0.35	0.43	0.38	0.44	0.44	0.44
Fe	4.96	4.94	4.86	4.85	4.68	4.57	4.67	4.23	4.92	4.78	4.97	5.12	4.53	4.60	4.55	4.52	4.53	4.51	4.51
Mg	0.46	0.50	0.50	0.60	0.82	0.87	0.57	1.09	0.50	0.59	0.51	0.57	0.73	0.76	0.75	0.83	0.79	0.74	0.74
Li †	0.09	0.08	0.06	0.09	0.08	0.06	0.09	0.08	0.09	0.07	0.07	0.08	0.09	0.08	0.09	0.10	0.11	0.10	0.11
M-site total	5.81	5.86	5.84	5.92	5.91	5.85	5.72	5.77	5.83	5.77	5.87	6.05	5.72	5.78	5.73	5.77	5.76	5.73	5.75
Ca	0.08	0.00	0.00	0.00	0.00	0.00	0.00	0.00	0.00	0.00	0.00	0.00	0.00	0.00	0.00	0.00	0.00	0.00	0.00

Na	0.00	0.00	0.00	0.00	0.00	0.00	0.00	0.00	0.00	0.00	0.00	0.00	0.04	0.00	0.04	0.00	0.04	0.00	0.05
K	1.72	1.76	1.77	1.64	1.68	1.78	1.88	1.78	1.93	1.91	1.79	1.70	1.82	1.83	1.85	1.87	1.85	1.79	1.73
I-site total	1.80	1.76	1.77	1.64	1.68	1.78	1.88	1.78	1.93	1.91	1.79	1.70	1.86	1.83	1.88	1.87	1.89	1.79	1.78
OH	4.00	4.00	4.00	4.00	4.00	4.00	4.00	4.00	4.00	4.00	4.00	4.00	4.00	4.00	4.00	4.00	4.00	4.00	4.00
Total	19.70	19.70	19.67	19.65	19.67	19.70	19.67	19.64	19.84	19.75	19.74	19.83	19.67	19.69	19.71	19.74	19.74	19.62	19.63
Al total	2.39	2.40	2.47	2.52	2.40	2.39	2.29	2.32	2.48	2.31	2.38	2.61	2.32	2.32	2.30	2.34	2.30	2.31	2.37
Fe/Fe+Mg	0.92	0.91	0.91	0.89	0.85	0.84	0.89	0.79	0.91	0.89	0.91	0.90	0.86	0.86	0.86	0.85	0.85	0.86	0.86
mgli ‡	0.37	0.41	0.43	0.52	0.74	0.80	0.47	1.01	0.42	0.52	0.44	0.49	0.63	0.68	0.66	0.72	0.68	0.64	0.64
feal ‡	5.32	5.17	5.19	5.07	5.04	4.75	5.15	4.54	4.99	5.01	5.05	4.95	4.86	4.88	4.97	4.86	4.97	4.90	4.90

b.d. = below detection limit at a 95% confidence level; * = calculated stoichiometrically; † = calculated from LA-ICP-MS analysis; ‡ = after Tischendorf et al. (1997).

Table B. Major element composition of A-type biotite samples LOV-3 and LOV-4 (in wt.%) determined by EPMA. Cations calculated on the basis of 22 oxygens.

	LOV-3										LOV-4								
	grain 1	grain 2	grain 3	grain 4	grain 5	grain 6	grain 7	grain 8	grain 9	grain 10	grain 1	grain 2	grain 3	grain 4	grain 5	grain 7	grain 8	grain 9	grain 10
SiO_2	34.83	34.67	34.77	34.63	33.50	34.13	34.13	34.31	34.51	33.87	34.50	34.30	33.97	34.74	34.61	35.08	35.32	35.43	35.05
TiO_2	1.98	2.01	2.75	3.25	2.84	1.79	2.05	2.71	2.32	2.65	2.52	2.92	2.43	2.33	2.08	2.68	3.13	2.74	2.26
Al_2O_3	14.57	14.46	14.36	14.25	14.28	14.26	15.14	14.18	14.65	14.66	15.83	15.32	15.53	15.09	15.77	14.50	14.55	15.08	15.25
FeO	34.91	35.30	35.15	35.54	34.80	35.28	35.37	34.58	35.71	36.41	33.38	32.23	32.57	31.85	32.61	30.75	30.88	31.11	32.08
MgO	0.82	0.85	0.79	0.84	1.04	0.88	0.76	0.71	0.75	0.79	2.19	2.17	2.06	2.12	2.20	2.18	2.24	2.31	2.20
CaO	b.d.	b.d.	b.d.	b.d.	b.d.	b.d.	b.d.	b.d.	b.d.	b.d.	b.d.	b.d.	b.d.	b.d.	b.d.	b.d.	b.d.	b.d.	b.d.
Na_2O	0.13	b.d.	b.d.	b.d.	0.11	b.d.	b.d.	0.15	b.d.	0.15	0.17	0.13	b.d.	b.d.	0.14	b.d.	b.d.	0.13	0.11
K_2O	8.59	8.87	8.47	8.65	7.80	8.46	8.46	8.49	8.28	8.54	8.53	8.43	8.36	8.49	8.54	8.59	8.83	8.81	8.74
Li_2O †	0.29	0.28	0.28	0.25	0.26	0.26	0.23	0.27	0.21	0.22	0.21	0.22	0.20	0.19	0.16	0.16	0.19	0.16	0.17
H_2O*	3.68	3.68	3.70	3.72	3.62	3.62	3.67	3.65	3.68	3.69	3.76	3.71	3.68	3.69	3.73	3.67	3.71	3.74	3.72
Total	99.79	100.11	100.27	101.13	98.24	98.68	99.81	99.03	100.12	100.99	101.07	99.44	98.80	98.49	99.83	97.61	98.84	99.50	99.59

Si	5.68	5.65	5.64	5.59	5.55	5.65	5.57	5.64	5.62	5.51	5.50	5.54	5.53	5.65	5.57	5.73	5.70	5.68	5.65
Al^{IV}	2.32	2.35	2.36	2.41	2.45	2.35	2.43	2.36	2.38	2.49	2.50	2.46	2.47	2.35	2.43	2.27	2.30	2.32	2.35
T-site total	8.00	8.00	8.00	8.00	8.00	8.00	8.00	8.00	8.00	8.00	8.00	8.00	8.00	8.00	8.00	8.00	8.00	8.00	8.00
Al^{VI}	0.48	0.43	0.39	0.30	0.34	0.43	0.49	0.39	0.43	0.32	0.48	0.46	0.51	0.54	0.56	0.53	0.47	0.53	0.54
Ti	0.24	0.25	0.34	0.39	0.35	0.22	0.25	0.34	0.28	0.32	0.30	0.35	0.30	0.28	0.25	0.33	0.38	0.33	0.27
Fe	4.76	4.81	4.77	4.80	4.82	4.89	4.83	4.75	4.86	4.95	4.45	4.35	4.44	4.33	4.39	4.20	4.17	4.17	4.32
Mg	0.20	0.21	0.19	0.20	0.26	0.22	0.19	0.17	0.18	0.19	0.52	0.52	0.50	0.51	0.53	0.53	0.54	0.55	0.53
Li †	0.19	0.18	0.19	0.16	0.17	0.17	0.15	0.18	0.14	0.15	0.13	0.15	0.13	0.12	0.10	0.11	0.12	0.10	0.11
M-site total	5.67	5.70	5.68	5.69	5.77	5.76	5.76	5.65	5.76	5.78	5.75	5.69	5.75	5.68	5.73	5.59	5.56	5.59	5.66
Ca	0.00	0.00	0.00	0.00	0.00	0.00	0.00	0.00	0.00	0.00	0.00	0.00	0.00	0.00	0.00	0.00	0.00	0.00	0.00
Na	0.04	0.00	0.00	0.00	0.04	0.00	0.00	0.05	0.00	0.05	0.05	0.04	0.00	0.00	0.05	0.00	0.00	0.04	0.03
K	1.79	1.84	1.75	1.78	1.65	1.79	1.76	1.78	1.72	1.77	1.74	1.74	1.74	1.76	1.75	1.79	1.82	1.80	1.80
I-site total	1.83	1.84	1.75	1.78	1.68	1.79	1.76	1.83	1.72	1.82	1.79	1.78	1.74	1.76	1.80	1.79	1.82	1.84	1.83
OH	4.00	4.00	4.00	4.00	4.00	4.00	4.00	4.00	4.00	4.00	4.00	4.00	4.00	4.00	4.00	4.00	4.00	4.00	4.00
Total	19.69	19.73	19.62	19.63	19.63	19.72	19.67	19.65	19.62	19.75	19.67	19.61	19.61	19.56	19.63	19.49	19.50	19.53	19.60
Al total	2.80	2.78	2.75	2.71	2.79	2.78	2.92	2.75	2.81	2.81	2.97	2.92	2.98	2.89	2.99	2.79	2.77	2.85	2.89
Fe/Fe+Mg	0.96	0.96	0.96	0.96	0.95	0.96	0.96	0.96	0.96	0.96	0.90	0.89	0.90	0.89	0.89	0.89	0.89	0.88	0.89
mgli ‡	0.01	0.02	0.01	0.04	0.08	0.04	0.04	0.00	0.04	0.04	0.39	0.38	0.37	0.39	0.43	0.42	0.42	0.45	0.42
feal ‡	4.52	4.63	4.72	4.89	4.84	4.68	4.59	4.70	4.72	4.96	4.28	4.25	4.22	4.07	4.08	4.01	4.08	3.97	4.05

b.d. = below detection limit at a 95% confidence level; * = calculated stoichiometrically; † = calculated from LA-ICP-MS analysis; ‡ = after Tischendorf et al. (1997).

Table C. Major element composition of A-type biotite sample LOV-5 (in wt.%) determined by EPMA. Cations calculated on the basis of 22 oxygens.

	LOV-5									
	grain 1	grain 2	grain 3	grain 4	grain 5	grain 6	grain 7	grain 8	grain 9	grain 10
SiO_2	33.92	33.82	33.62	33.64	33.30	33.98	33.26	33.19	33.76	33.19
TiO_2	3.10	2.72	2.11	1.81	3.04	2.30	2.18	1.15	2.60	2.07
Al_2O_3	12.22	12.19	12.24	12.66	12.27	12.19	12.29	12.57	12.33	12.64
FeO	36.74	36.52	36.78	36.22	34.68	35.16	35.88	36.22	36.03	35.64
MgO	1.49	1.33	1.52	1.80	1.76	2.19	1.47	1.53	1.49	1.35
CaO	b.d.	b.d.	b.d.	b.d.	b.d.	b.d.	b.d.	b.d.	b.d.	b.d.
Na_2O	0.18	b.d.	b.d.	b.d.	b.d.	b.d.	b.d.	b.d.	b.d.	b.d.
K_2O	8.15	8.38	8.21	7.71	8.37	8.42	8.23	6.82	8.35	8.08
Li_2O †	0.11	0.13	0.13	0.14	0.14	0.12	0.13	0.09	0.12	0.12
H_2O*	3.62	3.58	3.56	3.56	3.55	3.58	3.52	3.47	3.57	3.52
Total	99.52	98.67	98.16	97.54	97.11	97.92	96.98	95.05	98.24	96.60
Si	5.63	5.66	5.67	5.67	5.63	5.70	5.66	5.73	5.66	5.66
Al^{IV}	2.37	2.34	2.33	2.33	2.37	2.30	2.34	2.27	2.34	2.34
T-site total	8.00	8.00	8.00	8.00	8.00	8.00	8.00	8.00	8.00	8.00
Al^{VI}	0.01	0.07	0.10	0.18	0.08	0.11	0.13	0.29	0.10	0.20
Ti	0.39	0.34	0.27	0.23	0.39	0.29	0.28	0.15	0.33	0.27
Fe	5.10	5.11	5.18	5.10	4.90	4.93	5.11	5.23	5.06	5.08
Mg	0.37	0.33	0.38	0.45	0.44	0.55	0.37	0.39	0.37	0.34
Li †	0.07	0.08	0.09	0.10	0.09	0.08	0.09	0.06	0.08	0.08
M-site total	5.87	5.86	5.93	5.97	5.81	5.87	5.89	6.06	5.86	5.89
Ca	0.00	0.00	0.00	0.00	0.00	0.00	0.00	0.00	0.00	0.00
Na	0.06	0.00	0.00	0.00	0.00	0.00	0.00	0.00	0.00	0.00
K	1.72	1.79	1.76	1.66	1.80	1.80	1.79	1.50	1.79	1.76
I-site total	1.78	1.79	1.76	1.66	1.80	1.80	1.79	1.50	1.79	1.76

OH	4.00	4.00	4.00	4.00	4.00	4.00	4.00	4.00	4.00	4.00
Total	19.72	19.73	19.78	19.72	19.71	19.75	19.77	19.62	19.72	19.73
Al total	2.39	2.40	2.43	2.51	2.45	2.41	2.47	2.56	2.44	2.54
Fe/Fe+Mg	0.93	0.94	0.93	0.92	0.92	0.90	0.93	0.93	0.93	0.94
mgli ‡	0.30	0.25	0.30	0.35	0.35	0.47	0.28	0.33	0.29	0.26
feal ‡	5.47	5.39	5.35	5.15	5.21	5.11	5.26	5.09	5.28	5.15

b.d. = below detection limit at a 95% confidence level; * = calculated stoichiometrically; † = calculated from LA-ICP-MS analysis; ‡ = after Tischendorf et al. (1997).

Table D. Major element composition of A-type biotite samples LOV-6.1 and LOV-6.2 (in wt.%) determined by EPMA. Cations calculated on the basis of 22 oxygens.

	LOV-6.1									LOV-6.2										
	grain 1	grain 2	grain 3	grain 4	grain 5	grain 6	grain 7	grain 8	grain 9	grain 1	grain 2	grain 3	grain 4	grain 5	grain 6	grain 7	grain 8	grain 9	grain 10	grain 11
SiO_2	33.41	32.69	32.55	32.88	33.16	33.31	33.54	33.06	33.33	32.93	33.64	33.23	33.23	33.28	33.35	33.89	32.99	33.83	32.81	33.60
TiO_2	3.37	3.04	2.47	3.36	3.14	2.90	3.80	2.53	2.60	3.51	1.83	2.66	2.68	2.65	1.81	2.61	2.76	2.58	2.61	2.65
Al_2O_3	13.17	12.35	12.67	12.50	12.61	12.41	12.47	12.76	12.39	12.45	12.72	12.57	12.22	12.73	12.62	12.53	12.40	12.67	12.48	12.26
FeO	35.63	35.96	36.85	37.08	36.77	37.75	34.16	36.82	37.37	36.75	36.52	37.71	36.31	36.16	36.12	36.86	37.53	36.87	35.90	36.18
MgO	1.03	0.88	0.79	0.79	0.96	1.10	1.62	0.67	0.68	1.00	1.89	1.13	1.73	1.56	1.79	1.70	0.87	1.32	1.15	0.79
CaO	b.d.	b.d.	b.d.	b.d.	b.d.	b.d.	b.d.	0.14	b.d.	b.d.	0.16	b.d.	b.d.	b.d.	b.d.	b.d.	b.d.	b.d.	b.d.	b.d.
Na_2O	b.d.	b.d.	b.d.	b.d.	b.d.	0.12	b.d.	b.d.	b.d.	b.d.	0.14	b.d.	b.d.	b.d.	b.d.	b.d.	b.d.	b.d.	0.12	b.d.
K_2O	8.40	8.06	7.90	8.12	8.48	8.08	8.26	7.70	8.13	7.83	7.71	8.09	8.11	8.36	8.19	8.13	7.85	8.10	7.87	7.68
Li_2O †	0.15	0.14	0.15	0.17	0.19	0.19	0.14	0.19	0.15	0.16	0.16	0.15	0.14	0.15	0.17	0.16	0.20	0.18	0.18	0.20
H_2O*	3.60	3.51	3.50	3.56	3.58	3.59	3.58	3.54	3.55	3.56	3.58	3.58	3.56	3.58	3.55	3.62	3.55	3.60	3.51	3.53
Total	98.78	96.63	96.88	98.46	98.87	99.45	97.57	97.41	98.19	98.19	98.35	99.11	97.98	98.48	97.60	99.49	98.15	99.15	96.64	96.89
Si	5.56	5.59	5.57	5.54	5.56	5.56	5.62	5.61	5.63	5.54	5.63	5.57	5.60	5.58	5.64	5.62	5.58	5.63	5.60	5.70
Al^{IV}	2.44	2.41	2.43	2.46	2.44	2.44	2.38	2.39	2.37	2.46	2.37	2.43	2.40	2.42	2.36	2.38	2.42	2.37	2.40	2.30
T-site total	8.00	8.00	8.00	8.00	8.00	8.00	8.00	8.00	8.00	8.00	8.00	8.00	8.00	8.00	8.00	8.00	8.00	8.00	8.00	8.00

Al^{VI}	0.14	0.08	0.13	0.02	0.05	0.00	0.08	0.16	0.10	0.01	0.14	0.05	0.03	0.09	0.15	0.07	0.05	0.11	0.11	0.16
Ti	0.42	0.39	0.32	0.43	0.40	0.36	0.48	0.32	0.33	0.44	0.23	0.33	0.34	0.33	0.23	0.32	0.35	0.32	0.33	0.34
Fe	4.96	5.14	5.27	5.22	5.15	5.27	4.78	5.22	5.28	5.17	5.11	5.28	5.12	5.07	5.10	5.11	5.31	5.13	5.13	5.14
Mg	0.26	0.22	0.20	0.20	0.24	0.27	0.40	0.17	0.17	0.25	0.47	0.28	0.44	0.39	0.45	0.42	0.22	0.33	0.29	0.20
Li †	0.10	0.10	0.10	0.11	0.13	0.13	0.09	0.13	0.10	0.11	0.11	0.10	0.10	0.10	0.11	0.11	0.13	0.12	0.13	0.13
M-site total	5.78	5.84	5.92	5.87	5.83	5.91	5.75	5.87	5.88	5.88	5.96	5.95	5.92	5.89	5.94	5.92	5.92	5.89	5.87	5.83
Ca	0.00	0.00	0.00	0.00	0.00	0.00	0.00	0.03	0.00	0.00	0.03	0.00	0.00	0.00	0.00	0.00	0.00	0.00	0.00	0.00
Na	0.00	0.00	0.00	0.00	0.00	0.04	0.00	0.00	0.00	0.00	0.05	0.00	0.00	0.00	0.00	0.00	0.00	0.00	0.04	0.00
K	1.78	1.76	1.72	1.74	1.81	1.72	1.76	1.67	1.75	1.68	1.65	1.73	1.74	1.79	1.76	1.72	1.69	1.72	1.71	1.66
I-site total	1.78	1.76	1.72	1.74	1.81	1.76	1.76	1.69	1.75	1.68	1.72	1.73	1.74	1.79	1.76	1.72	1.69	1.72	1.76	1.66
OH	4.00	4.00	4.00	4.00	4.00	4.00	4.00	4.00	4.00	4.00	4.00	4.00	4.00	4.00	4.00	4.00	4.00	4.00	4.00	4.00
Total	19.67	19.70	19.74	19.72	19.77	19.80	19.60	19.69	19.73	19.67	19.78	19.77	19.77	19.78	19.81	19.75	19.75	19.73	19.75	19.63
Al total	2.58	2.49	2.56	2.48	2.49	2.44	2.46	2.55	2.47	2.47	2.51	2.48	2.43	2.52	2.51	2.45	2.47	2.48	2.51	2.45
Fe/Fe+Mg	0.95	0.96	0.96	0.96	0.96	0.95	0.92	0.97	0.97	0.95	0.92	0.95	0.92	0.93	0.92	0.92	0.96	0.94	0.95	0.96
mgli ‡	0.15	0.13	0.10	0.08	0.12	0.15	0.31	0.04	0.07	0.14	0.37	0.18	0.34	0.29	0.34	0.31	0.09	0.21	0.17	0.07
feal ‡	5.24	5.45	5.47	5.63	5.50	5.63	5.18	5.39	5.51	5.60	5.20	5.57	5.43	5.31	5.18	5.37	5.61	5.34	5.35	5.32

b.d. = below detection limit at a 95% confidence level; * = calculated stoichiometrically; † = calculated from LA-ICP-MS analysis; ‡ = after Tischendorf et al. (1997).

Table E. Major element composition of S-type biotite samples OLR09 and NAR-1 (in wt.%) determined by EPMA. Cations calculated on the basis of 22 oxygens.

	OLR09											NAR-1		
	grain 1	grain 2	grain 3	grain 4	grain 5	grain 6	grain 7	grain 8	grain 9	grain 10	grain 11	grain 8	grain 9	grain 10
SiO_2	35.23	34.58	35.65	35.12	35.15	35.45	35.03	34.82	35.61	35.23	35.87	34.40	34.34	34.57
TiO_2	2.66	2.60	2.39	2.16	2.23	2.56	2.10	2.54	2.08	2.59	2.42	2.00	1.47	2.05
Al_2O_3	16.09	16.16	15.93	16.37	15.41	16.43	16.39	16.03	16.46	16.03	16.25	16.90	17.11	17.28
FeO	21.47	21.95	21.68	21.92	20.95	21.57	21.78	21.43	21.11	21.62	22.02	26.74	26.63	26.62
MgO	9.32	9.31	9.13	9.06	9.40	8.89	9.22	8.94	9.10	9.13	9.19	3.81	3.81	3.82
CaO	b.d.	b.d.	b.d.	b.d.	b.d.	0.22	b.d.	b.d.	b.d.	b.d.	b.d.	b.d.	b.d.	b.d.
Na_2O	b.d.	b.d.	b.d.	b.d.	b.d.	b.d.	b.d.	b.d.	b.d.	b.d.	b.d.	0.10	b.d.	b.d.
K_2O	9.13	8.36	8.83	8.95	8.87	7.96	8.94	8.76	8.88	9.05	9.00	8.88	8.74	8.60
Li_2O †	0.03	0.03	0.04	0.03	0.03	0.04	0.03	0.03	0.03	0.03	0.04	0.50	0.49	0.51
H_2O*	3.83	3.80	3.83	3.82	3.77	3.83	3.81	3.78	3.83	3.82	3.87	3.72	3.70	3.74
Total	97.76	96.78	97.48	97.43	95.82	96.94	97.32	96.33	97.10	97.49	98.65	97.05	96.28	97.19
Si	5.51	5.46	5.58	5.52	5.60	5.55	5.51	5.52	5.58	5.53	5.56	5.54	5.57	5.54
Al^{IV}	2.49	2.54	2.42	2.48	2.40	2.45	2.49	2.48	2.42	2.47	2.44	2.46	2.43	2.46
T-site total	8.00	8.00	8.00	8.00	8.00	8.00	8.00	8.00	8.00	8.00	8.00	8.00	8.00	8.00
Al^{VI}	0.48	0.47	0.52	0.55	0.49	0.58	0.54	0.52	0.62	0.49	0.52	0.75	0.84	0.81
Ti	0.31	0.31	0.28	0.26	0.27	0.30	0.25	0.30	0.24	0.31	0.28	0.24	0.18	0.25
Fe	2.81	2.90	2.84	2.88	2.79	2.83	2.86	2.84	2.77	2.84	2.85	3.60	3.61	3.57
Mg	2.17	2.19	2.13	2.12	2.23	2.08	2.16	2.11	2.13	2.14	2.12	0.92	0.92	0.91
Li †	0.02	0.02	0.02	0.02	0.02	0.02	0.02	0.02	0.02	0.02	0.02	0.32	0.32	0.33
M-site total	5.77	5.87	5.77	5.80	5.78	5.79	5.82	5.78	5.76	5.77	5.78	5.52	5.55	5.53
Ca	0.00	0.00	0.00	0.00	0.00	0.04	0.00	0.00	0.00	0.00	0.00	0.00	0.00	0.00
Na	0.00	0.00	0.00	0.00	0.00	0.00	0.00	0.00	0.00	0.00	0.00	0.03	0.00	0.00
K	1.82	1.68	1.76	1.79	1.80	1.59	1.79	1.77	1.78	1.81	1.78	1.83	1.81	1.76
I-site total	1.82	1.68	1.76	1.79	1.80	1.63	1.79	1.77	1.78	1.81	1.78	1.86	1.81	1.76
OH	4.00	4.00	4.00	4.00	4.00	4.00	4.00	4.00	4.00	4.00	4.00	4.00	4.00	4.00
Total	19.61	19.58	19.56	19.62	19.60	19.44	19.63	19.57	19.55	19.60	19.58	19.70	19.68	19.62
Al total	2.97	3.01	2.94	3.03	2.89	3.03	3.04	3.00	3.04	2.96	2.97	3.21	3.27	3.27
Fe/Fe+Mg	0.56	0.57	0.57	0.58	0.56	0.58	0.57	0.57	0.57	0.57	0.57	0.80	0.80	0.80
mgli ‡	2.15	2.17	2.11	2.10	2.21	2.05	2.14	2.10	2.11	2.12	2.10	0.59	0.60	0.58

feal ‡	2.64	2.74	2.60	2.59	2.57	2.54	2.57	2.63	2.39	2.65	2.61	3.09	2.95	3.01

b.d. = below detection limit at a 95% confidence level; * = calculated stoichiometrically; † = calculated from LA-ICP-MS analysis; ‡ = after Tischendorf et al. (1997).

Table F. Major element composition of I-type biotite samples VIG-1 and KUI-3 (in wt.%) determined by EPMA. Cations calculated on the basis of 22 oxygens.

	VIG-1										KUI-3									
	grain 1	grain 2	grain 3	grain 4	grain 5	grain 6	grain 7	grain 8	grain 9	grain 10	grain 1	grain 2	grain 3	grain 4	grain 5	grain 6	grain 7	grain 8	grain 9	grain 10
SiO_2	37.55	37.31	37.32	37.30	37.64	36.06	37.35	37.33	37.99	37.53	36.14	36.34	36.46	36.54	36.13	36.40	36.20	36.62	36.44	36.34
TiO_2	1.47	1.27	0.72	0.83	1.22	1.24	1.30	1.15	1.60	1.50	1.95	1.97	2.12	2.02	1.86	1.78	1.82	1.55	1.90	1.58
Al_2O_3	15.15	15.26	15.80	15.78	15.25	15.27	15.87	15.38	15.55	15.42	15.83	15.81	15.91	16.25	15.88	15.90	15.80	16.06	15.79	15.92
FeO	16.34	15.73	16.45	16.05	17.06	16.91	16.63	16.00	17.41	16.78	19.58	20.47	19.83	20.00	19.97	20.51	20.20	21.38	21.64	20.65
MgO	13.75	13.16	13.71	14.06	12.98	13.97	13.73	13.19	12.74	12.54	10.01	9.99	10.20	10.32	10.07	9.95	9.96	10.08	9.97	9.86
CaO	b.d.	0.21	0.23	0.22	b.d.	0.12	b.d.	b.d.	b.d.	b.d.	b.d.	b.d.	b.d.	b.d.	b.d.	b.d.	b.d.	b.d.	b.d.	b.d.
Na_2O	b.d.	b.d.	b.d.	b.d.	b.d.	b.d.	b.d.	b.d.	b.d.	b.d.	b.d.	b.d.	b.d.	b.d.	b.d.	b.d.	b.d.	b.d.	b.d.	b.d.
K_2O	9.72	9.17	8.41	8.19	9.43	7.61	8.50	9.03	9.70	9.51	9.18	8.83	9.20	9.34	9.21	9.37	9.09	9.48	9.58	9.41
Li_2O †	0.03	0.04	0.03	0.03	0.03	0.03	0.03	0.03	0.04	0.04	0.05	0.05	0.05	0.05	0.04	0.05	0.05	0.05	0.04	0.05
H_2O*	3.94	3.88	3.91	3.92	3.92	3.84	3.94	3.88	3.97	3.91	3.83	3.85	3.87	3.90	3.84	3.86	3.83	3.90	3.89	3.85
Total	97.95	96.02	96.57	96.38	97.54	95.07	97.35	95.98	99.00	97.22	96.57	97.30	97.65	98.41	97.02	97.81	96.95	99.12	99.26	97.65
Si	5.72	5.76	5.72	5.71	5.76	5.63	5.68	5.77	5.74	5.76	5.66	5.66	5.65	5.62	5.64	5.65	5.66	5.63	5.61	5.66
Al^{IV}	2.28	2.24	2.28	2.29	2.24	2.37	2.32	2.23	2.26	2.24	2.34	2.34	2.35	2.38	2.36	2.35	2.34	2.37	2.39	2.34
T-site total	8.00	8.00	8.00	8.00	8.00	8.00	8.00	8.00	8.00	8.00	8.00	8.00	8.00	8.00	8.00	8.00	8.00	8.00	8.00	8.00
Al^{VI}	0.44	0.54	0.58	0.56	0.51	0.43	0.53	0.57	0.50	0.54	0.58	0.56	0.55	0.57	0.57	0.56	0.57	0.55	0.48	0.58
Ti	0.17	0.15	0.08	0.10	0.14	0.15	0.15	0.13	0.18	0.17	0.23	0.23	0.25	0.23	0.22	0.21	0.21	0.18	0.22	0.18
Fe	2.08	2.03	2.11	2.06	2.18	2.21	2.12	2.07	2.20	2.15	2.56	2.66	2.57	2.57	2.61	2.66	2.64	2.75	2.79	2.69
Mg	3.12	3.03	3.13	3.21	2.96	3.25	3.11	3.04	2.87	2.87	2.34	2.32	2.36	2.37	2.35	2.30	2.32	2.31	2.29	2.29
Li †	0.02	0.02	0.02	0.02	0.02	0.02	0.02	0.02	0.02	0.02	0.03	0.03	0.03	0.03	0.03	0.03	0.03	0.03	0.03	0.03
M-site total	5.80	5.75	5.90	5.92	5.79	6.04	5.91	5.80	5.75	5.74	5.72	5.77	5.73	5.74	5.74	5.74	5.75	5.79	5.78	5.75
Ca	0.00	0.04	0.04	0.04	0.00	0.02	0.00	0.00	0.00	0.00	0.00	0.00	0.00	0.00	0.00	0.00	0.00	0.00	0.00	0.00
Na	0.00	0.00	0.00	0.00	0.00	0.00	0.00	0.00	0.00	0.00	0.00	0.00	0.00	0.00	0.00	0.00	0.00	0.00	0.00	0.00

K	1.89	1.81	1.64	1.60	1.84	1.52	1.65	1.78	1.87	1.86	1.83	1.75	1.82	1.83	1.84	1.86	1.81	1.86	1.88	1.87
I-site total	1.89	1.84	1.68	1.64	1.84	1.54	1.65	1.78	1.87	1.86	1.83	1.75	1.82	1.83	1.84	1.86	1.81	1.86	1.88	1.87
OH	4.00	4.00	4.00	4.00	4.00	4.00	4.00	4.00	4.00	4.00	4.00	4.00	4.00	4.00	4.00	4.00	4.00	4.00	4.00	4.00
Total	19.71	19.61	19.60	19.58	19.66	19.59	19.58	19.60	19.64	19.62	19.58	19.55	19.57	19.60	19.61	19.63	19.59	19.68	19.69	19.64
Al total	2.72	2.78	2.85	2.85	2.75	2.81	2.85	2.80	2.77	2.79	2.92	2.90	2.91	2.95	2.92	2.91	2.91	2.91	2.87	2.92
Fe/Fe+Mg	0.40	0.40	0.40	0.39	0.42	0.40	0.40	0.40	0.43	0.43	0.52	0.53	0.52	0.52	0.53	0.54	0.53	0.54	0.55	0.54
mgli ‡	3.10	3.01	3.11	3.19	2.94	3.23	3.09	3.01	2.84	2.84	2.31	2.29	2.33	2.34	2.32	2.28	2.29	2.28	2.26	2.26
feal ‡	1.81	1.64	1.62	1.59	1.81	1.92	1.74	1.63	1.88	1.78	2.21	2.34	2.26	2.24	2.26	2.31	2.28	2.38	2.53	2.29

b.d. = below detection limit at a 95% confidence level; * = calculated stoichiometrically; † = calculated from LA-ICP-MS analysis; ‡ = after Tischendorf et al. (1997).

APPENDIX 8

Table A. Major element composition of S-type muscovites from sample NAR-1 (in wt.%) determined by EPMA. Cations calculated on the basis of 22 oxygens.

	S-type						
	NAR-1						
	grain 1	grain 2	grain 3	grain 4	grain 5	grain 6	grain 7
SiO_2	45.44	45.37	45.26	45.31	45.55	46.10	44.90
TiO_2	b.d.	b.d.	0.44	b.d.	b.d.	b.d.	b.d.
Al_2O_3	32.01	32.06	32.25	31.83	32.09	30.74	32.17
FeO	3.41	3.07	3.23	3.60	3.44	4.10	3.16
MgO	0.62	0.64	0.66	0.72	0.71	0.97	0.63
CaO	b.d.	b.d.	b.d.	b.d.	b.d.	b.d.	b.d.
Na_2O	0.41	0.37	0.43	0.35	0.34	0.30	0.40
K_2O	10.46	10.35	10.14	9.97	10.52	10.28	9.87
Li_2O †	0.16	0.15	0.17	0.16	0.16	0.16	0.14
H_2O*	4.32	4.31	4.34	4.31	4.34	4.32	4.29
Total	96.84	96.34	96.93	96.24	97.14	96.97	95.57
Si	6.30	6.31	6.26	6.31	6.30	6.40	6.28
Al^{IV}	1.70	1.69	1.74	1.69	1.70	1.60	1.72
T-site total	8.00	8.00	8.00	8.00	8.00	8.00	8.00
Al^{VI}	3.53	3.56	3.51	3.53	3.53	3.42	3.59
Ti	0.00	0.00	0.05	0.00	0.00	0.00	0.00
Fe	0.40	0.36	0.37	0.42	0.40	0.48	0.37
Mg	0.13	0.13	0.14	0.15	0.15	0.20	0.13
Li †	0.09	0.08	0.09	0.09	0.09	0.09	0.08
M-site total	4.06	4.05	4.07	4.10	4.07	4.10	4.09
Ca	0.00	0.00	0.00	0.00	0.00	0.00	0.00
Na	0.11	0.10	0.12	0.09	0.09	0.08	0.11
K	1.85	1.84	1.79	1.77	1.86	1.82	1.76
I-site total	1.96	1.94	1.91	1.87	1.95	1.90	1.87
OH	4.00	4.00	4.00	4.00	4.00	4.00	4.00

Total	18.11	18.07	18.07	18.06	18.10	18.09	18.04
Al total	5.23	5.25	5.26	5.22	5.23	5.03	5.30
Fe/Fe+Mg	0.75	0.73	0.73	0.74	0.73	0.70	0.74
mgli ‡	0.04	0.05	0.04	0.06	0.06	0.11	0.05
feal ‡	-3.14	-3.21	-3.09	-3.12	-3.13	-2.95	-3.22

b.d. = below detection limit at a 95% confidence level; * = calculated stoichiometrically; † = calculated from LA-ICP-MS analysis; ‡ = after Tischendorf et al. (1997).

APPENDIX 9

Table A. Major element composition of A-type amphiboles (in wt.%) determined by EPMA. Cations calculated on the basis of 24 oxygens.

	A-type									
	LOV-1		LOV-2.1						LOV-2.2	
	grain 9	grain 10	grain 2	grain 3	grain 6	grain 8	grain 9	grain 10	grain 2	grain 4
SiO_2	40.03	40.15	39.00	40.20	39.85	39.72	39.19	40.31	39.75	40.29
TiO_2	0.61	1.13	1.08	1.74	b.d.	1.25	1.00	1.33	1.44	1.36
Al_2O_3	8.47	8.27	8.71	8.18	8.57	8.47	8.71	8.35	8.52	8.21
FeO	33.23	30.80	31.19	31.85	30.41	30.31	30.03	30.21	30.83	31.00
MgO	1.90	2.82	1.98	2.82	3.07	2.60	2.50	2.98	1.94	2.69
CaO	10.46	9.99	9.92	10.64	10.72	10.15	9.82	10.39	9.81	10.24
Na_2O	1.73	1.76	1.85	1.73	1.75	1.78	1.76	1.77	1.76	1.68
K_2O	1.44	1.41	1.55	1.68	1.66	1.55	1.51	1.68	1.48	1.48
Initial total	97.87	96.33	95.27	98.83	96.02	95.82	94.54	97.02	95.52	96.95
$Fe^{3+}/\Sigma Fe^*$	0.15	0.12	0.10	0.12	0.14	0.06	0.07	0.06	0.06	0.11
FeO*	28.15	27.01	28.07	27.90	26.24	28.55	28.02	28.55	29.10	27.62
Fe_2O_3*	5.65	4.21	3.47	4.39	4.63	1.95	2.24	1.85	1.92	3.76
H_2O+*	1.85	1.87	1.86	1.86	1.87	1.86	1.87	1.87	1.86	1.87
Total	100.29	98.62	97.48	101.13	98.36	97.88	96.63	99.07	97.58	99.19
Si	6.46	6.53	6.46	6.42	6.51	6.53	6.52	6.54	6.56	6.53
Al	1.54	1.47	1.54	1.54	1.49	1.47	1.48	1.46	1.44	1.48
Ti	-	-	-	0.05	-	-	-	-	-	-
T-site total	8.00	8.00	8.00	8.00	8.00	8.00	8.00	8.00	8.00	8.00
Ti	0.07	0.14	0.14	0.16	-	0.15	0.13	0.16	0.18	0.17
Al	0.07	0.11	0.17	-	0.16	0.18	0.23	0.14	0.22	0.09
Fe^{3+}	0.69	0.51	0.43	0.53	0.57	0.24	0.28	0.23	0.24	0.46
Fe^{2+}	3.71	3.55	3.78	3.64	3.53	3.79	3.74	3.75	3.88	3.64
Mg	0.46	0.68	0.49	0.67	0.75	0.64	0.62	0.72	0.48	0.65
C-site total	5.00	5.00	5.00	5.00	5.00	5.00	5.00	5.00	5.00	5.00
Fe^{2+}	0.09	0.12	0.11	0.08	0.06	0.14	0.16	0.13	0.14	0.10

Mg	-	-	-	-	-	-	-	-	-	-
Ca	1.81	1.74	1.76	1.82	1.88	1.79	1.75	1.81	1.74	1.78
Na	0.10	0.14	0.13	0.10	0.07	0.08	0.09	0.07	0.13	0.12
B-site total	2.00	2.00	2.00	2.00	2.00	2.00	2.00	2.00	2.00	2.00
Ca	-	-	-	-	-	-	-	-	-	-
Na	0.44	0.42	0.47	0.44	0.49	0.49	0.48	0.49	0.43	0.41
K	0.30	0.29	0.33	0.34	0.35	0.33	0.32	0.35	0.31	0.31
A-site total	0.74	0.71	0.80	0.78	0.83	0.82	0.80	0.84	0.75	0.71
OH	2.00	2.00	2.00	2.00	2.00	2.00	2.00	2.00	2.00	2.00
Sum T+C+B+A	15.74	15.71	15.79	15.78	15.83	15.82	15.80	15.84	15.75	15.71
Subgroup	Ca	Ca	Ca	Ca	Ca	Ca	Ca	Ca	Ca	Ca

b.d. = below detection limit; * = calculated.

APPENDIX 10

Table A. Biotite analysis data measured by LA-ICP-MS, elements Li-Nb. All element abundances are in ppm. Green rows refer to ovoid-hosted biotites (see text).

(continued)	Grain	Li	Be	B	Sc	Co	Ni	Cu	Zn	Ga!	Ge	Zr	Nb
LOV-1	grain2	611.84	1.79	b.d.	6.82	17.6	2.72	3.72	630.39	28.24	4.97	3.6	201.27
LOV-1	grain3	582.33	0.94	0.32	4.09	26.36	3.13	0.21	1134.35	26.44	4.44	4.53	226.16
LOV-1	grain4	446.72	1.66	1.68	2.92	16.27	2.75	4.88	183.55	34.18	3.87	2.38	146.1
LOV-1	grain5	592.05	1.56	b.d.	4.95	20.08	3.71	0.63	177.28	26.45	3.62	3.23	156.26
LOV-1	grain7	564	0.49	0.49	10.28	28.57	3.49	0.2	996.41	15.06	3.8	3.09	92.93
LOV-1	grain8	450.54	1.14	1.74	8.85	25.17	3.52	22.82	781.9	27.17	3.85	1.43	81.64
LOV-2.1	grain1	644.04	0.85	b.d.	9.52	27.81	3.62	0.13	1015.79	18.22	4.07	1.93	170.67
LOV-2.1	grain7	590.04	0.32	b.d.	13.82	34.92	4.68	0.08	1137.95	16.67	3.86	2.13	112.81
LOV-2.2	grain1	599.3	0.61	b.d.	41.9	25.17	2.18		1220.12	22.76	4.81	3	102.52
LOV-2.2	grain3	505.34	1.28	0.49	11.31	30.11	4.56	0.21	167.35	6.52	3.75	1.21	67.06
LOV-2.2	grain6	494.78	1.69	0.66	9.68	26.09	2.7	0.16	925.24	13.01	4.28	1.87	114.64
LOV-2.2	grain7	545.32	0.92	0.64	15.88	30.29	2.76	0.05	500.23	23.56	5.23	4.46	67.01
LOV-2.2	grain8	657.28	0.9	0.7	10.84	27.28	3.66	0.12	1002.09	29.35	3.38	1.89	149.57
LOV-2.2	grain9	531.61	1.14	0.74	9.73	30.96	3.9	0.16	1088.52	26.76	3.86	2.9	139.04
LOV-2.2	grain10	658.89	0.9	1.02	8.79	30.43	3.79	0.11	1190.45	31.61	3.74	2.65	155.4
LOV-2.2	grain11	735.25	0.76	0.85	12.32	31.81	4.37	0.18	1250.53	33.23	4.29	5.78	144.42
LOV-2.2	grain12	796.88	1.05	1.05	11.93	31.87	4.2	0.38	1235.5	30.42	3.68	4.09	147.28
LOV-2.2	grain13	669.86	1.11	1.08	8.47	29.95	3.7	0.17	1187.42	27.75	3.96	2.3	139.68
LOV-2.2	grain14	732.55	0.9	1.05	7.77	29.76	3.86	0.87	1213.32	31.15	3.91	7.37	163.47
LOV-3	grain1	1327.64	3.62	0.59	58.84	10.15	0.4	1.92	1006.95	58.07	4.27	1.4	369.53
LOV-3	grain2	1291.74	3.19	0.68	62.03	10.36	0.39	0.56	957.62	60.66	4.78	1.19	407.9
LOV-3	grain3	1323.77	3.32	b.d.	59.78	9.85	0.51	0.17	860.84	56.70	4.07	0.71	401.23

(continued)	Grain	Li	Be	B	Sc	Co	Ni	Cu	Zn	Ga!	Ge	Zr	Nb
LOV-3	grain4	1159.43	3.66	b.d.	62.69	10.02	0.53	0.35	852.24	61.77	4.59	0.92	368.45
LOV-3	grain5	1216.06	3.31	0.5	59.35	9.42	0.44	0.51	937.03	60.16	4.11	1	389.65
LOV-3	grain6	1217.83	3.04	0.33	58.4	9.58	0.46	0.19	909.03	55.90	4.56	0.84	403.04
LOV-3	grain7	1062.41	3.23	0.8	58.65	9.74	0.42	0.22	790.81	57.96	5.49	0.99	404.06
LOV-3	grain8	1242.97	2.76	0.36	55.05	9.05	0.32	0.12	770.66	54.24	4.09	1.1	407.01
LOV-3	grain9	992.18	3.03	0.36	54.67	9.61	0.35	0.25	1007.57	61.47	5.28	1.13	459.2
LOV-3	grain10	1043.31	3.46	b.d.	62.18	9.61	0.36	0.35	954.51	64.22	5.09	1.07	394.72
LOV-4	grain1	952.74	7.22	2.2	72.34	18.71	2.81	1.14	936.64	48.08	3.97	2.09	260.36
LOV-4	grain2	1042.46	4.29	0.41	74	17.34	2.62	0.29	953.57	43.57	2.66	1.28	208.82
LOV-4	grain3	918.19	4.34	0.6	72.59	16.89	2.69	0.13	946.58	42.66	3.77	0.58	237.9
LOV-4	grain4	865.71	4.34	0.66	64.73	16.24	2.35	0.12	860.52	42.82	5.02	0.6	264.61
LOV-4	grain5	728.89	5.31	1.86	70.05	17.38	2.86	0.27	984.75	51.32	6.3	0.91	422.22
LOV-4	grain7	763.79	4.18	b.d.	65.53	16.34	2.77	0.2	734.84	35.77	3.7	0.44	302.23
LOV-4	grain8	863.68	4.37	0.33	67.34	16.74	2.39	0.11	818.68	36.78	2.99	0.47	183.61
LOV-4	grain9	741.06	4.89	0.37	69.05	16.09	2.33	0.11	867.52	43.34	3.75	1.29	289.73
LOV-4	grain10	797.95	5.2	0.5	71.55	17.33	2.48	0.12	900.09	43.20	3.02	0.96	189.15
LOV-5	grain1	495.19	3.25	0.52	5.28	20.82	1.22	2.05	1316.16	40.12	3.55	11.94	157.52
LOV-5	grain2	580.83	1.62	b.d.	6.3	13.31	0.63	0.79	782.32	25.88	4.15	3.06	222.68
LOV-5	grain3	584.38	1.06	0.41	8.76	15.28	0.98	0.71	1288.38	20.40	4.94	3.23	158.09
LOV-5	grain4	660.39	1.34	0.49	7.79	18.41	0.96	9.06	1656.35	17.43	3.59	4.06	108.39
LOV-5	grain5	627.18	1.05	0.93	27.27	15.69	1.13	13.03	1183.55	27.57	3.55	6.67	96.04
LOV-5	grain6	539.21	2.72	1.2	30.81	21.3	1.41	6.6	1271.16	34.08	5.16	10.54	129.8
LOV-5	grain7	620.81	0.97	0.36	5.82	14.3	0.64	10.87	1189.11	19.36	5.66	2.9	284.76
LOV-5	grain8	417.57	0.78	0.49	4.19	14.65	0.75	9.25	1341.59	30.85	5.02	0.82	82.14
LOV-5	grain9	547.03	0.76	0.31	7.2	16.98	1.23	2.69	817.24	19.66	3.83	2.43	172.94
LOV-5	grain10	561.46	0.8	0.23	4.11	14.23	0.71	0.58	1269.49	11.17	3.56	2.55	155.04
LOV-6.1	grain1	719.3	1.06	0.79	2	14.55	1.08	0.15	934.32	18.52	3.21	1.71	177.48

(continued)	Grain	Li	Be	B	Sc	Co	Ni	Cu	Zn	Ga!	Ge	Zr	Nb
LOV-6.1	grain2	671.28	1.04	0.53	5.1	18.5	0.64	0.11	1015.09	20.04	4.34	3.65	244.25
LOV-6.1	grain3	676.51	0.76	0.47	4.43	14.76	0.8	0.1	817.15	22.31	3.6	1.53	172.37
LOV-6.1	grain4	783.05	0.65	0.54	2.82	15.63	0.72	0.12	685.88	13.42	2.85	1.94	174.54
LOV-6.1	grain5	864.91	0.75	0.49	1.95	18.43	0.68	0.12	964.74	11.96	2.97	2.55	177.37
LOV-6.1	grain6	879.21	1.01	0.67	6.71	17.25	0.8	0.08	958.81	34.74	4.88	6.22	236.33
LOV-6.1	grain7	631.56	0.69	0.73	20.81	21.25	1.5	0.12	1110.06	39.48	4.18	20.25	122.56
LOV-6.1	grain8	869.58	1.18	0.56	5.19	17.28	0.62	0.12	1113.55	21.21	4.01	2.39	168.61
LOV-6.1	grain9	708.16	0.62	3.58	7.48	15.95	0.68	0.08	1058.28	18.96	2.99	1.97	118.93
LOV-6.2	grain1	738.44	1.73	1.68	2.16	22.43	1.18	0.07	1174.18	32.99	4.34	14.99	158.04
LOV-6.2	grain2	734.49	0.88	0.39	12.09	16.62	0.74	0.08	1127.45	48.32	8.62	4.7	378.38
LOV-6.2	grain3	678.61	0.79	0.36	7.13	15.81	0.71	0.1	888.02	9.10	4.45	2.24	235.09
LOV-6.2	grain4	666.11	0.81	0.42	12.52	14.78	0.72	0.1	940.32	29.49	4.21	7.03	164.17
LOV-6.2	grain5	708.72	1.01	b.d.	10.94	17.94	0.83	0.08	1212.09	44.07	7.51	3.6	367.2
LOV-6.2	grain6	769.04	0.73	0.78	21.44	16.05	0.71	0.09	1273.91	28.45	6.2	3.82	328.56
LOV-6.2	grain7	759.95	0.91	0.36	19.81	19.99	1.04	0.1	1253.28	35.49	5.93	9.27	211.43
LOV-6.2	grain8	911.02	0.68	0.42	2.39	17.02	0.69	0.1	1118.12	4.43	2.89	2.28	170.7
LOV-6.2	grain9	826.49	0.83	0.39	5.88	16.87	0.86	0.08	1125.58	0.41	2.91	2.84	177.93
LOV-6.2	grain10	852.66	0.82	0.66	2.89	16.35	0.8	0.1	551.65	5.01	3.2	1.81	131.65
LOV-6.2	grain11	917.9	0.6	b.d.	2.18	15.93	0.67	0.11	982.84	1.93	2.72	2.15	171.21
OLR09	grain1	139.24	b.d.	0.6	38.75	53.09	91.01	3.35	356.93	12.23	3.24	0.35	57.89
OLR09	grain2	145.03	b.d.	0.54	39.14	48.54	65.2	2.47	353.28	7.92	2.95	0.3	41.89
OLR09	grain3	162.8	b.d.	b.d.	41.75	44.66	66.55	0.23	399.26	21.74	2.81	0.23	52.85
OLR09	grain4	152.6	b.d.	0.49	43.51	50.16	63.57	2.74	312.48	13.77	2.74	0.27	63.51
OLR09	grain5	142.03	b.d.	b.d.	41.1	51.24	65.45	3.61	338.86	12.85	2.91	0.7	59.06
OLR09	grain6	164.5	b.d.	0.41	38.73	46.84	63.38	2.43	285.4	11.60	2.92	0.29	60.36
OLR09	grain7	142.58	0.2	0.26	36.9	57.63	86.4	0.14	342.84	14.22	3.64	0.22	55.28
OLR09	grain8	130.99	0.17	0.42	40.44	51.68	75.12	1.59	321.94	8.38	3.56	0.3	51.2

(continued)	Grain	Li	Be	B	Sc	Co	Ni	Cu	Zn	Ga!	Ge	Zr	Nb
OLR09	grain9	150.31	b.d.	0.5	41.3	50.08	72.21	5.85	322.16	11.47	2.68	0.34	58.24
OLR09	grain10	136.6	0.1	0.26	38	53.42	63.81	0.73	323.33	8.34	3.12	0.23	56.61
OLR09	grain11	167.09	0.44	0.63	34.16	52.68	62.23	20.54	340.05	6.47	3.29	0.32	54.64
NAR-1	grain8	2319.8	1.78	0.35	15.05	15.92	17.59	0.18	1227.63	41.65	3.78	0.09	361.2
NAR-1	grain9	2291.85	2.23	0.23	13.45	17.09	19.32	0.45	1260.45	38.39	4.02	0.47	331.97
NAR-1	grain10	2377.5	1.84	0.33	21.26	16.22	17.16	0.29	1243.15	41.37	4.24	0.1	232.85
VIG-1	grain1	154.87	2.45	b.d.	2.87	78.23	140.76	4.72	653.05	12.76	1.82	0.03	12.13
VIG-1	grain2	168.83	1.7	0.55	3.48	70.71	143.26	10.43	590.19	5.55	1.7	0.03	12.59
VIG-1	grain3	151.73	2.8	0.76	3.44	81.34	160.44	18.44	657.35	10.13	1.86	0.24	5.44
VIG-1	grain4	161.13	2.19	0.5	3.82	74.23	158.82	26.46	614	6.72	1.95	0.09	5.54
VIG-1	grain5	159.29	2.11	b.d.	4.68	72.71	165.89	1.54	547.11	8.29	1.2	0.03	8.39
VIG-1	grain6	153.45	2.98	0.43	3.91	75.43	162.32	3.87	518.13	14.63	1.77	0.04	8.55
VIG-1	grain7	162.39	2.37	0.42	2.7	77.37	150.58	26.52	640.31	14.86	1.62	0.08	9.42
VIG-1	grain8	160.1	1.9	0.36	2.11	73.91	146.93	17.68	603.55	7.12	1.34	0.02	9.44
VIG-1	grain9	177.87	2.24	0.51	4.32	74.38	169.49	1.05	563.84	8.43	1.46	0.21	9.81
VIG-1	grain10	172.95	2.22	0.44	3.48	77.39	175.75	10.39	573.05	9.59	1.42	0.12	9.13
KUI-3	grain1	226.12	1.03	0.6	26.38	63.3	131.79	2.22	338.28	NA	2.33	0.07	21.11
KUI-3	grain3	219.85	0.89	0.62	27.67	62.67	130.78	81.62	352.09	NA	2.27	3.49	21
KUI-3	grain2	211.27	0.76	b.d.	24.12	62.81	132.76	42	370.68	NA	2.34	1.25	19.57
KUI-3	grain4	215.53	0.72	0.49	19.45	64.63	125.74	0.73	327.38	NA	2.27	0.04	19.03
KUI-3	grain5	206.82	0.62	0.28	20.08	65.06	126.14	0.58	325.57	NA	2.36	0.11	19.6
KUI-3	grain7	214.71	0.71	0.5	14.78	64.41	124.01	1.21	364.22	NA	2.27	0.05	18.88
KUI-3	grain6	216.6	0.87	0.56	28.83	65.57	123.42	0.43	361.11	NA	2.35	0.07	19.83
KUI-3	grain8	212.27	0.82	0.32	22.43	67.32	126	3.98	371.9	NA	2.32	0.44	18.56
KUI-3	grain9	205.08	1.03	0.39	11.59	68.47	132.13	53.33	383.49	NA	2.41	4.25	18.6
KUI-3	grain10	212.13	0.88	0.46	22.13	67.39	126.66	3.58	377.46	NA	2.62	0.64	18.21

b.d. = below detection limit; ! = corrected for doubly charged Ba – concentrations informational and speculative, see Chapter 3.5.2. for discussion; NA = not analyzed (assumed to be 0).

Table B. Biotite analysis data measured by LA-ICP-MS, elements Cd-Pb. All element abundances are in ppm. Green rows refer to ovoid-hosted biotites (see text).

(continued)	Grain	Cd	^{113}In*	^{115}In*	Sn	Ba	Nd	Dy	Ho	Hf	Ta	Pb
LOV-1	grain2	b.d.	b.d.	0.56	334.83	1529.3	0.99	0.13	0.04	0.35	12.25	9
LOV-1	grain3	b.d.	b.d.	0.14	211.64	695.88	0.45	0.05	0.01	0.28	12.62	7.86
LOV-1	grain4	0.25	b.d.	0.18	166.53	621.93	1.65	0.24	0.04	0.19	12.26	13.4
LOV-1	grain5	b.d.	b.d.	0.11	100.01	818.78	0.74	0.08	b.d.	0.19	7.66	6.13
LOV-1	grain7	b.d.	b.d.	0.09	26.69	1265.69	0.21	0.02	0.01	0.24	5.36	5.78
LOV-1	grain8	b.d.	b.d.	0.19	115.05	1084.34	2.27	0.35	0.08	0.11	4.75	11.25
LOV-2.1	grain1	b.d.	b.d.	0.13	18.4	1536.83	0.06	b.d.	b.d.	0.22	7.96	5.97
LOV-2.1	grain7	b.d.	b.d.	0.09	12.46	1889.67	0.04	b.d.	b.d.	0.17	6	4.7
LOV-2.2	grain1	b.d.	b.d.	1.13	100.32	1150.38	b.d.	b.d.	b.d.	0.27	5.35	4.04
LOV-2.2	grain3	b.d.	0.4	0.27	33.98	1079.87	0.19	0.06	0.01	0.11	2.79	4.77
LOV-2.2	grain6	0.4	0.91	0.94	61.71	1342.94	b.d.	b.d.	0.06	0.19	6.37	3.56
LOV-2.2	grain7	b.d.	b.d.	0.19	22.58	874.82	0.09	0.03	0.01	0.49	3.99	7.82
LOV-2.2	grain8	b.d.	b.d.	0.14	29.4	1740.1	0.06	b.d.	b.d.	0.32	8.5	5.81
LOV-2.2	grain9	b.d.	b.d.	0.08	22.72	1544.22	0.03	0.01	0.01	0.31	8.49	5.93
LOV-2.2	grain10	b.d.	b.d.	0.08	32.97	1756	b.d.	b.d.	b.d.	0.5	9.44	6.39
LOV-2.2	grain11	b.d.	b.d.	0.09	27.79	1782.08	0.08	b.d.	b.d.	0.65	8.22	7.11
LOV-2.2	grain12	b.d.	b.d.	0.1	26.25	1545.23	0.1	0.06	0.01	0.55	8.17	6.09
LOV-2.2	grain13	b.d.	b.d.	0.08	30.1	1699.49	b.d.	b.d.	0.01	0.37	10.1	6.33
LOV-2.2	grain14	b.d.	b.d.	0.12	33.49	1622.58	b.d.	b.d.	0.06	0.96	10.86	6.33
LOV-3	grain1	b.d.	0.68	0.6	101.74	270.25	0.9	0.22	0.05	0.23	12.74	6.89
LOV-3	grain2	b.d.	b.d.	0.7	114.81	209.55	0.24	0.06	0.01	0.19	15.72	5.53
LOV-3	grain3	b.d.	0.32	0.58	93.32	340.84	b.d.	b.d.	b.d.	0.09	15.03	4.91
LOV-3	grain4	b.d.	b.d.	0.61	89.83	269.96	0.15	0.05	b.d.	0.09	9.41	6.14
LOV-3	grain5	b.d.	0.51	0.54	87.54	246.23	0.34	0.13	0.01	0.13	17.95	12.55
LOV-3	grain6	b.d.	0.44	0.59	99.23	236	0.1	0.01	0.01	0.11	22.63	5.94

(continued)	Grain	Cd	^{113}In*	^{115}In*	Sn	Ba	Nd	Dy	Ho	Hf	Ta	Pb
LOV-3	grain7	b.d.	0.5	0.68	92.82	88.19	0.2	0.04	0.01	0.09	47.01	6.71
LOV-3	grain8	b.d.	0.41	0.53	88.43	246.31	0.02	0.01	0	0.25	12.02	4.58
LOV-3	grain9	b.d.	0.5	0.61	94.15	87.94	0.49	0.1	0.02	0.12	43.93	10.28
LOV-3	grain10	b.d.	0.41	0.63	95.35	236.73	0.06	b.d.	b.d.	0.36	14.11	6.39
LOV-4	grain1	b.d.	b.d.	0.61	69.9	185.36	b.d.	b.d.	b.d.	0.29	9.04	15.85
LOV-4	grain2	b.d.	b.d.	0.47	61.6	227.28	0.32	0.05	b.d.	0.52	6.79	6.75
LOV-4	grain3	b.d.	0.41	0.52	59.34	227.36	0.08	0.04	0.01	0.2	5.79	5.43
LOV-4	grain4	0.26	0.48	0.51	66.93	172.98	0.27	0.03	0.01	0.21	16.18	4.12
LOV-4	grain5	b.d.	0.65	0.58	64	103.47	0.6	0.11	0.02	0.28	28.6	18.62
LOV-4	grain7	b.d.	b.d.	0.52	57.79	187.26	0.14	0.05	0.01	0.09	8.65	5.79
LOV-4	grain8	b.d.	0.61	0.48	52.98	191.06	0.01	0	b.d.	0.12	4.36	3.58
LOV-4	grain9	b.d.	0.51	0.52	72.88	144.29	0.04	b.d.	b.d.	0.48	15.47	3.91
LOV-4	grain10	b.d.	0.43	0.53	61.69	320.68	0.23	0.05	0.01	0.41	5.2	6.17
LOV-5	grain1	b.d.	b.d.	0.11	66.85	828.31	2.56	0.28	0.05	1.38	7.06	9.07
LOV-5	grain2	b.d.	0.3	0.24	36.17	635.84	0.92	0.11	0.02	0.69	11.7	9.64
LOV-5	grain3	0.16	b.d.	0.21	37.53	509.04	5.65	0.53	0.13	0.38	20.34	8.46
LOV-5	grain4	0.31	0.28	0.2	42.17	787.41	25.71	2.94	0.66	0.37	7.98	10.79
LOV-5	grain5	b.d.	0.27	0.2	44.5	827.9	3.92	0.71	0.13	0.91	3.99	13.19
LOV-5	grain6	b.d.	b.d.	0.22	48.6	735.97	1.6	0.76	0.16	0.96	6.63	19
LOV-5	grain7	b.d.	0.22	0.2	35.44	395.08	15.51	1.63	0.35	0.35	19.54	17.26
LOV-5	grain8	0.52	0.51	0.29	53.4	568.26	21.13	2.86	0.62	0.08	6.86	31.09
LOV-5	grain9	b.d.	b.d.	0.23	32.69	680.97	2.71	0.33	0.05	0.35	9.3	7.24
LOV-5	grain10	b.d.	0.2	0.24	44.39	777.75	0.29	0.07	0.01	0.22	17.32	8.98
LOV-6.1	grain1	b.d.	b.d.	0.11	30.79	710.22	b.d.	b.d.	b.d.	0.14	11.09	10.07
LOV-6.1	grain2	b.d.	0.1	0.08	35.95	601.14	0.23	0.04	0.02	0.31	26.42	8.51
LOV-6.1	grain3	b.d.	b.d.	0.09	43.24	655.81	0.16	b.d.	0.01	0.12	18.04	9.15
LOV-6.1	grain4	b.d.	b.d.	0.11	32.06	703.1	b.d.	b.d.	b.d.	0.12	16.25	9.37

(continued)	Grain	Cd	^{113}In*	^{115}In*	Sn	Ba	Nd	Dy	Ho	Hf	Ta	Pb
LOV-6.1	grain5	b.d.	b.d.	0.09	33.68	760.04	0.04	0.01	0	0.13	15.81	11.04
LOV-6.1	grain6	b.d.	b.d.	0.1	19.49	650.48	0.15	0.1	0.01	0.53	12.25	11.12
LOV-6.1	grain7	b.d.	b.d.	0.09	30.45	2752.12	b.d.	0.01	b.d.	2.93	5.57	5.56
LOV-6.1	grain8	b.d.	0.19	0.13	46.02	697.49	0.25	0.14	0.03	0.18	12.05	9.98
LOV-6.1	grain9	b.d.	0.29	0.2	35.27	622.6	0.19	0.09	0.02	0.15	9.54	8.51
LOV-6.2	grain1	b.d.	b.d.	0.1	41.83	548.95	b.d.	b.d.	b.d.	0.82	8.08	11.54
LOV-6.2	grain2	b.d.	b.d.	0.12	48.64	285.85	0.22	0.05	0.01	0.47	24.16	7.26
LOV-6.2	grain3	b.d.	b.d.	0.12	37.54	1810.02	b.d.	0.01	b.d.	0.18	14.5	7.22
LOV-6.2	grain4	b.d.	b.d.	0.1	35.15	590.83	b.d.	b.d.	b.d.	0.99	6.92	9.04
LOV-6.2	grain5	b.d.	b.d.	0.11	43.23	313.15	0.21	0.09	0.02	0.31	33.7	6.72
LOV-6.2	grain6	b.d.	b.d.	0.12	42.79	281.34	0.12	0.05	0.01	0.29	35.6	9.49
LOV-6.2	grain7	b.d.	0.16	0.1	39.31	314.33	0.09	0.02	0	1.34	22.42	8.04
LOV-6.2	grain8	b.d.	0.14	0.11	29.26	652.24	0.14	0.03	0.01	0.15	15.45	10.68
LOV-6.2	grain9	b.d.	0.2	0.12	35.49	987.28	0.23	0.06	0.02	0.18	11.68	10.03
LOV-6.2	grain10	b.d.	b.d.	0.11	38.5	745.6	b.d.	b.d.	b.d.	0.1	8.12	7.26
LOV-6.2	grain11	b.d.	b.d.	0.13	33.04	690.61	b.d.	0.01	0.01	0.11	13.84	11.87
OLR09	grain1	b.d.	b.d.	0.16	13.34	585.82	0.2	0.02	b.d.	0.05	3.57	2.16
OLR09	grain2	b.d.	0.53	0.14	11.73	762.72	0.56	b.d.	0.01	0.04	3.13	2.55
OLR09	grain3	b.d.	b.d.	0.22	14.17	482.24	0.03	0.01	b.d.	0.03	3.67	1.74
OLR09	grain4	b.d.	b.d.	0.17	14.06	551.63	0.25	b.d.	0.01	0.03	4.26	1.84
OLR09	grain5	b.d.	b.d.	0.17	12.75	582.66	0.4	0.03	0.01	0.06	4.04	1.85
OLR09	grain6	b.d.	b.d.	0.17	12.92	725.19	0.4	0.03	0.01	0.04	3.93	1.88
OLR09	grain7	b.d.	0.36	0.16	12.15	654.33	0.03	b.d.	b.d.	0.02	3.68	1.85
OLR09	grain8	0.15	b.d.	0.17	13.62	650.47	0.26	0.02	b.d.	0.03	3.92	2.43
OLR09	grain9	b.d.	b.d.	0.18	14.59	578.84	0.09	0.01	b.d.	0.04	4.08	1.89
OLR09	grain10	b.d.	b.d.	0.15	12.75	504.8	0.12	b.d.	b.d.	0.03	3.98	1.91
OLR09	grain11	b.d.	b.d.	0.13	11.62	739.41	2.63	0.16	0.03	0.02	3.74	3.58

(continued)	Grain	Cd	^{113}In*	^{115}In*	Sn	Ba	Nd	Dy	Ho	Hf	Ta	Pb
NAR-1	grain8	b.d.	b.d.	0.11	34.41	69.65	0.17	0.02	b.d.	0.02	96.62	3.57
NAR-1	grain9	b.d.	b.d.	0.08	32.31	72.08	0.17	b.d.	b.d.	0.06	95.05	4.81
NAR-1	grain10	b.d.	b.d.	0.11	36.73	63.21	0.14	0.01	b.d.	0.03	76.27	3.41
VIG-1	grain1	b.d.	b.d.	0.01	0.34	302.25	2.8	b.d.	b.d.	b.d.	0.27	1.61
VIG-1	grain2	0.24	b.d.	b.d.	0.34	259.98	2.1	0.01	0	b.d.	0.29	1.59
VIG-1	grain3	b.d.	b.d.	b.d.	0.32	204.74	12.23	0.08	0.01	0.02	0.11	3.56
VIG-1	grain4	b.d.	b.d.	b.d.	0.31	256.45	15.06	0.13	0.02	b.d.	0.11	3.92
VIG-1	grain5	b.d.	b.d.	b.d.	0.53	609.72	0.43	0.02	b.d.	b.d.	0.07	1
VIG-1	grain6	b.d.	b.d.	b.d.	0.45	481.78	2.15	0.03	0	b.d.	0.09	3.03
VIG-1	grain7	b.d.	b.d.	0	0.39	336.92	1.4	b.d.	b.d.	0.01	0.05	2.59
VIG-1	grain8	b.d.	b.d.	0	0.35	467.2	1.18	0.01	0	b.d.	0.06	2.67
VIG-1	grain9	b.d.	b.d.	0	0.55	1112.25	0.43	b.d.	b.d.	0.04	0.14	0.8
VIG-1	grain10	b.d.	b.d.	b.d.	0.51	451.35	0.73	b.d.	b.d.	0.02	0.11	1.11
KUI-3	grain1	b.d.	b.d.	0.05	2.09	4534.25	0.01	b.d.	b.d.	0.02	1.42	1.89
KUI-3	grain3	b.d.	b.d.	0.05	1.95	2947.87	2.16	0.41	0.07	0.1	1.48	3.48
KUI-3	grain2	b.d.	b.d.	0.04	1.91	2260.17	0.86	0.13	0.02	0.07	1.32	2.32
KUI-3	grain4	b.d.	b.d.	0.03	1.91	1227.87	0.03	0	b.d.	0.01	1.32	1.43
KUI-3	grain5	b.d.	b.d.	0.03	1.89	1625.96	b.d.	b.d.	b.d.	0.03	1.35	1.49
KUI-3	grain7	b.d.	b.d.	0.03	1.59	1433.25	0.04	b.d.	b.d.	b.d.	1.33	1.27
KUI-3	grain6	b.d.	b.d.	0.04	1.95	3402.4	0.01	b.d.	b.d.	0.02	1.64	1.99
KUI-3	grain8	0.3	b.d.	0.02	1.8	1916.78	0.17	0.03	0.01	0.02	1.19	1.36
KUI-3	grain9	b.d.	b.d.	0.01	1.7	1670.5	2.33	0.46	0.08	0.2	1.21	2.41
KUI-3	grain10	b.d.	b.d.	0.03	1.95	1926.48	0.21	0.02	0	0.04	1.31	1.62

b.d. = below detection limit; * = total indium concentration calculated from masses 113 and 115 (corrected for spectral interferences).

APPENDIX 11

Table A. Muscovite LA-ICP-MS analysis data, elements Li-Nb. Element abundances are in ppm.

Sample	Grain	Li	Be	B	Sc	Co	Ni	Cu	Zn	Ga	Ge	Zr	Nb
NAR-1	grain1	747.87	6.64	67.82	72.16	1.07	1.11	0.17	114.05	165.64	1.45	3.70	75.57
NAR-1	grain2	681.54	5.72	56.15	91.64	1.01	0.90	0.08	94.70	151.01	0.93	1.29	69.83
NAR-1	grain3	781.86	6.86	80.49	53.34	1.21	1.54	0.17	116.06	161.51	2.12	0.92	107.12
NAR-1	grain4	734.38	6.34	64.31	64.11	1.06	1.08	0.14	102.23	160.69	b.d.	0.81	79.54
NAR-1	grain5	722.51	6.40	66.51	92.50	1.12	1.23	0.25	105.51	164.58	1.14	1.20	88.19
NAR-1	grain6	733.18	7.07	68.75	50.41	1.10	1.29	b.d.	107.09	158.19	1.73	0.66	112.94
NAR-1	grain7	672.31	5.94	57.50	112.40	0.96	1.00	0.10	100.33	151.87	1.04	1.26	82.04

b.d. = below detection limit.

Table B. Muscovite LA-ICP-MS analysis data, elements Cd-Pb. Element abundances are in ppm.

Sample	Grain	Cd	^{113}In*	^{115}In*	Sn	Ba	Nd	Dy	Ho	Hf	Ta	Pb
NAR-1	grain1	b.d.	b.d.	0.57	38.80	74.18	0.07	0.12	0.02	0.20	3.82	6.54
NAR-1	grain2	b.d.	b.d.	0.64	29.29	67.00	b.d.	0.01	b.d.	0.14	2.61	4.55
NAR-1	grain3	b.d.	b.d.	0.38	55.96	73.07	b.d.	b.d.	b.d.	0.12	12.02	4.83
NAR-1	grain4	b.d.	b.d.	0.45	45.60	59.21	b.d.	b.d.	b.d.	0.17	3.84	6.70
NAR-1	grain5	b.d.	0.83	0.65	37.80	61.76	b.d.	b.d.	0.01	0.19	4.03	5.47
NAR-1	grain6	b.d.	b.d.	0.43	55.67	111.00	b.d.	b.d.	b.d.	0.08	17.08	5.69
NAR-1	grain7	b.d.	0.64	0.77	30.74	66.09	b.d.	b.d.	b.d.	0.16	3.15	4.75

b.d. = below detection limit; * = total indium concentration calculated from masses 113 and 115 (corrected for spectral interferences).

APPENDIX 12

Table A. Amphibole LA-ICP-MS analysis data, elements Li-Nb. Element abundances are in ppm. Green rows refer to ovoid-hosted amphiboles (see text).

Sample	Grain	Li	Be	B	Sc	Co	Ni	Cu	Zn	Ga	Ge	Zr	Nb
LOV-1	grain 9	8.5	15.22	1.87	101.23	9.89	0.55	0.4	935.99	38.88	7.72	187.42	53.17
LOV-1	grain 10	7.19	16.87	1.38	121.7	20.7	1.85	2.1	1036.12	37.89	7.39	151.89	82.52
LOV-2.1	grain 2	14.39	24.45	2.88	92.86	20.99	1.99	0.6	867.89	45.83	10.36	158.28	132.52
LOV-2.1	grain 3	5.04	14.35	0.62	137.58	23.94	2.46	0.42	814.09	33.81	8.88	161.82	95.7
LOV-2.1	grain 6	10.35	17.67	4.58	152.25	27.24	2.89	0.43	1006.89	40.14	8.63	151.61	63.81
LOV-2.1	grain 8	10.41	12.85	0.56	89.18	22.96	2.46	0.4	861.2	41.34	8.09	163.21	109.96
LOV-2.1	grain 9	13.07	16.63	0.37	60.31	21.81	2.21	0.48	820.54	41.27	10.14	236.65	137.08
LOV-2.1	grain 10	8.68	12.6	1.49	104.49	23.87	2.44	0.7	986.57	39.56	8.35	175.91	101.89
LOV-2.2	grain 2	30.1	21.71	0.73	95.2	21.3	1.77	0.73	979.67	41.47	9.76	151.67	103.99
LOV-2.2	grain 4	9.3	14.31	0.78	94.32	22.97	2.54	0.4	924	41.09	8.46	134.79	86.59

Table B. Amphibole LA-ICP-MS analysis data, elements Cd-Pb. Element abundances are in ppm. Green rows refer to ovoid-hosted amphiboles (see text.)

(continued)	Grain	Cd	^{113}In*	^{115}In*	Sn	Ba	Nd	Dy	Ho	Hf	Ta	Pb
LOV-1	grain 9	0.71	3.59	3.69	855.14	81.18	291.04	70.97	14.34	12.28	3.61	7.72
LOV-1	grain 10	1.42	1.14	1.27	58.58	86.18	429.67	83.3	16.27	8.87	3.47	12.86
LOV-2.1	grain 2	1.51	1.68	1.56	91.66	67.75	554.25	122.26	23.98	10.81	5.2	11.4
LOV-2.1	grain 3	0.96	1.29	1.16	5.17	68.26	517.57	96.01	18.35	9.2	3.73	8.72
LOV-2.1	grain 6	1.38	1.84	1.18	20.92	82.18	347.19	68.43	13.72	8	2.83	7.24
LOV-2.1	grain 8	1.07	1.32	1.11	7.89	115.37	496.26	90.3	17.57	10.84	5.31	8.39
LOV-2.1	grain 9	1.26	1.51	1.06	17.81	92.78	641.09	122.33	24.01	16.43	6.07	7.51

(continued)	Grain	Cd	^{113}In*	^{115}In*	Sn	Ba	Nd	Dy	Ho	Hf	Ta	Pb
LOV-2.1	grain 10	1.15	1.16	1.15	10.76	111.07	476.15	87.32	17.16	11.19	5.46	9.12
LOV-2.2	grain 2	1.39	3.79	3.53	22.15	104.81	550.09	95.62	18.25	9.74	3.83	11.58
LOV-2.2	grain 4	1.38	0.89	1.25	9.86	89.29	441.23	82.45	16.25	7.98	3.07	8.35

* = total indium concentration calculated from masses 113 and 115 (corrected for spectral interferences).

APPENDIX 13

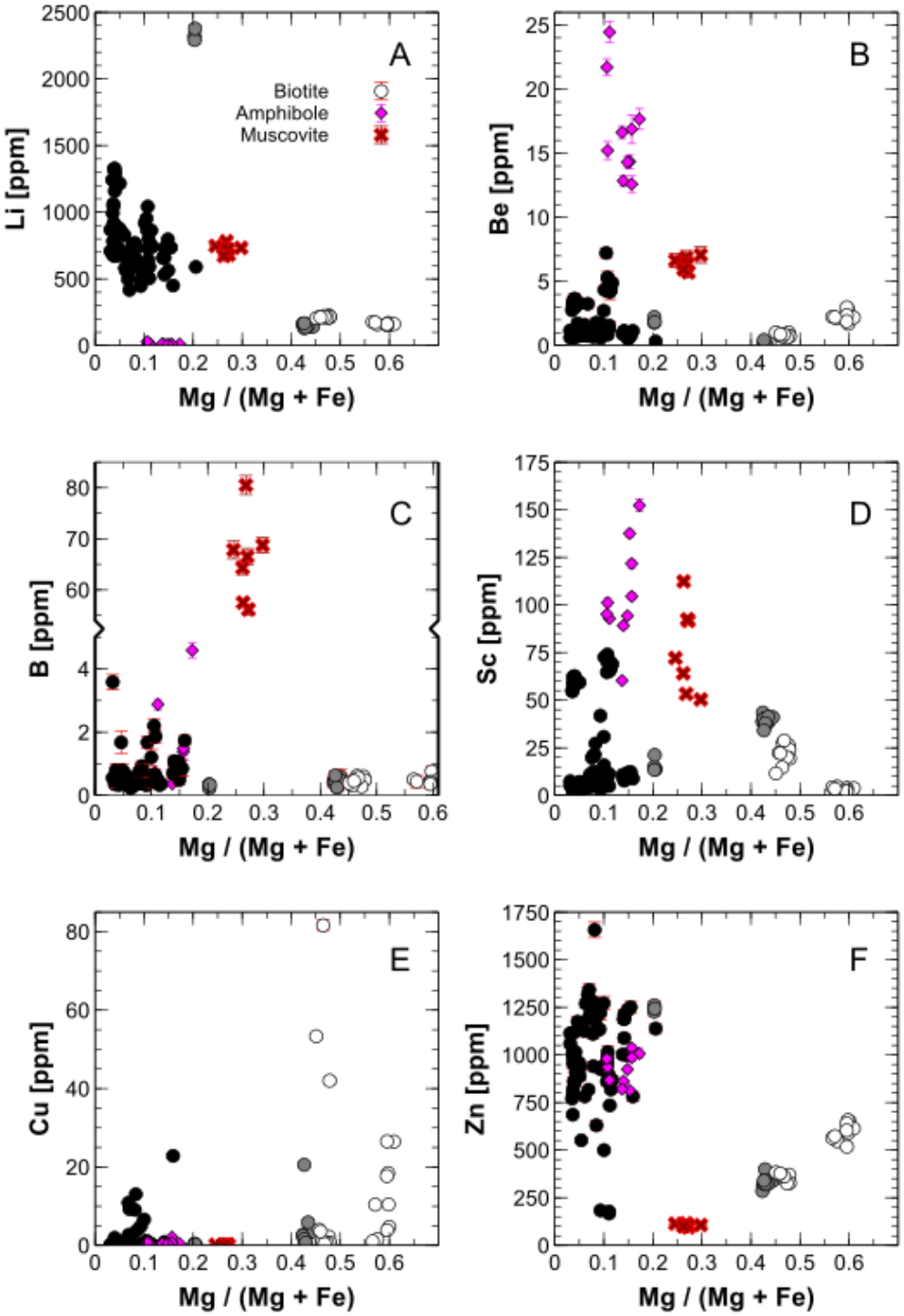

Figure 1. Variation diagrams for (A) Li, (B) Be, (C) B, (D) Sc, (E) Cu, and (F) Zn concentrations in biotites, muscovites, and amphiboles as a function of Mg/(Mg+Fe) apfu. Biotite symbology as in Fig. 22. Error bars indicate a combined 1 σ of LA-ICP-MS transient signal noise and counting statistical errors.

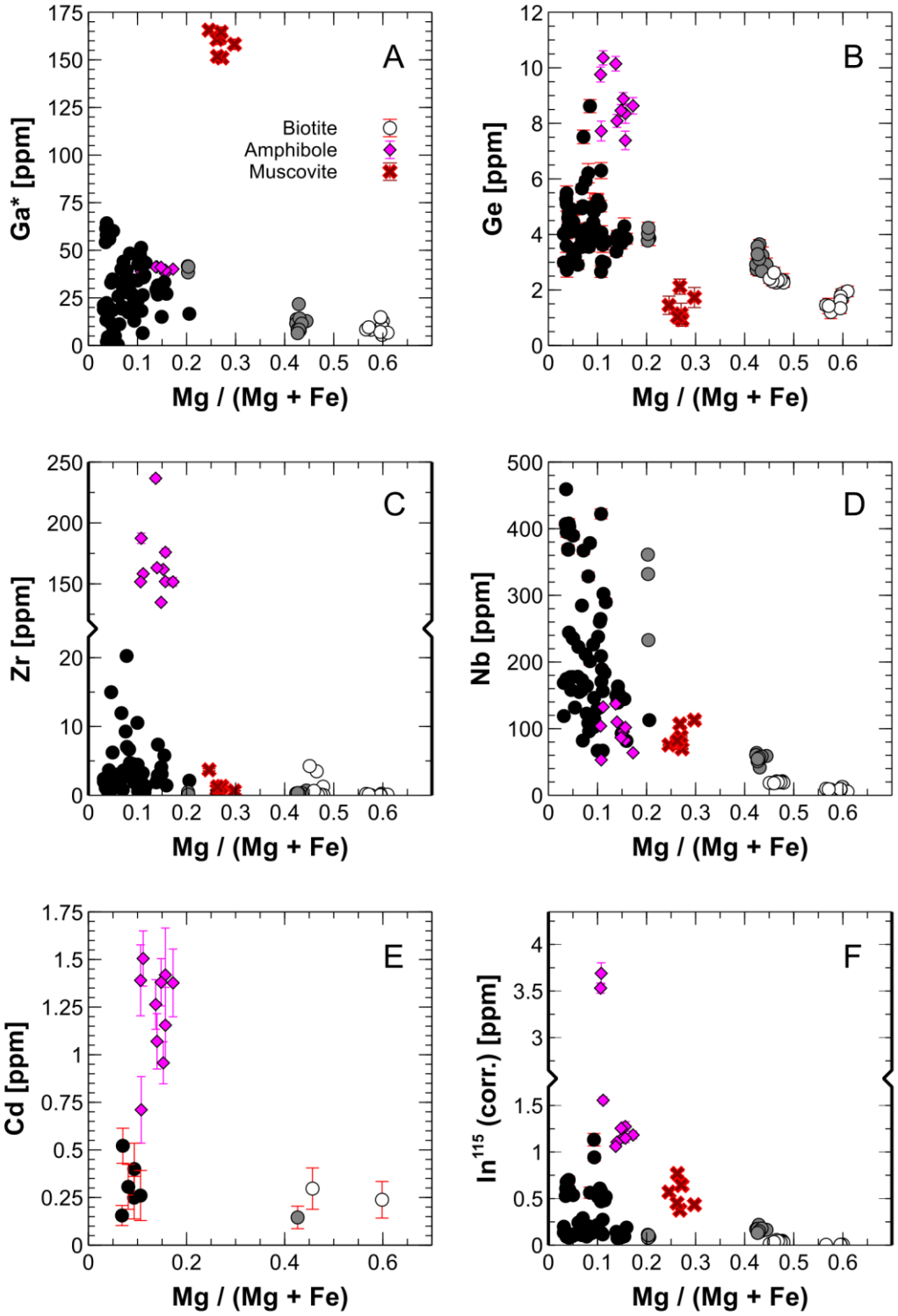

Figure 2. Variation diagrams for (A) Ga, (B) Ge, (C) Zr, (D) Nb, (E) Cd, and (F) ^{115}In (corrected) concentrations in biotites, muscovites, and amphiboles as a function of Mg/(Mg+Fe) apfu. Note that "115In (corr.) [ppm]" refers to the total indium concentration calculated from mass 115 that has been corrected for spectral interferences. Furthermore, note that Ga concentrations (*) have been corrected for doubly charged Ba, and thus these concentration values are speculative. See Chapter 3.5.2. for discussion. Biotite symbology as in Fig. 1. Error bars indicate a combined 1 σ of LA-ICP-MS transient signal noise and counting statistical errors.

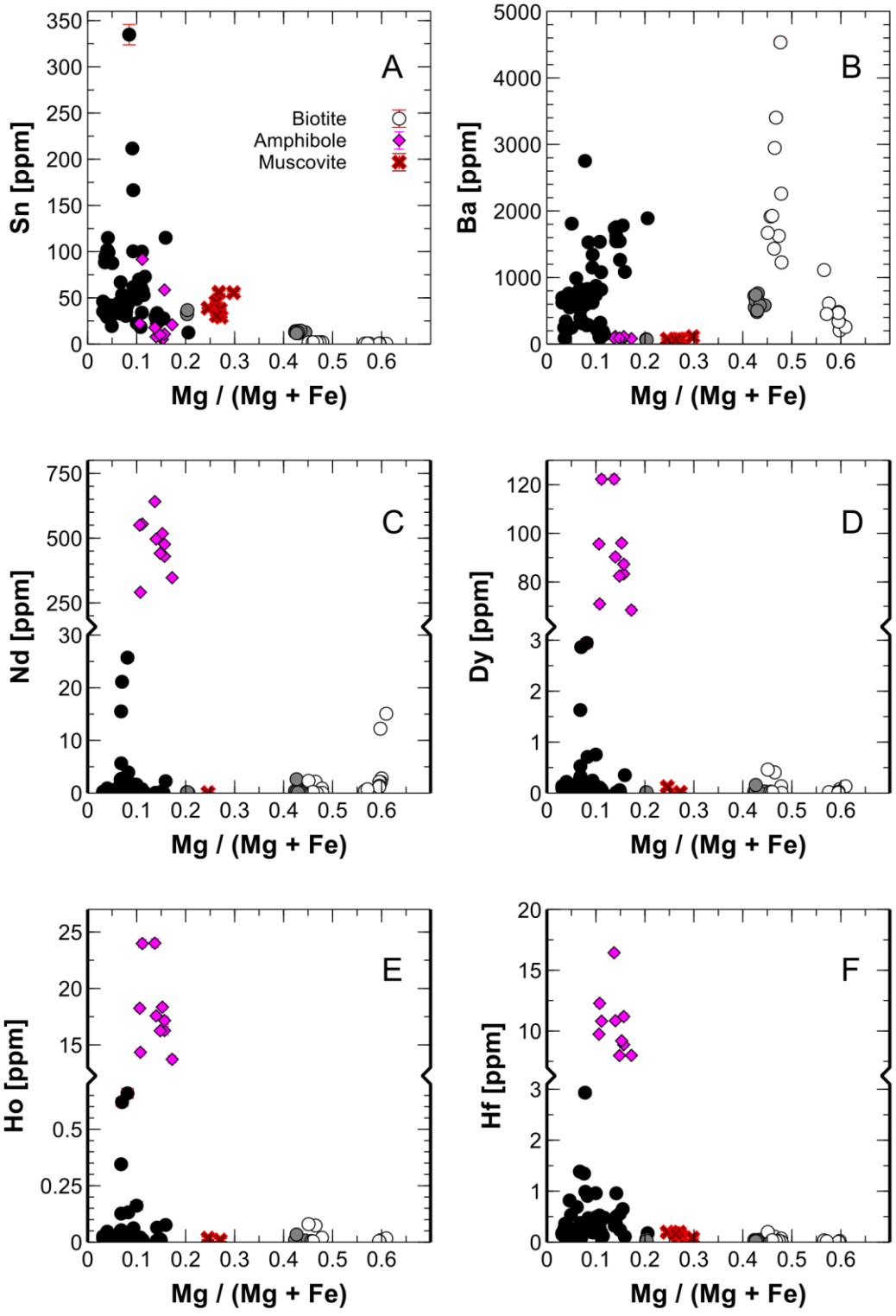

Figure 3. Variation diagrams for (A) Sn, (B) Ba, (C) Nd, (D) Dy, (E) Ho, and (F) Hf concentrations in biotites, muscovites, and amphiboles as a function of Mg/(Mg+Fe) apfu. Biotite symbology as in Fig. 1. Error bars indicate a combined 1 σ of LA-ICP-MS transient signal noise and counting statistical errors.

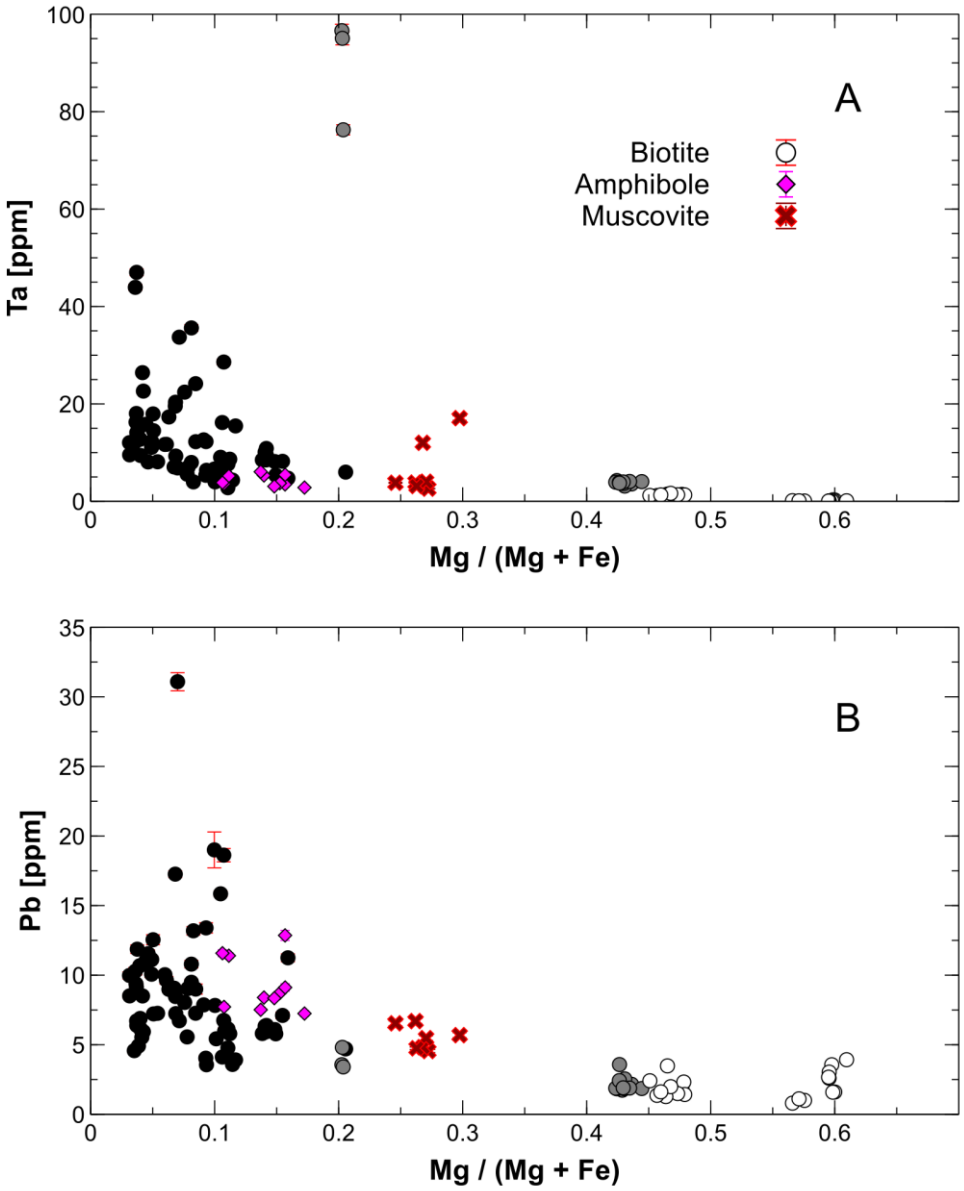

Figure 4. Variation diagrams for (A) Hf and (B) Pb concentrations in biotites, muscovites, and amphiboles as a function of Mg/(Mg+Fe) apfu. Biotite symbology as in Fig. 1. Error bars indicate a combined 1 σ of LA-ICP-MS transient signal noise and counting statistical errors.